BEHAVIOR OF NANO-CONFINED MULTI-COMPONENT FLUIDS IN SOURCE ROCKS

A Dissertation

by

SEUNGHWAN BAEK

Submitted to the Office of Graduate and Professional Studies of
Texas A&M University
in partial fulfillment of the requirements for the degree of

DOCTOR OF PHILOSOPHY

Chair of Committee,	I. Yucel Akkutlu
Committee Members,	Thomas A. Blasingame
	George J. Moridis
	Yuefeng Sun
Head of Department,	Jeffrey B. Spath

August 2019

Major Subject: Petroleum Engineering

ABSTRACT

Source rocks, such as organic-rich shale, consist of multi-scale pore structures which include pores with sizes down to nano-scale contributing to the storage of hydrocarbons. During my Ph.D. studies, using molecular simulations, I showed the applications of the concept of composition redistribution of the produced fluids in source rocks. The hydrocarbons in the source rock partition into nano-confined fluids with significantly varying physical properties across the nanopore size distribution of the organic matter. This partitioning is a consequence of multi-component hydrocarbon mixtures stored in nanopores showing a significant compositional variation with the changing pore size and pressure. It is firstly observed that this variance leads to capillary-condensation of fluids in nanopores at the lower end of the organic pore size distribution. Condensation impairs the transport ability of the fluids left behind in nanopores and consequently, their recoveries are reduced significantly.

In the light of these microscopic scale observations, I developed a new volumetric method for predicting hydrocarbons in-place honoring the compositional variability across the measured pore size distribution in the presence of nano-confinement effects. My approach allows the reservoir engineer to differentiate mobile bulk hydrocarbon fluids from the fluids under confinement and from the capillary-condensed trapped fluids.

The low recoveries from the organic nanopores makes the source rocks potential resources for enhanced oil recovery. In addition, as part of my thesis work, I considered lean gases (such as CO_2 and N_2) injection for enhanced nano-confined oil recovery. The

concept of gas injection is firstly developed in equilibrium molecular simulation research. I showed that lean gas injection could influence the vaporization pressure of the confined hydrocarbon fluid mixture and strip additional hydrocarbon molecules from the organic pores. This mechanism is known as the vaporizing gas drive in the literature.

On the other hand, the several limitations of CO_2 injection are found during my study, and ethane injection is alternatively considered for enhanced nano-confined oil recovery. I studied the ethane injection extensively and compared with CO_2 injection. Ethane has a better stripping ability against heavy hydrocarbons, and also enhances the mobility.

At reservoir scale, I propose a new robust method of simulation-based history-matching and optimization for future reserve prediction. This approach considers the total fracture surface area for the drainage of hydrocarbons as a key quantity in production from horizontal shale gas wells with multiple-hydraulic fractures. The effective fracture surface area is estimated by incorporating an analytical solution of production rate transient data associated with the formation linear flow and introduced as an additional constraint to the optimization. Stress-dependent models are employed for the fracture width and the matrix permeability change during the production. The new approach not only predicts the reserve but also the time for the fractures to close significantly when the fractures no longer produces economically. This time indicates the life of the well.

DEDICATION

To God Father, my grandmother, parents, and beloved wife, Kyuhyun Lee for supporting me with love, encouragement, and patience throughout my academic journey.

ACKNOWLEDGEMENTS

I would like to thank my committee chair Dr. Akkutlu for his academic guidance, financial support, opportunities, and most of all, faith in me. Dr. Blasingame, Dr. Moridis, and Dr. Sun also served on my graduate committee, and I appreciate their valuable contributions to this research work.

CONTRIBUTORS AND FUNDING SOURCES

Contributors

This work was supervised by a dissertation committee consisting of Professor I. Yucel Akkutlu (chair), T. A. Blasingame, and G. Moridis in the Department of Petroleum Engineering and Professor Yuefeng Sun in the Department of Geology and Geophysics.

In Chapter 2-4, the protocol originally developed by Dr. I. Yucel Akkutlu and Dr. B. Khoa was used for the composition re-distribution based on Monte Carlo Molecular Simulation.

In Chapter 5, the in-house simulator originally developed by Dr. I. Yucel Akkutlu and Dr. O. Olorode was used for history-matching and optimization.

All other work conducted for the dissertation was independently completed by the student.

Funding Sources

S. Baek's Ph.D. works have been supported by the Crisman Institute for Petroleum Research at Texas A&M University (Jan 2016 – Dec 2018), and by Marathon Oil Company (Jan 2019 – Aug 2019).

NOMENCLATURE

N_A	Avogadro’s number, 6.023x10^{23} molecule number/mol
ρ_b	Bulk mass density of the rock
$\rho_{bulk,mix}$	Bulk mass density of the fluid
$\rho_{bulk,mol}$	Bulk molar density of the fluid
$\rho_{bulk,mol,CH4}$	Bulk molar density of CH_4
K_B	Boltzmann constant
α	Biot coefficient
COM	Center-of-Mass
cEDFM	Compartmental Embedded Discrete Fracture model
p_c	Confining stress
Cr	Crossover probability rate
$d_{p,L}$	Cut-off pore size for nanopore effects
$d_{p,T}$	Cut-off pore size for trapped hydrocarbons
z_{sc}	Compressibility at standard conditions
$\rho_{adsorbed}$	Density of adsorbed phase
ρ_{free}	Density of free phase
DE	Differential Evolution
EOR	Enhanced Oil Recovery
EnKF	Ensemble Kalman filter
EOS	Equation of State

p_{eff}	Effective stress
$\mathrm{A}_{\mathrm{FRAC,RTA}}$	Effective fracture surface area based on RTA
$\mathrm{A}_{\mathrm{Frac,OPT}}$	Effective fracture surface area based on optimization
σ'_{xx}	Effective compressive stress
ϕ_{HC}	Effective porosity having mobile hydrocarbons
ρ_{total}	Fluid density in the pore
p_{wf}	Flowing bottomhole pressure
B_g	Formation volume factor
w_f	Fracture width
k_f	Fracture permeability
ϕ_f	Fracture porosity
μVT	Grand Canonical ensemble
GCMC	Grand Canonical Monte Carlo
q_g	Gas flow rate
GCMC	Grand Canonical Monte Carlo
$G(p)$	Gas in place without nanopore confinement effects
$G^*(p)$	Gas in place with nanopore confinement effects
μVT	Grand canonical
R	Gas constant
I_{HF}	Hydraulic fracturing quality index
x_f	Half fracture length
w_0	Initial matrix permeability

p_i	Initial reservoir pressure
NPT	Isothermal-isobaric ensemble
zi	Initial mole fraction
NPT	Isothermal-isobaric
$\delta_{\alpha\beta}$	Kronecker delta function
eps	Large pore cut-off
NG	Maximum number of generation
MD	Molecular Dynamics
MC	Monte Carlo
$\rho_{dp,mix}$	Mass density of the fluid in nanopore
$\rho_{dp,CH4}$	Mass density of CH_4 in nanopore
$\rho_{dp,mol}$	Molar density of the fluid in nanopore
$\rho_{dp,mol,CH4}$	Molar density of CH_4 in nanopore
B_g^*	Modified formation volume factor
C	Molar density
k_0	Matrix permeability
p_{max}	Matrix closure stress
n	Number density of hydrocarbons in large pores
n_{frac}	Number of the fractures
OGIP	Original Gas in-Place
ϕ_{FW}	Porosity of the free water

ϕ_{CBW}	Porosity of the clay bound water
ϕ_{Large}	Porosity of organic pores larger than $d_{p,L}$
ϕ_{Nano}	Porosity of organic pores smaller than $d_{p,L}$
$\phi_{trappedHC}$	Porosity of organic pores smaller than $d_{p,T}$
d_p	Pore size
$r_i(t)$	Position of Center-of-Mass in Molecular Dynamics simulation
v	Poisson's ratio
NP	Population size
t_{ap}	Pseudo time
η	Recovery enhancement
P_{sc}	Pressure at standard conditions
RTA	Rate Transient Analysis
h	Reservoir thickness
F	Scaling factor
$P_{\alpha\beta}$	Symmetrized traceless portion of the stress tensor, $\sigma_{\alpha\beta}$
τ	Tortuosity
L_h	Total lateral length of a well
T	Temperature
A_{FRAC}	Total fracture surface area
TraPPE	Transferable Potentials for Phase Equilibria Force Field
V_p	Total pore volume in one ton of rock
ϕ	Total porosity

T_{sc}	Temperature at standard conditions
$S_{trappedHC}$	Trapped hydrocarbons saturation
ε	Volume fraction of large pores
$V_{p,Nano}$	Volume of hydrocarbons in nanopores with size smaller than $d_{p,L}$
V_T	Volume fraction of trapped hydrocarbons
η	Viscoelastic shear coefficient
S_w	Water saturation
r_w	Well radius
E_f	Young's modulus

TABLE OF CONTENTS

Page

LIST OF FIGURES

LIST OF TABLES

Page

1. INTRODUCTION

1.1. Statement of the Problem

Resource shale and other source rock formations with significant amount of organic matter, such as mudstone, silt-stone and carbonate, have multi-scale pore structure including fractures, micro-cracks and pores down to a few nanometers (Loucks et al. 2012; Ambrose et al. 2012). The total amount of hydrocarbons stored are directly proportional to the amount of organic matter, and thus extensive studies on hydrocarbon storage in the organics in source rock have been conducted to investigate the effects of the amount, type and thermal maturity of the organic matter, moisture content and swelling strain (Weniger et al. 2010; Modica and Lapierre 2012; Gasparik et al. 2012; Zhang et al. 2012; Chen and Jiang 2016).

In order to estimate initial hydrocarbon in-place of the organic-rich resources, laboratory measurements have been widely adopted. However, the intrinsic ultralow permeability of the unconventional resource and the extreme subsurface conditions make this task challenging. Alternatively, molecular simulations can be used, in particular to answer some of the questions at the nanoscale. Many works have been conducted using molecular simulations up to date, and they further help us to understand behavior of hydrocarbon fluids confined in nanopores such as kerogen on microscopic level (Jiang et al. 2005; Ambrose et al. 2012; Liu and Wilcox 2012; Falk et al. 2015; Pitakbunkate et al. 2016; Bousige et al. 2016, Greathouse et al. 2016).

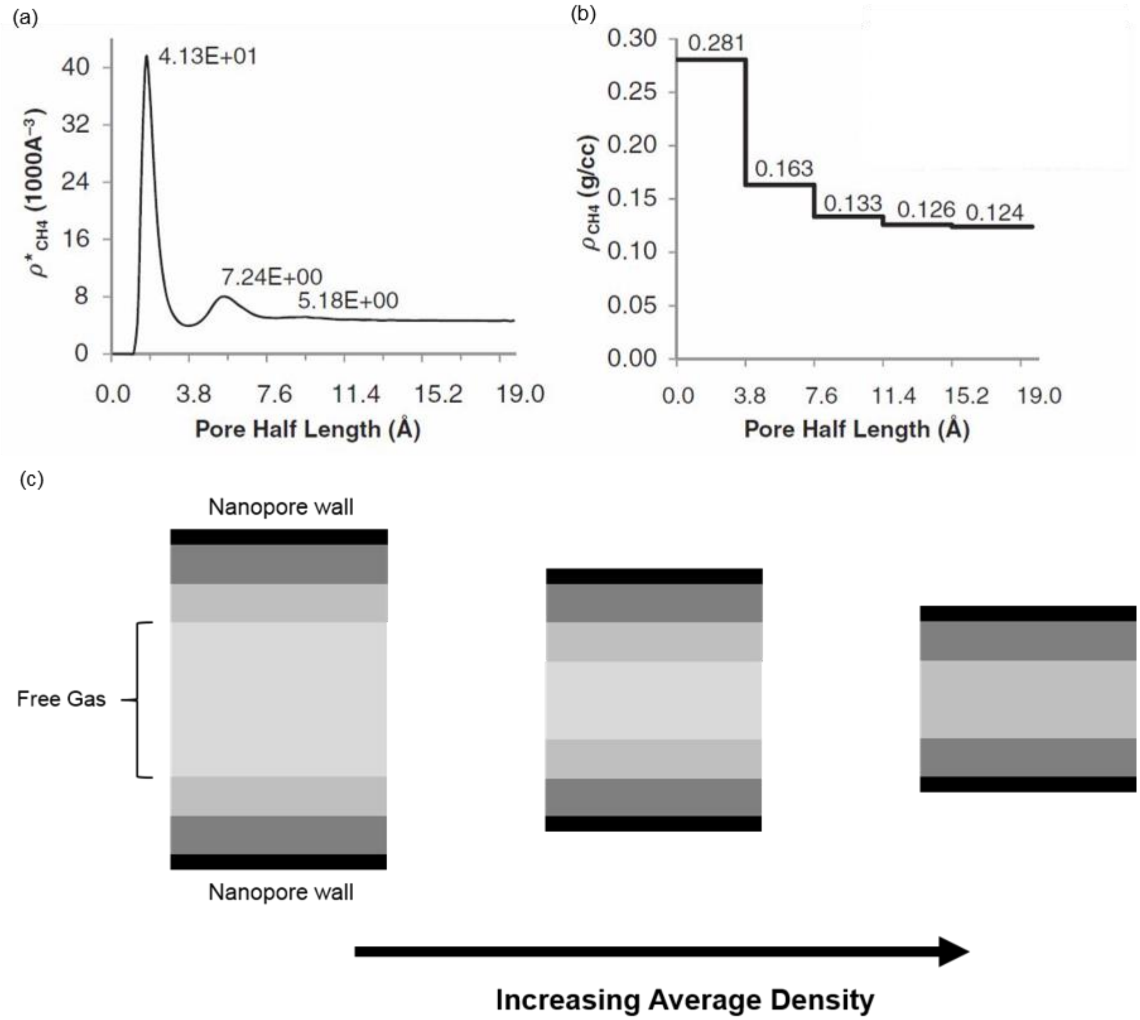

Figure 1.1 Nano-confinement effects on single component fluids.

The fluid in nanoscale pore structures is subjected to amplified molecular interactions with the walls. Thus, the fluid develops anisotropic forces near the walls and holds a non-uniform density (Bui and Akkutlu 2015). Figure 1.1 shows the density of confined pure component fluid (methane) in a nano-channel under the reservoir conditions (Ambrose at el. 2011). A graded change is observed in density in the direction

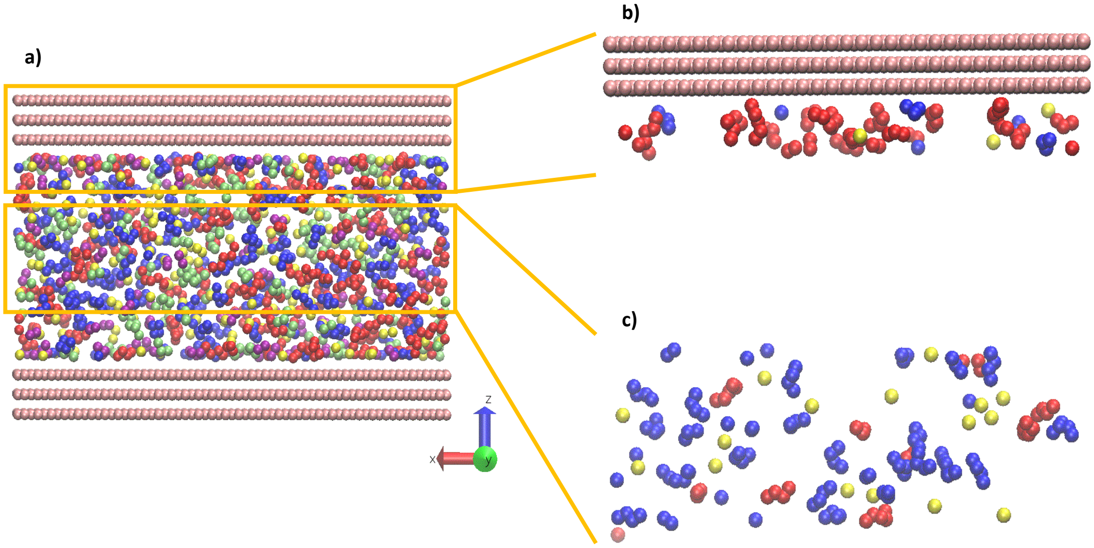

Figure 1.2 Compositional variation in a nanopore.

perpendicular to the channel surface. Consequently, a staircase-like density structure prevails near the channel walls (Ambrose et al. 2012). The high-density by the wall belongs to adsorbed fluid molecules while the low density at the central portion of the channel belongs to free fluid molecules. The free molecules are far enough from the walls so that their interactions with the wall atoms are negligible. As the channel size is reduced, the density structure near the wall does not change, but the channel volume taken up by the free fluid molecules decreases. The reduction in nano-channel size can cause a significant increase in the average density of the fluid inside the channel. Similarly, the average compressional stress applied on the fluid molecules considerably increases. We call the amplified fluid-wall molecular interactions due to increase in confinement, which leads to changes in the fluid properties, the nano-confinement effects.

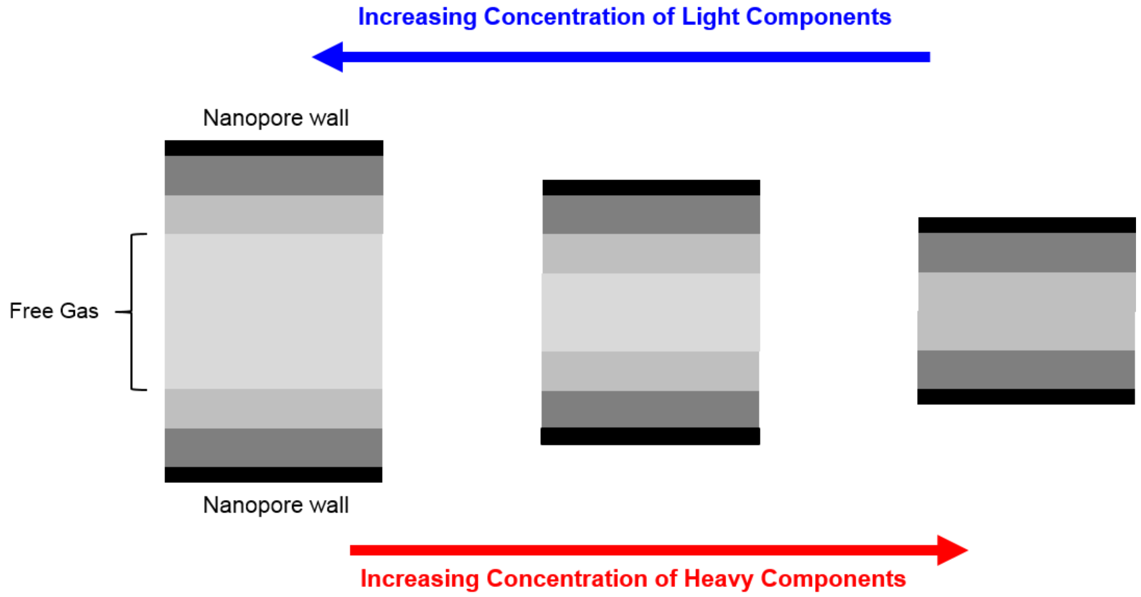

Figure 1.3 Nano-confinement effects on multi-component fluids.

Multi-component gases in nano-channels have added complexity mainly due to the presence of varying levels of fluid-wall interactions with each chemical species that make up the fluid mixture. The gas molecules experience selective adsorption and this also depends on the chemistry of the channel wall surfaces. Nano-channels have large wall surface area to volume ratio, which, in turn, could make the volume-averaged composition heavier in a nano-channel as dictated by the walls (Bui and Akkutlu 2017). Figure 1.2 shows a mixture of hydrocarbon gas in a nano-channel under equilibrium; yellow: Methane, blue: n-butane, red: n-pentane. Note that the adsorption layer composition by the wall is rich in the largest molecule of the mixture, Figure 1.2b; whereas the free fluid composition is rich in the lighter components, Figure 1.2c. Now, a graded change is observed in composition in the direction perpendicular to the channel walls due to the amplified molecular interactions with the wall atoms. Figure 1.3 shows the effect of fluid composition on the fluid storage under confinement. Again, a staircase-like structure is expected by channel walls but now the density by the walls is larger than the pure methane density because the fluid is a hydrocarbon mixture. Similarly, the reduction in the channel size will increase the average density further because of the diminishing volume with the free molecules including the light components in the mixture. Clearly, the in-situ fluid composition is likely to further escalate the confinement effects and, therefore, it should be taken into account during the investigation of fluid transport under the influence of nano-confinement. Storage of multi-component hydrocarbon fluids under nanoscale confinement is analyzed in this work highlighting the differences between single-component (pure methane) and multi-component fluid systems.

In summary, nanopore confinement has two effects on fluid density. The first effect is due to physical adsorption. It is difficult to differentiate the adsorption effect and the pore size effect in the laboratory and using simulations therefore we will refer to them here briefly as the nano-confinement effects. Consequently, the nano-confinement effects make it difficult to predict fluid behavior.

Simpler analytical models have been developed to predict the fluid behavior (Schoen and Diestler 1998; Zarragoicoechea and Kuz 2004). Travalloni et al. (2010) developed a new equation of state (EOS) on the basis of Peng-Robinson EOS with the generalized van der Waals theory. A square-well model was adopted to take into account the wall interaction, and the related parameters need to be fitted with experimental data. Their model provides good correlations of experimental data for pure fluid with the simple formulation. Also, it was expanded to multi-component fluids. The model, however, basically adopts monoatomic spherical molecules, and constant effective diameter of the molecule. In addition, interference by different components was not considered in molecular distribution in nanopores for multi-component system. Under typical reservoir conditions, those limitations would be pronounced especially for asymmetric mixtures. Especially, molecular geometry is a very critical entropic factor in confined fluids, then the simple molecular structures would cause large uncertainties. So far, most of investigations have limited their scope to simple fluids, and sometimes they have been performed under non-representative reservoir conditions.

Petroleum in reservoir includes various components. Modeling the fluids with a single component may lead to inaccurate reserve and fluid property estimation. Several experiments have reported that multi-component fluids on solid surfaces have variation in composition (Myers et al. 1968; Stevenson et al. 1991; Arri et al. 1992; Clarkson et al. 2000). Lately, thermodynamic computations of multi-component hydrocarbon fluids have confirmed that the composition in organic nanoporous materials is entirely different from the bulk fluid composition due to the nanoscale confinement effects (Bui and Akkutlu 2017). Specifically, the adsorbed fluid by the pore walls consists of heavy fraction of the hydrocarbon mixture; whereas the free phase is rich in lighter components. This is attributed to the relative affinity of individual component to pore surface, and not observed with a pure component system. This creates large compositional variation near the walls, in particular for the heaviest and lightest components. With decreasing pore dimension, the adsorbed heavy components influence progressively further on the fluid composition in the pore. Thus, the average composition in the smaller pores becomes heavier. Figure 1.2 shows the adsorption and pore size effects on the overall composition of the fluid inside the pore. As a consequence of the nano-confinement effects, at initial reservoir conditions, the hydrocarbon mixture is expected to be heavier and more viscous in the smaller pores. During production and pressure depletion, due to selective release (desorption) of the lighter hydrocarbons, the composition left inside the nanopores becomes even heavier (Bui and Akkutlu 2017). Hence, the nano-confinement could have added complexities during the production and depletion. At the fundamental level, these are significant observations with a potential impact on hydrocarbon in-place and reserve calculations in the source rocks rich in organic matter.

Recently, technical advances in horizontal drilling and hydraulic-fracturing have been the major factors in achieving economical production from unconventional resources. At reservoir scale, we can use the existing optimization technologies that have already been developed for the conventional wells during the last decades. These methods overwhelmingly use a reservoir flow simulation model to history-match the production of a well or a group of wells in the field and to forecast the reserve. However, history-matching and production forecasting of the unconventional wells, such as the horizontal shale gas wells with multiple fractures, has fundamentally different focus in comparison to classical problems of interest. Primary optimization parameters that show significant sensitivities are, in this case, the fracture geometry (i.e., its length, width, and height), the fracture conductivity, the fracture spacing (or number of fractures) and the fracture complexity. Although a horizontal well’s lateral length and the number of hydraulic fracturing stages are known accurately, the nature of fractures contributing to the production is poorly understood. This lack of knowledge brings in added complexity and uncertainties to the optimization process when the reservoir engineer is not only required to consider the key matrix parameters (such as porosity and permeability) and the geological impact on these parameters, but also the completion qualities such as the hydraulic fracturing design. This is a challenging task because various aspects related to the reservoir and the completion should be considered simultaneously.

During the formation linear flow, the area of the fractures contributing to the production becomes the key quantity. The fracture surface area can be estimated if the number and geometry of the fractures are known. However, uncertainties exist on these completion-related quantities. The industry uses micro-seismic data, production logs, wellbore image logs and tracer test to characterize the fractures (Hetz et al. 2017). These methods have limited application, however, because the data is costly, or the formation holds a relatively complex network of fractures where identifying individual wing-like planar fractures could be difficult.

A common approach is to measure the fracture surface area directly using the well production data along with an RTA method. The most widely used approach is the method also known as $A\sqrt{k}$ method, originally proposed by Wattenbarger et al. (1998). The method is used to estimate the fracture surface area from the production decline on the basis of the several strict conditions such as constant permeability or fracture width. These often limits the accuracy of the reservoir characterization and reserve prediction for unconventional gas reservoirs.

1.2. Research Objectives

The overall objectives of my research are as follows:

1. To propose a new volumetric method to estimate hydrocarbon in-place for multi-component fluids in organic-rich source rocks.
2. To analyze the behavior of the nano-confined hydrocarbons in the pores of organic materials such as kerogen and solid bitumen.
3. To measure primary recovery in organic-rich source rocks at the microscopic scale and analyze the effects of fluid composition on the primary recovery due to pressure depletion.
4. To study the impact of CO_2 injection on the recovery, in particular recovery of nano-confined oil in the organic material.
5. To investigate the impact of ethane injection the nano-confined oil recovery and compare to that due to CO_2 injection.
6. To propose a new simulation-based reservoir optimization strategy for horizontal shale gas production wells with multiple hydraulic fractures.

2. COMPUTATIONAL METHODOLOGY

2.1. Kerogen Pore Model

Depending on its geographic origin, sediment burial and maturation history, kerogen exhibits strong heterogeneity in its physical and chemical properties such as bulk density, chemical composition and pore structure. In particular, maturity indicators such as vitrinite reflectance, aromatic/aliphatic ratio, and atomic ratios (H/C and O/C) are used to categorize kerogen types. See the original work by van Krevelen (1961) for details. As the maturation develops over geologic time, relative carbon content increases, hence H/C and O/C atomic ratios decrease. To date the effects of the amount, type and thermal maturity of the organic matter on the hydrocarbons storage in source rocks have been extensively investigated (Weniger et al. 2010; Modica and Lapierre 2012; Gasparik et al. 2012; Zhang et al. 2012; Bui et al., 2018).

Throughout molecular simulation study, the porous structure of kerogen is simplified and modeled as a membrane made of carbons consisting of slit-shape pores as shown in Figure 2.1. Chemically, the graphite includes carbon atoms only and represents the extreme case of thermal maturity (H/C and O/C atomic ~ 0) for the kerogen. Other types of nanopores in source rocks such as clay and calcite are not considered here. Our focus is on the complexity of the fluids, and the solid surface heterogeneities are not considered in this study. The level of confinement is controlled in the z-direction, and the sizes of the pores in x- and y-dimensions are fixed. Similar approach is adopted to study pure CH_4 or CO_2 in nanopores in literature (Liu and Wilcox 2012; Rahmani and Akkutlu 2015).

2.2. Composition Re-Distribution

Based on the typical subsurface conditions and the produced fluid composition, the in-situ hydrocarbon configuration in model kerogen nanopores can be estimated based on the composition re-distribution computations (Figure 2.2) using the molecular Monte Carlo (MC) simulation (Bui and Akkutlu 2017). The confined fluids in nanopores are assumed to be thermodynamically in equilibrium with the bulk fluid outside in the fracture. This requires the chemical potential of individual components is the same in both places. Throughout the study, the term bulk indicates the space outside the nanopores in places such as natural fracture or micro-crack, and the bulk fluid refers to the fluid residing therein. Also, fluid pressure refers to pressure of the bulk phase fluid in the fracture, and only the bulk phase fluid pressure is controlled in this study because the compressional stresses in confined fluids are strongly anisotropic (Bui and Akkutlu 2015).

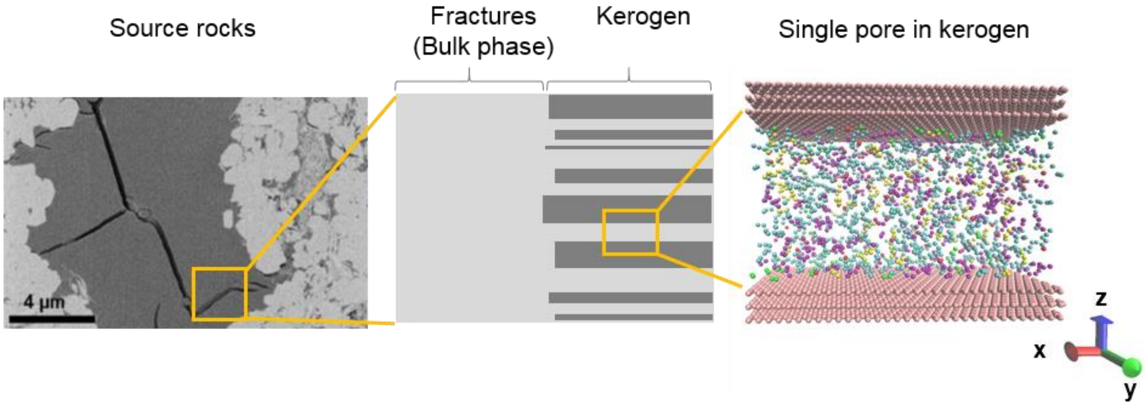

Figure 2.1 Pore consideration in molecular simulation (Baek and Akkutlu 2019c).

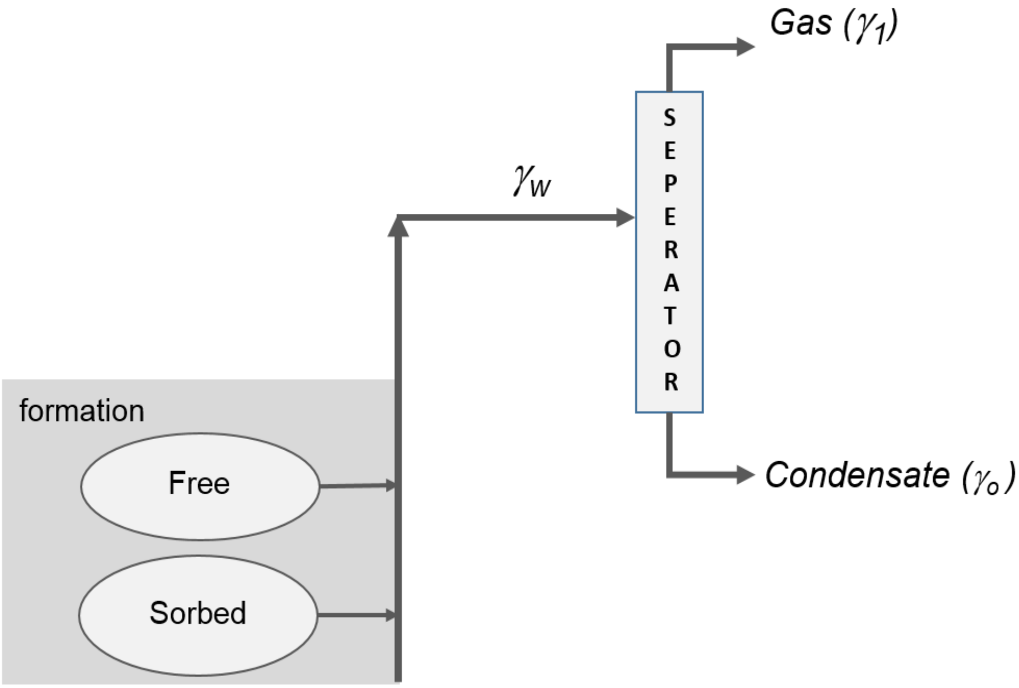

Figure 2.2 Conceptual model of composition re-distribution of the produced fluids for organic-rich source rock formations (Baek and Akkutlu 2019a).

2.3. Monte Carlo Molecular Simulation

The composition redistribution calculations are based on the Grand Canonical Monte Carlo (GCMC) molecular simulations and use open-source, TOWHEE (Martin 2013). During the GCMC simulation, the following five types of moves are used: volume exchanges with the external bath based on the pressure, center-of-mass translation and rotation, configurational-bias partial molecule re-growth and configurational-bias single box molecule re-insertion move. Firstly, using isothermal-isobaric (NPT) ensemble – inputs with the constant number of molecules, pressure and temperature, chemical potential of the individual component in the bulk fluid mixture is computed. Fifty thousand cycles are run for both the equilibrium and the production data, respectively. Then, using the chemical potential values of the components predicted, the GCMC or μVT ensemble - inputs with the constant chemical potential of individual component, volume of the system, and temperature, is run, and the number of each component in the nanopore is predicted. GCMC simulation maintains the same chemical potential of the individual component in the nanopore and in the bulk fluid residing in the micro-crack, which are in accordance with those from NPT simulation. 40 million cycles of computation are performed for the membrane-crack system to reach equilibrium state and for data production. The equilibrium state is confirmed with small difference in the chemical potential between bulk phase and nanopores for NPT simulation as seen in literature (Bui and Akkutlu 2017). For GCMC (or μVT) simulation, the mole fraction of the individual component in the nanopore has less than 0.005 of standard deviation over production run.

The numbers of cycles for NPT and μVT simulations were enough to make the system reach equilibrium (Pitakbunkate et al. 2016).

Molecular interactions of hydrocarbons are described with the TraPPE force field cost (Martin and Siepmann 1998 and 1999), and all hydrocarbons are modeled as united-atoms. In the united-atom force field, the single interaction sites, so called pseudo-atoms are used to represent a carbon atom together with all of its bonded hydrogen atoms to save the computational. Lennard-Jones 12-6 potential is adopted to model the non-bonded interaction and van der Waals intermolecular interactions (Eq. 2.1). Lorentz-Berthelot mixing rule is employed for interactions between unlike particles (Eq. 2.2). All pseudo-atoms are connected by a fixed bond length (1.54 Å), bond bending is governed by a harmonic potential (Eq. 2.3) and the motion of the dihedral angles $\emptyset$ is controlled by OPLS united-atom torsional potential (Eq. 2.4).

$$U_{ij}(r_{ij}) = 4\varepsilon_{ij}\left(\left(\frac{\sigma_{ij}}{r_{ij}}\right)^{12} - \left(\frac{\sigma_{ij}}{r_{ij}}\right)^{6}\right), r_{ij} < r_t \tag{2.1}$$

$$\sigma_{ij} = \frac{1}{2}\left(\sigma_{ii} + \sigma_{jj}\right)$$

$$\epsilon_{ij} = \sqrt{\epsilon_{ii}\epsilon_{jj}} \tag{2.2}$$

$$u_{bend}(\theta) = \frac{k_\theta}{2}\left(\theta - \theta_{eq}\right) \tag{2.3}$$

$$u_{torsion}(\emptyset) = c_1[1 + cos(\emptyset)] + c_2[1 - cos(2\emptyset)] + c_3[1 + cos(3\emptyset)] \tag{2.4}$$

Table 2.1 Bonded and non-bonded interaction parameters.

Pseudo-atom	ϵ/k_B [K]	σ [Å]	q [e]
CH_4	148	3.73	-
CH_3-	98	3.75	-
-CH_2-	46	3.95	-
C in CO_2	27	2.8	0.70
O in CO_2	79	3.05	-0.35

Stretch	Length [Å]
CH_x- CH_y or CH_y- CH_x	1.54
O=(C=O) or O=(C=O)	1.16

Bend	θ_{eq} [°]	k_θ/k_B [K/rad^2]
CH_x-CH_2-CH_y	114	62,500
O=(C)=O	180	-

Torsion	C_o/k_B [K]	C_1/k_B [K]	C_2/k_B [K]	C_3/k_B [K]
CH_x-CH_2-CH_2-CH_y	0.00	355.03	-68.19	791.32

CO_2 is simulated with three-site rigid model (θ = 180°) having point charge on the carbon atom (q_c = +0.7e) and on each of the oxygen atoms (q_o = -0.35e) in order to take into account its intrinsic quadrupole moment. Lennard-Jones 12-6 potential is adopted to model the non-bonded interaction and van der Waals intermolecular interactions, and the permanent electrostatic interactions are computed with Ewald summation of the point partial charges for CO_2-CO_2 interactions. The Ewald convergence parameter, α is set to 5.6 divided by the shortest simulation box length, and the maximum number of inverse space vectors (k_{max}) is 5. The detailed parameter values are given in Table 2.1.

A cut-off distance of 13.8 Å is used, and analytical tail correction is applied to estimate the effects of long-range molecular interactions. The solid-fluid interaction potential ϕ_{sf} for hydrocarbons interacting with the organic nanopore wall is well described by the Steele 10-4-3 potential (Steele 1973).

$$\phi_{sf}(\mathrm{z}) = 2\pi\epsilon_{sf}\rho_s\sigma_{sf}^2\Delta\left[\frac{2}{5}\left(\frac{\sigma_{sf}}{\mathrm{z}}\right)^{10} - \left(\frac{\sigma_{sf}}{\mathrm{z}}\right)^4 - \frac{\sigma_{sf}^4}{3\Delta(\mathrm{z}+0.61\Delta)^3}\right] \tag{2.5}$$

where z is the distance from the pore wall, ρ_s is the solid density, Δ is the spacing between carbon layers, and ε_{sf} and σ_{sf} are the well depth and effective diameter for the hydrocarbons and carbon wall, which are determined by Lorentz-Berthelot mixing rule. We fix ρ_s = 0.114 atoms/Å^3 and Δ = 3.35 Å. For the model slit pore, the fluid molecule will interact with both carbon slabs and hence, the full external potential V_{ext} is written as

$$V_{ext}(\mathrm{z}) = \phi_{sf}(\mathrm{z}) + \phi_{sf}(\mathrm{H}-\mathrm{z}) \tag{2.6}$$

2.3.1. Simulation Validation

For validation of the molecular simulation-based approach, firstly, one hydrocarbon mixture (methane: ethane: propane: n-butane: n-pentane = 0.54: 0.16: 0.13: 0.11: 0.06) and pure CO_2 fluid are compared over typical reservoir pressure in Figure 2.3a. Both fluids are simulated in the bulk phase using NPT ensemble at 176 °F. Peng-Robinson equation of state and NIST database are used for the comparisons. Figure 2.3a shows that the fluid models are in agreement for the entire range of pressure investigated. Next, the

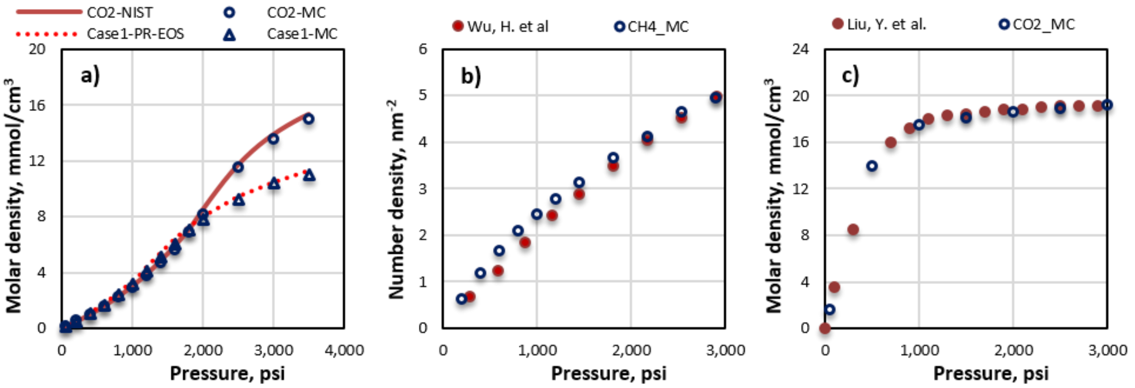

Figure 2.3 Computational methodology validation (Baek and Akkutlu 2019b).

comparison is made for pure methane and pure CO_2 in model kerogen pore. In both cases, the average density over the entire nanopore volume is counted. In Figure 4.4b, Wu et al. (2017) computed the number density (the number of molecules per pore volume multiplied by the pore size) of pure CH_4 using molecular dynamics simulation at 176 °F. The unit of y-axis in Figure 2.3b is displayed as given in their work. Their simulation had a large bath of the bulk phase connected to the nanopore, and they adopted the mixed wall model, which includes the one explicit carbon layer and implicit wall potential for consecutive layers. Their simulation result is matched using the simulation approach of this study with the implicit Steele's wall potential. Likewise, in Figure 2.3c, the 2 nm pore generated a consistent molar density (the number of molecules per pore volume) for pure CO_2 at 104 °F when compared to the results previously published by Liu and Wilcox (2012). These results gave confidence on the developed computational methodology for the fluids and the model pores and encouraged us to look into the behavior of the multi-component fluids in organic nanopores under the effects of competitive adsorption and nanopore confinement effects.

2.3.2. Recovery Calculation

In order to assess the performance of the injected gases, hydrocarbons recovery from the nanopores is calculated using the composition re-distribution data from Monte Carlo molecular simulations and Eq. 2.7:

$$\text{Recovery, \%} = \frac{C\left(P_i,\ d_p\right) - C\left(P,\ d_p\right)}{C\left(P_i,\ d_p\right)} \times 100, \tag{2.7}$$

in which $C(P, d_p)$ is molar density of the fluid in the nanopore with the size d_p at pressure P. This value points out hydrocarbon in-place in the nanopore at a particular pressure. P_i is the initial pressure and equal to 4,000 psi in this study.

2.4. Molecular Dynamics Simulation

Molecular Dynamics (MD) simulation is performed separately for the redistributed hydrocarbons in each pore to compute the transport properties such as viscosity, the mean free path length, and diffusivity of the hydrocarbon molecules using the computed trajectories of the molecules. Large-scale Atomic/Molecular Massively Parallel Simulator (LAMMPS) is adopted for the MD simulations (Plimpton 1995). The same molecular interaction parameters are used (Table 2.1). In-house MATLAB codes are used to build input files and analyze results and trajectories.

2.4.1. Viscosity Calculation

The viscosity of the confined mixtures is measured using Green-Kubo relation as (Chen et al. 2009):

$$\eta = \frac{V}{K_B T}\int_0^\infty \langle \sum_{\alpha\beta} P_{\alpha\beta}(0)P_{\alpha\beta}(t)\rangle \, dt \tag{2.8}$$

$$P_{\alpha\beta} = \frac{1}{2}\left(\sigma_{\alpha\beta} + \sigma_{\beta\alpha}\right) - \frac{1}{3}\delta_{\alpha\beta}\left(\sum_{\alpha\beta}\sigma_{yy}\right)$$

where K_B, Boltzmann constant, $P_{\alpha\beta}$, symmetrized traceless portion of the stress tensor, $\sigma_{\alpha\beta}$, $\delta_{\alpha\beta}$ is the Kronecker delta and $\delta_{\alpha\beta} = 0$ when $\alpha \neq \beta$. Viscosity calculation with MD equilibrium simulation reasonably predicts the viscosity of multi-component hydrocarbon fluids in bulk phase (Bui and Akkutlu 2017).

2.4.2. Fluid Average Diffusivity Calculation

The average diffusivity of the fluids in nanopores of the membrane are estimated based on the mean free path and the mean collision time of the molecules measured using MD simulation (Gottlieb et al. 2013). By definition, the mean free path is the average distance the fluid molecules take between successive collisions, and the mean free collision time is the average time between the collisions. The mean free path length of multi-component hydrocarbons in confined space can be calculated using the generated trajectories from the molecular simulation as follows:

$$\lambda_i = \frac{\sum r_i^t - \sum r_{i,c}}{m_i} \tag{2.9}$$

$$\lambda_{ave} = \frac{\sum \lambda_i}{N} \tag{2.10}$$

Non-collisional traveling distance λ_i of a particle i can be measured by subtracting the distance, $\sum r_{i,c}$ the particle move during the collisions from the total distance $\sum r_i^t$ the molecule travels during the entire simulation time. m_i and N indicate the number of free flight of the particle i and the total number of the molecules in the system, respectively. The average diffusivity of the redistributed hydrocarbon mixture inside the nanopore is computed using:

$$D = \frac{1}{3}\lambda_{ave} v_{ave} = \frac{1}{3}\frac{{\lambda_{ave}}^2}{\Delta\tau}, \tag{2.11}$$

in which λ, v_{ave}, and $\Delta\tau$ are the mean free path, average molecule velocity and the mean free collision time, respectively. The ratio of the mean free path length to the collision time is the average molecule velocity, namely, $v_{ave} = \lambda_{ave}/\Delta\tau$.

2.4.3. Self-Diffusivity Calculation

Self-diffusivity (D_s) of injectant in the mixture is estimated from the mean-square displacement (Einstein equation, Eq. 2.12). For the hydrocarbons in nanopores, interlayer diffusion parallel to the basal surface (xy- plane) is considered (Greathouse et al. 2016).

$$D_s = \frac{1}{4}\lim_{t\to\infty}\frac{\langle [r_i(t) - r_i(0)]^2 \rangle}{t} \tag{2.12}$$

where $r_i(t)$ is the position of Center-of-Mass (COM) of the injectant molecule i at time t, and the angle brackets indicate an ensemble average over all injectant molecules and all time origins. The displacement between 0.1 – 4.5 ns was chosen for linear fitting, and 70 different simulations were used to reduce uncertainties.

2.5. Reservoir Flow Simulation

In chapter 6, an in-house flow simulator, *NaSh*, is used for forward simulation and history-matching. *NaSh* is a robust compositional reservoir flow simulator. The main features of the simulator are as follows:

- Multi-scale pore structure is considered including pores, micro-cracks, discrete natural fractures and hydraulic fractures.
- Pore-size distribution is accounted for:
  - Pore volume partitioned into nanopores with confined fluids, large pores with bulk fluid, and discrete fractures with bulk fluid,
  - Multi-scale coupling among nanopores, large pores and fractures,
  - Confinement effect in nanopores considered using molecular simulation; no EOS needed,
  - Phase change, capillarity, and stress-dependent flow in large pores.
- Geomechanics is accounted for
  - Viscoelastic deformation of the hydraulic fractures (proppant embedment),

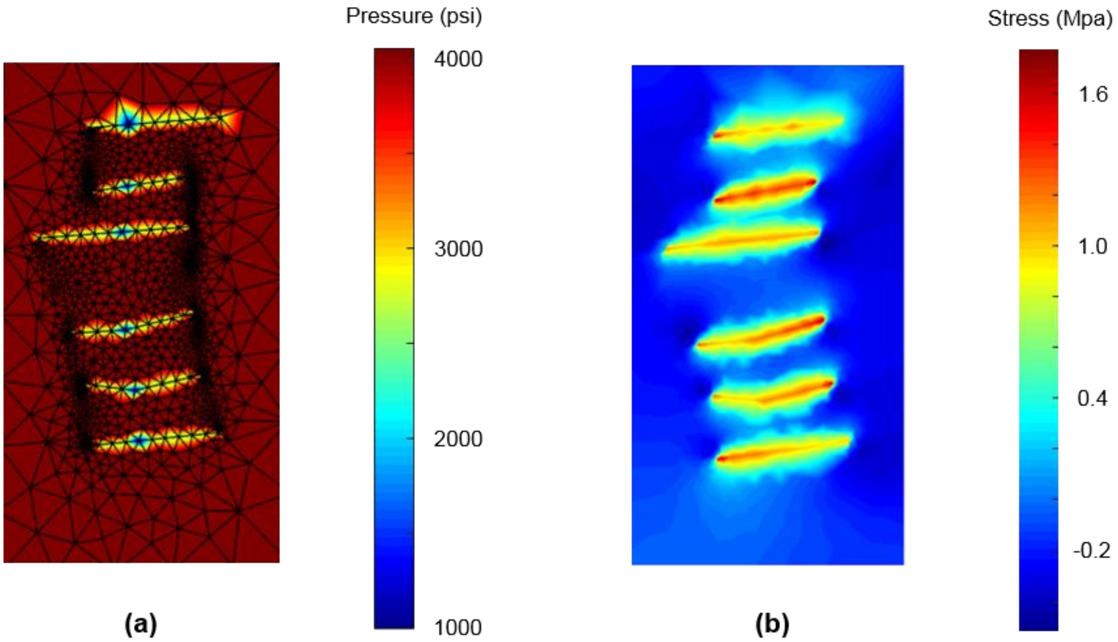

Figure 2.4 *NaSh* couples molecular simulation.

- Fracture conductivity change due to closure stress and plastic deformation,
- Embedded Discrete Fracture Model (EDFM) used for the discrete fractures.
- Dynamic (stress-sensitive) matrix permeability.

Gangi’s micro-fracture dominated permeability model (1978) is considered to capture the dynamic permeability of the matrix. Wasaki and Akkutlu (2015) previously showed the application of this method to the shale gas reservoirs. In this model, the permeability of the matrix (k) is stress dependent as follows:

$$k = k_0 \left[1 - \left(\frac{p_c - \alpha p}{p_{max}}\right)^m\right]^3 \tag{2.13}$$

where k_0 is the permeability of the matrix in the absence of stress, (p_c—αp) is the stress on the matrix, p_{max} is the maximum stress when the micro-fractures in the matrix entirely close. Exponent m represents the resistance of the micro-fractures to close under stress and is also related to the roughness of the micro-crack surfaces. During the optimization the Gangi's permeability model parameters k_0, m, and p_{max} will be treated as the calibration parameters, whose average values and their range can be determined based on the laboratory measurements of the formation sample core plugs maintained under controlled stress conditions as well (Kim, Olorode and Akkutlu 2019). The simulation model is fully-coupled geo-mechanically, hence not only the fluid pressure and saturations are computed dynamically, but also the changing stresses and the displacement are predicted (Olorode, Akkutlu, and Efendiev 2017a and 2017b). Figure 2.4 shows the computed pore pressure and stress during the gas production from a well.

The simulation model also considers the proppant embedment problem of the hydraulic fractures as a plastic deformation using a viscoelastic model originally proposed by Guo and Liu (2012):

$$\Delta w_f = w_0 \left[\frac{(1 - v^2)}{E_f} \sigma'_{xx}(t) + \frac{1}{4\eta} \left(1 + \frac{(1 - 2v)^2}{3} \right) \int_0^t \sigma'_{xx}(t)\, dt \right] \tag{2.14}$$

where Δw_f is the change in fracture width due to proppant embedment, w_0 is the initial fracture width, v is Poisson's ratio of the shale, E_f is the Young's modulus, η is the viscoelastic shear coefficient and $\sigma'_{xx}(t)$ is the time-dependent effective compressive stress acting on the surface of the hydraulic fractures.

2.6. Differential Evolution Algorithm

A gradient-free optimization algorithm, Differential Evolution (DE) is adopted in this work. DE basically consists of four steps of initialization, mutation, crossover, and selection. In the first stage, a population is randomly generated as many as population size (*NP*) within the variable range we initially set. In the second mutation step, new population is generated with the randomly chosen three (x_1, x_2 and x_3) vectors of initial population. They are created as $u_1 = x_1 + F(x_2 — x_3)$. *F* is a scaling factor, and used to perturb the selected solution and facilitate a population evolution. The crossover step varies the generated new candidate solutions (trial or offspring vector) on the basis of the corresponding parent vector and the crossover probability rate (*Cr*). Finally, the solutions with lower values of the cost function survive and become the parents for the next generation (selection). This process is repeated until the termination criteria (pre-specified tolerance level or maximum number of generation) is met (Goldberg 1989).

Table 2.2 Parameters of Differential Evolution Algorithm.

Parameters	Symbol	Value
Number of population	*NP*	Number of variables + 3
Scaling factor	*F*	0.618
Crossover probability rate	*Cr*	0.9
Max. Number of generation	*NG*	100

3. PRODUCED-FLUID COMPOSITION REDISTRIBUTION IN SOURCE ROCKS[1]

Source rocks, such as organic-rich shale, consist of multi-scale pore structure, which includes pores with sizes down to nano-scale contributing to the storage of hydrocarbons. In this study, we show that the hydrocarbons in the source rock partition into fluids with significantly varying physical properties across the nanopore size distribution of the organic matter. This partitioning is a consequence of multi-component hydrocarbon mixture stored in nanopores showing a significant compositional variation with the pore size. The smaller the pore is, the heavier and the more viscous the hydrocarbon mixture becomes. The concept of composition redistribution of the produced fluids is introduced using equilibrium molecular simulation that considers organic matter as a graphite membrane in contact with a micro-crack holding the bulk phase produced fluid.

A new equation of state is proposed to predict density of the recombined fluid mixtures in nanopores under the initial reservoir conditions. A new volumetric method is presented honoring the density variability across the measured pore size distribution for an improved accuracy in predicting hydrocarbons in-place. The approach allows us to account for the bulk hydrocarbon fluids and the fluids under confinement.

Multi-component fluids with the redistributed compositions are capillary-condensed in nanopores at the lower end of the pore size distribution of the matrix (< 10 nm). The

---

[1] This chapter is from SPE-195578-PA "Produced-Fluid Composition Redistribution in Source Rocks for Hydrocarbon-In-Place and Thermodynamic Recovery Calculations" written by Seunghwan Baek and I. Yucel Akkutlu. It is reprinted here with permission of SPE J., whose permission is required for further use.

nano-confinement effects are responsible for the condensation. During production and pressure depletion, the remaining hydrocarbons become progressively heavier. Hence, vaporization of the hydrocarbons and desorption develop at extremely low pressure. Consequently, hydrocarbon recovery from these small pores is characteristically low.

3.1. Preliminaries

Adsorptive properties of hydrocarbon fluids in the nanoporous organic materials, such as kerogen and bituminous coal, have been investigated using molecular simulations. Simple pore models with organic walls such as slit-pores with graphite walls have widely been used in these studies, and the focus was on providing new insights into fluid storage at the microscopic scale (Ottiger et al. 2008; Adesida et al. 2011; Ambrose et al. 2012; Mosher et al. 2013; Li et al. 2014). Cristancho-Albarracin et al. (2017) showed that a 4 nm pore contains roughly 50 % adsorbed hydrocarbons depending on the reservoir pressure and temperature. Also, they studied methane-nanopore wall interaction energy using quantum mechanical calculations to take into account the wall surface heterogeneities on the amount of methane adsorption. They compared the energy difference among the walls made of pure graphene, nitrogen-doped graphene, di-vacancy graphene and Stone-Wales effects and concluded that the impact of surface heterogeneities is significant on the adsorbed gas amount. Aljamaan et al. (2017) studied adsorption of pure gases using a molecular simulation and compared the results with experimental data using intact cores obtained from Haynesville and Barnett shale formations. All of these studies adopted a slit-shape carbon model in their analysis. However, these investigations have limited their scope to simple fluids, and they have been mostly performed under non-representative reservoir conditions. This work focuses on multi-component fluid systems and shows the importance of the in-situ composition on the fluids storage in source rocks.

Recent advances in the area of resource assessment, such as the shale gas in-place calculations proposed by Ambrose et al. (2012), considers *a priori* knowledge on the apparent molecular weight/density ratio of the adsorbed phase. Finding this ratio could be a difficult task, however, if the fluid is multi-component, and the composition is pore-size dependent (Hartman et al. 2011). Further, due to nano-scale confinement, the adsorption of the reservoir fluid may not follow the mono-layer Langmuir theory (Myers et al. 1968; Ruthven et al. 1984; Clarkson et al. 2000) but instead is characterized by a high-density excess fluid, which appears as semi-liquid on the density profile across the diameter of the pore (Dubinin 1960; Tsai et al. 1985; Ambrose et al. 2012; Heller and Zoback 2014; Aljamann et al. 2017). In addition, the formation volume factor becomes a vague quantity when dealing with the hydrocarbon mixtures in small pores in the presence of nano-confinement effects. It is often not possible to differentiate the fluid phases and their compositions in small pores by simply tracking the density variations.

In order to resolve these technical issues, in this study we revisit the multi-component hydrocarbon fluids occurrences in organic-rich source rocks. We present equilibrium thermo-dynamic computations based on molecular simulation of fluids under nano-scale confinement, to investigate the compositional variations of the hydrocarbons across the pore size distribution of the formation using the produced fluid composition. This method, called composition re-distribution of the produced fluids, is essential for resource assessment of the organic-rich source rocks. The redistribution is crucial for the initial hydrocarbon in-place considerations, for the reserve calculations including effective porosity associated with the mobile fluids, and, finally, for the prediction of the in-situ fluid transport properties. Although multi-component hydrocarbon fluids in nanopores have previously been studied (Stevenson et al. 1991; Arri et al. 1992; Clarkson et al. 2000; Jiang et al. 2005; Hartman et al. 2011; Collell et al. 2015; Rahmani and Akkutlu 2015; Bui and Akkutlu 2017; Obliger et al. 2016; Pitakbunkate et al. 2017), the concept of fluid composition redistribution and its application in resource assessment of the source rocks is new.

3.1.1. Nano-Confinement Effects

Figure 2.2 shows the concept of the composition redistribution of the produced fluids. Traditionally, the reservoir engineering studies require that the fluids collected from the separator be recombined for the subsequent analyses. The recombination calculations are well established (McCain 1990). Composition redistribution of the recombined fluid is important because the hydrocarbon fluids in the organic pores can have significantly varying composition (Stevenson et al. 1991; Arri et al. 1992; Clarkson et al. 2000; Hartman et al. 2011). This variation is different from the vertical compositional variation in thick conventional reservoirs (Mullins et al. 2004) but it is the consequence of the generated hydrocarbons expulsion and migration in the source rock. In organic-rich source rocks, the composition redistribution is necessary in the organic nanopores because their surfaces are in general hydrocarbon (oil) wet. Recent thermodynamic computations of multi-component hydrocarbon fluids proved that the composition in organic nanoporous materials is different from that of the bulk fluids due to the nanoscale confinement effects (Bui and Akkutlu, 2017).

3.1.2. New Conceptual Porosity Model for Source Rocks

The concept of composition redistribution is further illustrated in Figure 3.1 using a new conceptual porosity model for the organic-rich source rocks. Note that the composition redistribution is necessary only for the hydrocarbons stored in the organic nanopores. The inorganic porosity, where the hydrocarbon redistribution considerations may have existed, consists of the clay nanopores, which largely have already been taken by the formation water. The composition redistribution is needed for (i) partitioning the hydrocarbon porosity into large pore volume, which may include both organic and inorganic pores holding bulk hydrocarbon fluid, and the organic nanopore volume holding hydrocarbon molecules under the nano-confinement effects; (ii) separating the trapped hydrocarbons in the organic nanopores due to significant confinement. The trapped hydrocarbons are the molecules dissolved (absorbed) in those nanopores at the lower end of the pore size distribution. For multi-component systems the hydrocarbon dissolution and trapping in the organic nanopores, as we will see in the following pages, are also closely associated with the phenomenon of capillary condensation. Much like the clay-bound water, the trapped hydrocarbons in organic nanopores are under the strongest influence of the pore walls such that the hydrocarbon molecules have lost their ability to be transported under the influence of pressure and concentration gradients.

Separation of trapped and mobile hydrocarbons can be achieved after the redistribution computations by means of identifying two pore size cut-off values: (i) $d_{p,L}$

below which hydrocarbon fluids behave different from the bulk phase fluid due to nano-confinement effects; (ii) $d_{p,T}$ below which release of the hydrocarbon molecules is found negligible due to amplified attractive forces exerted by the pore walls, and the associated dramatic increases in the apparent molecular weight and viscosity of the fluid. These cut-offs may vary based on the produced fluid composition, surface chemistry of the pore wall and reservoir conditions. Similarly, a cut-off can be described to separate the immobile water from free water. Because mature source rocks are in general desiccated due to vaporization and removal of the formation water during hydrocarbon generation and migration, and hold water at sub-irreducible water saturation, a reasonable simplification for the inorganic porosity cut-off is to assume that, although it may take up a portion of

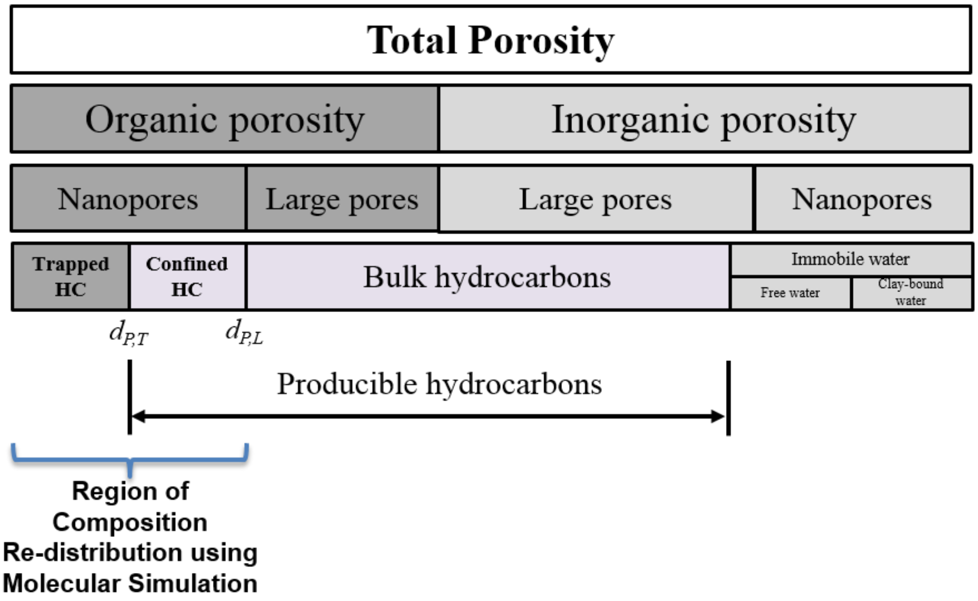

Figure 3.1 Conceptual porosity model for organic-rich source rock formations.

the total porosity of the formation, the free water is not mobile. The free and clay-bound water saturations can be measured in the laboratory using retort method. Heating of the sample is performed at different target temperatures suitable for vaporization of the free water and clay-bound water separately. Then the combined porosity of the free (ϕ_{FW}) and clay-bound water (ϕ_{CBW}) must be subtracted from the total porosity (ϕ). An effective porosity for mobile hydrocarbons (ϕ_{HC}) can then be used for the hydrocarbon in place and reserve calculations as follows:

$$\phi_{HC} = \phi - \phi_{trappedHC} - \phi_{FW} - \phi_{CBW} \tag{3.1}$$

$$\phi_{HC} = \phi_{Large} + \phi_{Nano} - \phi_{trappedHC} \tag{3.2}$$

where ϕ_{Large} represents the fraction of the hydrocarbon-filled organic and inorganic pores with the cut-off size larger than $d_{p,L}$ and ϕ_{Nano} is the fraction of hydrocarbon-filled organic pores with the size less than $d_{p,L}$.. $\phi_{trappedHC}$ stands for the fraction of the organic pores smaller than the cut-off nanopore size $d_{p,T}$. In the following section, a numerical approach is presented discussing in depth the new concepts introduced above.

3.2. Fluid Model

For the composition redistribution calculations, we consider three mixtures of hydrocarbon fluids produced from shale/tight formations. The compositions of the mixtures are shown in Table 3.1. Mixture 1 is a methane-rich natural gas; Mixtures 2 and 3 are the hydrocarbon mixtures with larger molecules from Zhang et al. (2013). They consist of five hydrocarbon components: methane (CH_4), ethane (C_2H_6), propane (C_3H_8), n-butane (n-C_4H_{10}), and n-pentane (n-C_5H_{12}). Figure 3.2 shows the pressure-temperature phase diagrams of the mixtures. The predicted two-phase envelops of Mixture 1 and Mixture 2 are located far below the reservoir temperature of 176 °F, which indicates that the fluids belong to a dry shale gas reservoir. Mixture 3 is somewhat different as a bulk fluid; the pressure path of isothermal expansion reaches tangent to its dew point at 1,250 psi and 176 °F. However, the liquid saturation is expected to be negligible in the reservoir; hence, Mixture 3 is wet-gas in the conventional sense. In this study we will show that Mixture 3, when redistributed in the organic nanopores, capillary-condenses in nanopores and stays condensed during pressure depletion.

The bulk fluid pressure conditions considered in the micro-crack are normally between 500-4,000 psi, and all the cases were assumed to be isothermal systems maintained at 176 °F (Gray dash line in Figure 3.2). The applied temperature and pressure conditions cover typical subsurface conditions corresponding to depths of several thousand meters (Ambrose et al. 2012).

Table 3.1 Molar composition (%) of bulk fluids used in the study.

Model Fluid	**CH_4**	**C_2H_6**	**C_3H_8**	**C_4H_{10}**	**C_5H_{12}**	**N_2**	**CO_2**
Mixture 1	98.2	0.66	0.01	-	-	0.91	0.22
Mixture 2	74.9	9.7	8.6	4.8	2.0	-	-
Mixture 3	53.8	16.4	12.7	10.5	6.6	-	-

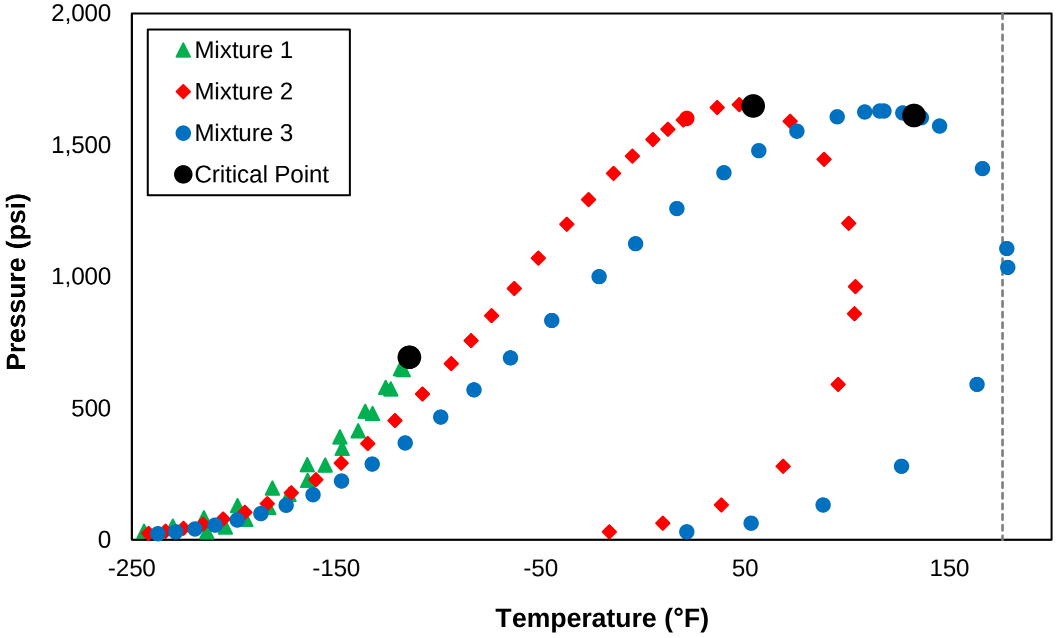

Figure 3.2 Pressure-temperature phase diagram of the produced fluid mixtures used in this study.

3.3. Results and Discussion

3.3.1. Composition Redistribution of the Produced Fluids in Nanopores

In general, the composition of the hydrocarbon mixture inside the nanopores varies due to the size of the pore, pressure and temperature (Stevenson et al. 1991; Jiang et al. 2005; Rahmani and Akkutlu 2015; Bui and Akkutlu 2017; Pitakbunkate et al. 2017). Figure 3.3 shows the compositional variations in nanopores for Mixture 3. In Figure 3.3 (Bottom) in comparison to the bulk fluid composition, the mole fractions of heavy components such as butane and pentane, increase in the hydrocarbon mixture inside the pore, while those of light components, such as methane and ethane, decrease. This is due to nano-confinement effects, as previously explained in Figure 3.1. Similarly, Figure 3.3 (Top) shows that the hydrocarbon mixture inside the 4.4 nm pores becomes progressively heavier and more viscous, when the pressure of the bulk fluid in the micro-crack is reduced. Since light components have relatively weaker affinity to the nanopore walls and have higher mobility (Falk et al. 2015), these molecules desorb from the model membrane easier during the depletion. We believe that the same arguments in Figure 3.3 can be extrapolated to mature organic materials in source rocks, such as kerogen and solid bitumen, with similar sizes of pores and capillaries but we should consider that the structural chemistry of the organic walls is more complex compared to graphite. Further investigation is needed to understand the compositional changes in confined fluids with controlled surface chemistry.

Note that the pore-size dependent compositional variation observed inside the organic nanopores is not considered during the conventional PVT calculations and the sorption isotherm tests. We are able to quantify this variability using equilibrium molecular simulations of hydrocarbons in graphite membrane in contact with a micro-crack. Below we present an approach that utilizes the redistributed compositions of the dense hydrocarbon mixtures in organic nanopores for the resource assessment of source rocks in the presence of nano-confinement effects.

3.3.2. Partitioning of Organic Nanopore Volume

Firstly, the redistributed hydrocarbon molecules inside the pores are quantitatively analyzed for the partitioning of the total hydrocarbon pore volume. Figure 3.4 shows the

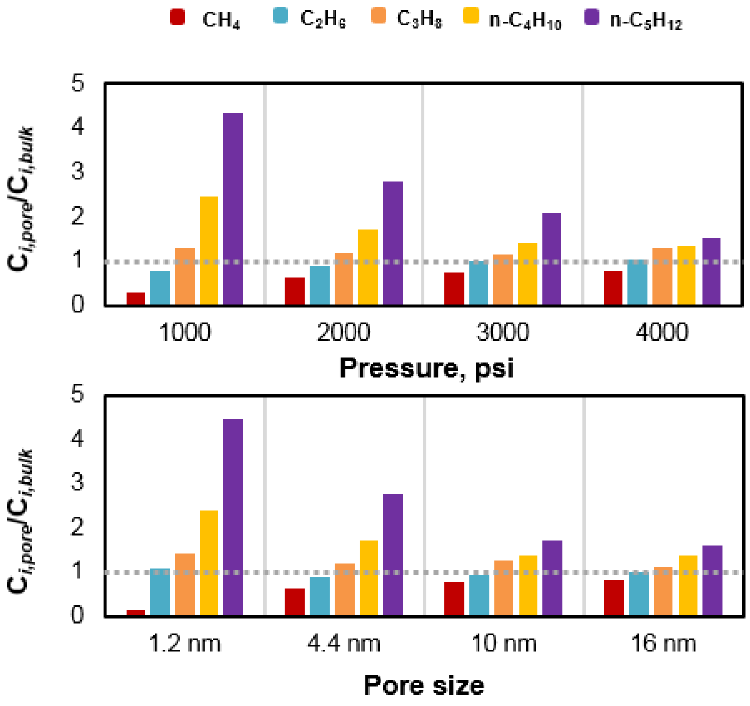

Figure 3.3 Compositional variation of Mixture 3 in nanopores.

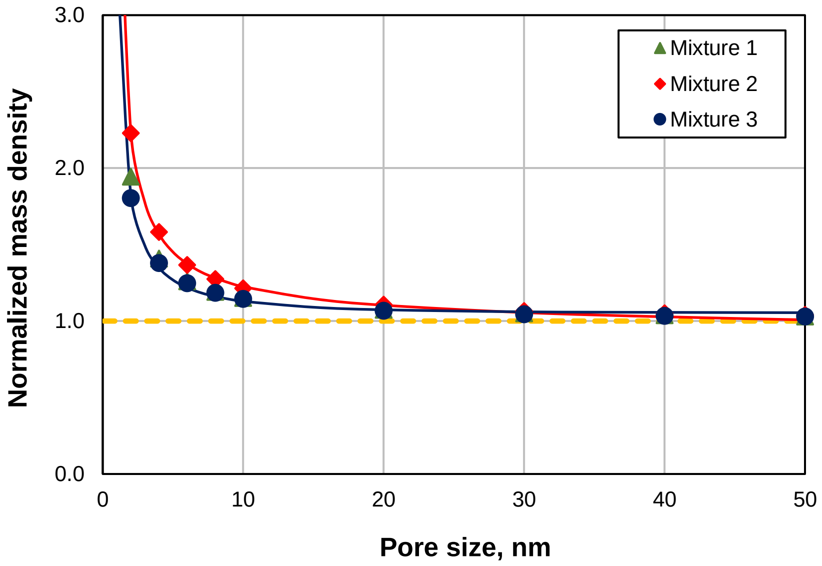

Figure 3.4 Normalized mass density of the hydrocarbon mixtures in nanopore with the bulk fluid density at 4,000 psi and 176 °F.

normalized mass density of the hydrocarbon molecules in nanopores with the corresponding bulk fluid density at the initial reservoir conditions of 4,000 psi and 176 °F.

Compared to the composition of the bulk hydrocarbon mixture outside in the micro-crack (shown as the dotted line), the predicted density varies due to the nano-confinement effects. The deviation from the bulk fluid behavior is larger in smaller pores. The crossing-point between the curve that belongs to the amount of molecules inside the pore, and the dash line of the bulk density indicates the cut-off pore size $d_{p,L}$ beyond which the nanopore effects disappear completely. In essence, this critical nanopore size splits the cumulative pore size distribution and partitions the total hydrocarbon pore volume into ε fraction of the large-pores (including both organic and inorganic pores) with bulk hydrocarbons, and (1- ε) fraction of the organic nanopores with the confined fluids, see Figure 3.5. Estimated $d_{p,L}$ value is 40 nm for all the mixtures. Several other hydrocarbon mixtures including volatile oils are tested, and they all have the same cut-off at given pressure and temperature conditions. This indicates an insensitivity to the redistributed fluid composition at high reservoir pressure. Note that, although 40 nm is the theoretical cut-off, practically the nano-confinement effects are major only in small nanopores with sizes less than 10 nm.

Constant value of $d_{p,L}$ and the similarities in normalized fluid mass density and pore size relationship for the three mixtures raise questions. If the trends have similarities regardless of the mixture composition, is it possible to predict the mass density of a redistributed fluid mixture in nanopore using its equilibrium bulk mass density measured

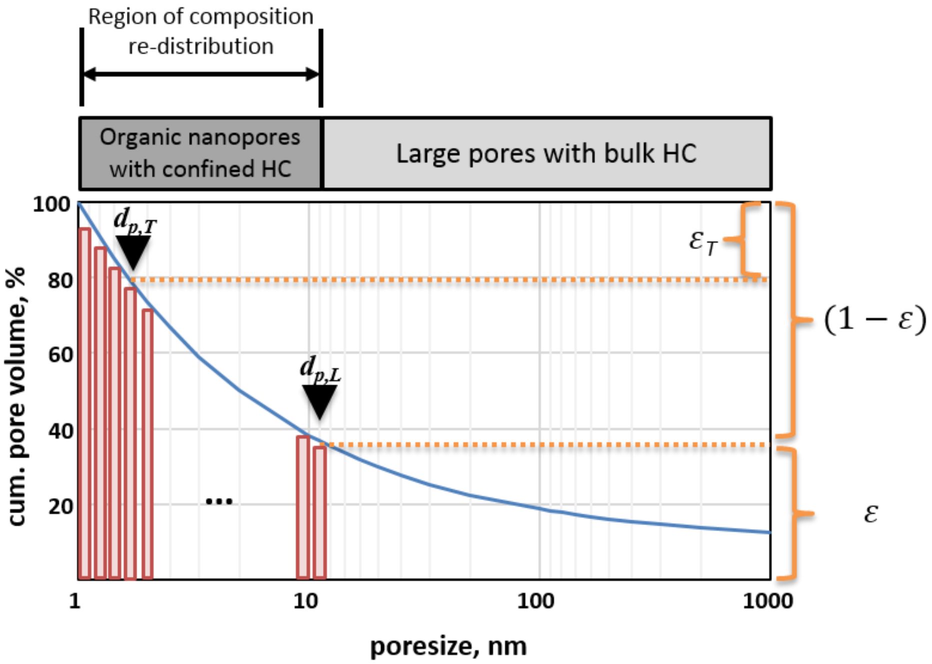

Figure 3.5 Diagram showing the treatment of organic nanopores with confined hydrocarbons using the cumulative pore volume distribution of an organic rich shale sample.

at the same pressure and temperature? Further, considering methane as the major constituent of the produced hydrocarbon fluids, is it possible to predict the mixture density for dry gas, wet gas and condensates as a function of the pure methane density? Being able to predict the mixture behavior with respect to methane has the added benefit because equation of state models for simple fluids such as methane including the nano-confinement effects exists in the literature (Vishnyakov 2001; Travalloni et al. 2010; Singh et al. 2011). In this study we show that the mass density of a redistributed hydrocarbon fluid mixture confined in nanopore with size d_p can be approximated with respect to methane using the following empirical relationship:

$$\frac{\rho_{dp,mix}/\rho_{bulk,mix}}{\rho_{dp,CH4}/\rho_{bulk,CH4}} = a \cdot \ln(d_p) + b \tag{3.3a}$$

$$a(\rho_{bulk,mix}) = -2.0072\rho_{bulk,mix}^2 + 2.0930\rho_{bulk,mix} - 0.4565 \tag{3.3b}$$

$$b(\rho_{bulk,mix}) = 6.1421\rho_{bulk,mix}^2 - 6.6553\rho_{bulk,mix} + 2.4843 \tag{3.3c}$$

In Eq. 3.3 d_p is the pore size in nanometers, and $\rho_{dp,CH4}/\rho_{bulk,CH4}$ is the normalized mass density of pure methane in the nanopore with respect to the bulk density. This ratio for methane is shown in Figure 3.4 and tabulated in Table 3.2 for 4,000 psi and 176 °F. It can be also predicted using currently existing equations of state for methane such as Travalloni et al (2010). $\rho_{bulk,mix}$ is the bulk fluid density of the mixture in micro-crack in g/cm^3. Here, $\rho_{bulk,mix}$ is obtained from GCMC. Alternatively, it can be calculated using the compressibility equation of state or Peng-Robinson.

Eq. 3.3 are derived based on 22 different fluid compositions, including Mixtures 2 and 3. It gives the mass density values of the redistributed hydrocarbon mixtures in nanopores with less than 5 % error (with respect to GCMC simulation) for dry gas, wet gas, and condensate consisting of light hydrocarbon mixtures rich in methane through pentane and having molar density of 0.18 – 0.5 g/cm^3. Note that the above discussion on the density predictions using Eq. 3.3 are strictly at the initial reservoir pressure and temperature conditions. It is anticipated that the equations will hold at higher pressures but one should be careful in their application at lower pressure due to depletion of the reservoir.

Table 3.2 Normalized density of pure methane in nanopores and $\rho_{dp,CH4}/\rho_{bulk,CH4}$ ratio at 4,000 psi and 176 °.

Pore size, d_p, nm	Normalized mass density $\rho_{dp,CH4}/\rho_{bulk,CH4}$	Normalized molar density $\rho_{dp,mol,CH4}/\rho_{bulk,mol,CH4}$
1	3.65548	3.64087
2	1.94324	1.93546
3	1.57235	1.56606
4	1.40869	1.40306
5	1.31717	1.31191
6	1.25958	1.25455
7	1.21883	1.21395
8	1.19046	1.18570
9	1.16814	1.16347
10	1.15051	1.14591
15	1.09921	1.09482
20	1.07433	1.07003
30	1.04978	1.04558
40	1.03837	1.03422
50	1.03045	1.02632

3.3.3. Capillary Condensation in Organic Nanopores and Trapped Hydrocarbons

Next, we focus on the hydrocarbon filled organic nanopore volume. Our target is to use the in-situ composition in nanopores to identify a cut-off size $d_{p,T}$ for the separation of trapped hydrocarbons shown in the porosity model given in Figure 3.1. Note that $d_{p,T}$ has a value in between zero and $d_{p,L}$. For this purpose, the molar density isotherms of the in-situ fluids in nanopores are shown in Figure 3.6. The figure shows thermodynamically the density of the hydrocarbons that are left in the nanopore during the pressure depletion. For Mixture 1, shown top left, the amount inside the nanopore proportionally decreases when the pressure is reduced. This indicates that these mixtures are proportionally producible as pressure is reduced. Behavior of Mixture 2 on the right is somewhat similar but the latter shows less sensitivity to nanopore size above 1,000 psi, and the pressure dependence is somewhat nonlinear. Note that Mixture 2 is much denser in nanopores. On the other hand, Mixture 3 at the bottom left has significantly different behavior. Firstly, its density in nanopores is large. Furthermore, the density is insensitive to pressure reduction, thus, the fluid has less compressibility. This indicates that Mixture 3 in nanopores is capillary-condensed. During depletion, its density shows a rapid change around 850 psi, which is within the phase transition region of the bulk fluid, indicating vaporization of the capillary condensed fluids. Phase diagram of Mixture 3 in bulk phase (shown in Figure 3.2) indicates that the fluid goes through the two-phase region at between 835 psi through 1,216 psi although the liquid saturation is anticipated to be negligible. In nanopores, however, nano-confinement effects have changed the composition of the fluids and, in turn, allowed phase transition at much lower pressures. In 6 nm pore the vaporization pressure of the capillary-condensed Mixture 3 is as low as 500 psi.

Pore size-dependent phase transitions cannot be captured correctly without redistribution calculations. This emphasizes the impact of composition, as controlled by the confinement effects, on the phase change. In Figure 3.6, molar density isotherm of pure ethane is also presented for comparison. Molecular weight of ethane (30.1 g/mol) is close to that of Mixture 3 (30.5 g/mol), but its bulk density (yellow line) is slightly higher than that of Mixture 3. Clearly, even though the density of ethane is higher, no phase change is observed for ethane in nanopores. The difference in behavior between pure ethane and Mixture 3 indicates that estimation of hydrocarbon in-place includes large uncertainties in the case of source rocks.

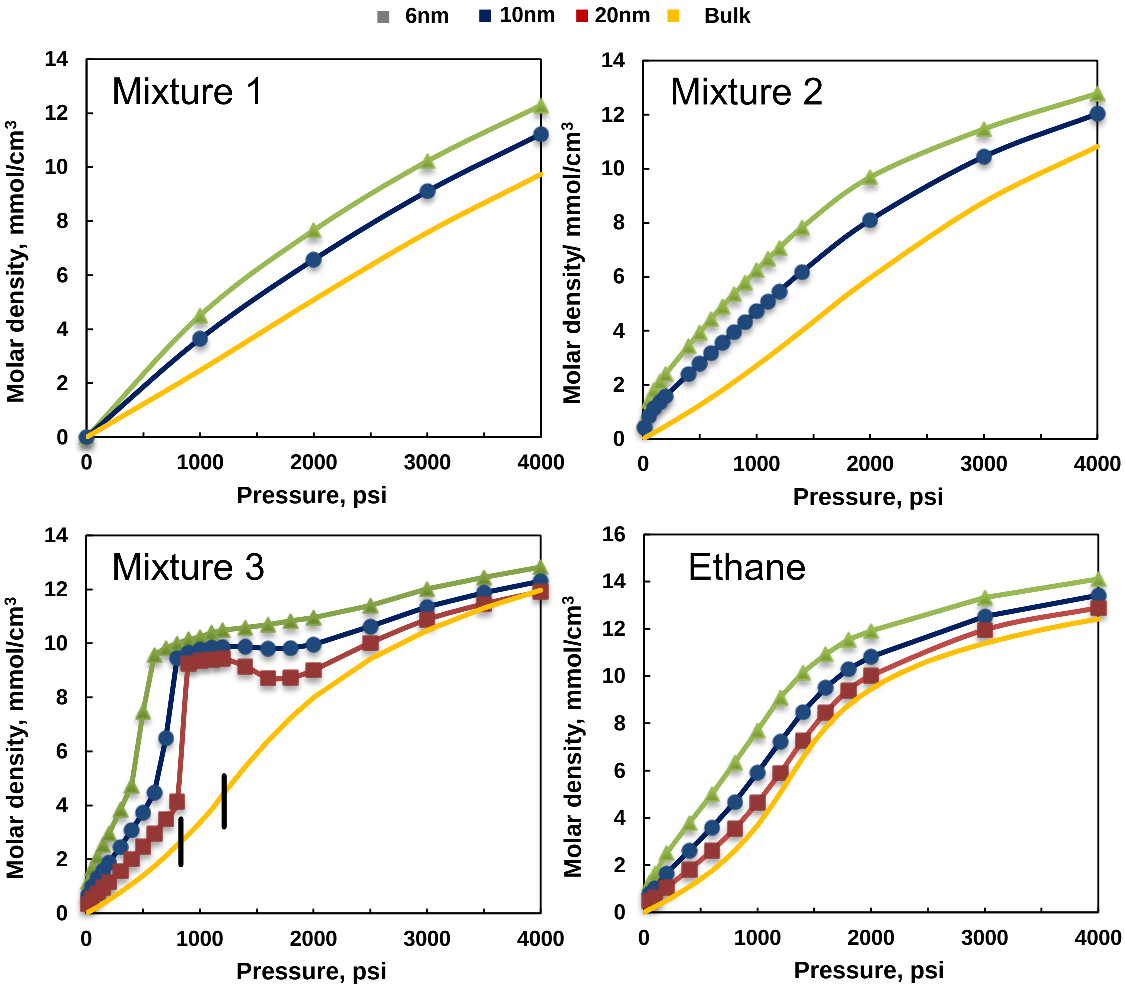

Figure 3.6 Adsorption isotherm curves at 176 °F.

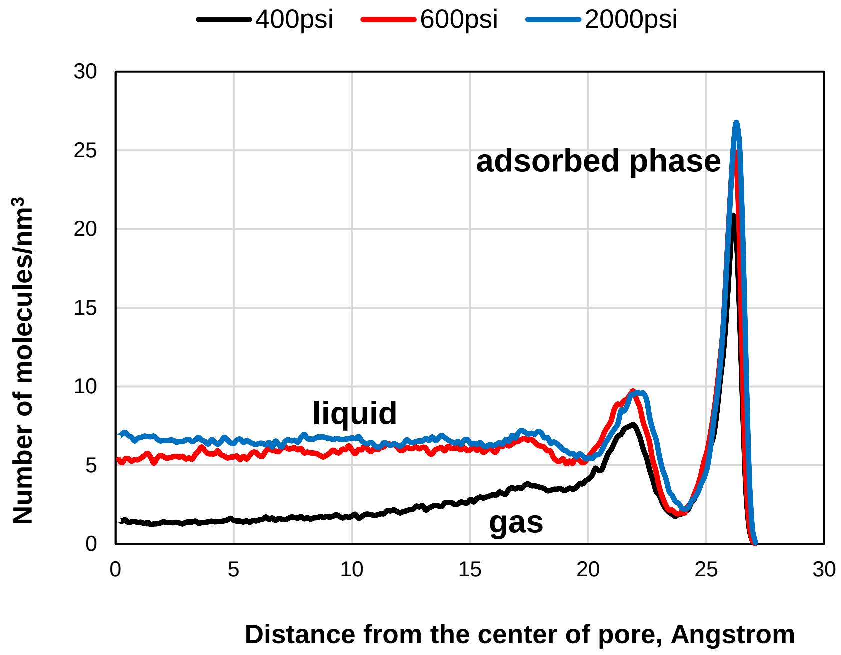

Figure 3.7 Liquid bridge formation of the redistributed hydrocarbon mixture in 4.4 nm pores.

Capillary-condensation is strongly dependent on the redistributed fluid composition in nanopore. Heavier mixtures can condense in larger nanopores. The condensed phase maintains much higher density in nanopore. In Figure 3.7, the density contrast in between the capillary condensed fluid and vaporized fluid is shown in 4.4 nm pore. The molecules of the condensed phase maintain a 2-3 times higher density compared to the gas phase. The distance among the condensed — liquid — molecules are much lower. Consequently, the attractive forces exerted by the pore walls penetrate deep into the center of the pore and influence a larger number of fluid molecules. Capillary condensed fluids have, therefore, significantly reduced mobility. The vaporized molecules, on the other hand, are not influenced by the walls as much as the liquid molecules due to larger distances they

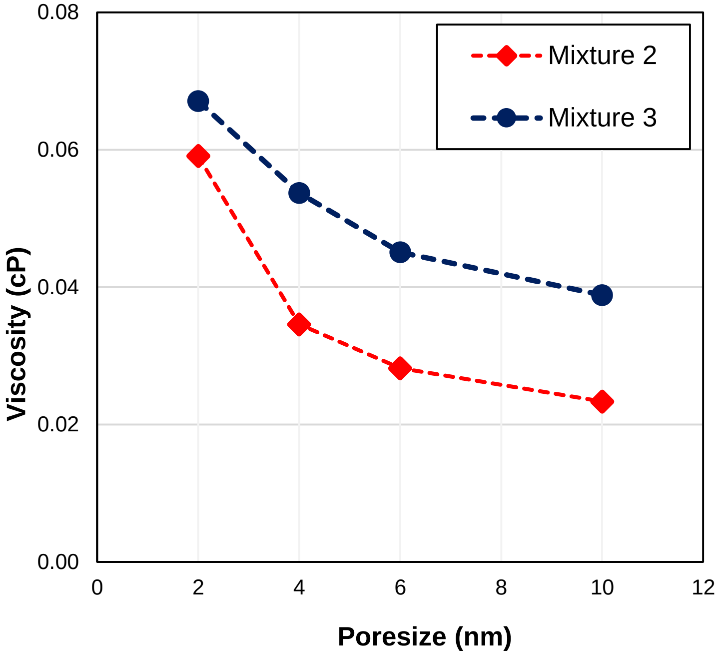

Figure 3.8 Viscosity of the redistributed hydrocarbon Mixture 3 in nanopores.

maintain among each other. So, the vaporized molecules can be released easier from the pore. This discussion is further supported by the estimated average viscosity of the hydrocarbon mixtures inside the nanopores. Figure 3.8 shows the predicted viscosity of the hydrocarbon mixtures in small pores varies several times higher than the viscosity of the bulk phase of Mixture 3. This is a dramatic increase in resistance to flow. Hence, in a practical sense, we conclude that the condensed hydrocarbon mixtures in nanopores can be deemed as trapped or non-producible hydrocarbons.

The discussion raises the need to identify a particular cut-off size for the trapped hydrocarbons in nanopores. This cut-off is shown in Figure 3.5 as $d_{p,T}$, which help us identify ε_T fraction of the total pore volume as the trapped hydrocarbon pore volume. In the following section we conduct the hydrocarbon in-place and reserve calculation with the identified cut-off sizes and their partitioned pore volumes. We will have further discussions on the trapped hydrocarbons when recovery from nanopores is discussed below.

3.3.4. Initial Hydrocarbon In-place Calculations in Presence of Nano-Confinement Effects

In order to show the impact of nanopores on the hydrocarbon in-place and recovery calculations, two organic rich shale samples with known pore-size distributions are used, Figure 3.9. Both samples have nanopores although Sample 1 is relatively richer in pores with sizes less than 10 nm (Shultz 2015). During the calculation, we use the reservoir parameters shown in Table 3.3. Combining with the cut-off sizes determined above, the predicted volume fraction ε of the large pores are summarized in Table 3.4. Here, the partitioning of the effective (non-trapped) hydrocarbon pore volume V_p into large pores and nanopores is considered. The hydrocarbon in place for the mixtures based on the conventional approach (Eq. 3.4a), and based on the composition redistribution approach including the nano-confinement effects (Eq. 3.4b) are as follows, respectively:

$$G(p) \;= 32.0368\frac{\emptyset(1-S_w)}{\rho_b B_g} = 1.2603\times10^6\times V_p\times n \qquad \text{(scf/ton)} \qquad (3.4a)$$

$$G^*(p) = 1.2603\times10^6\times V_p \times\left(\varepsilon\times n+\sum_{d_{p1}}^{d_{p,L}}\frac{V_{\%,d_p}}{100}\times n_{d_p}\right) \qquad \text{(scf/ton)} \qquad (3.4b)$$

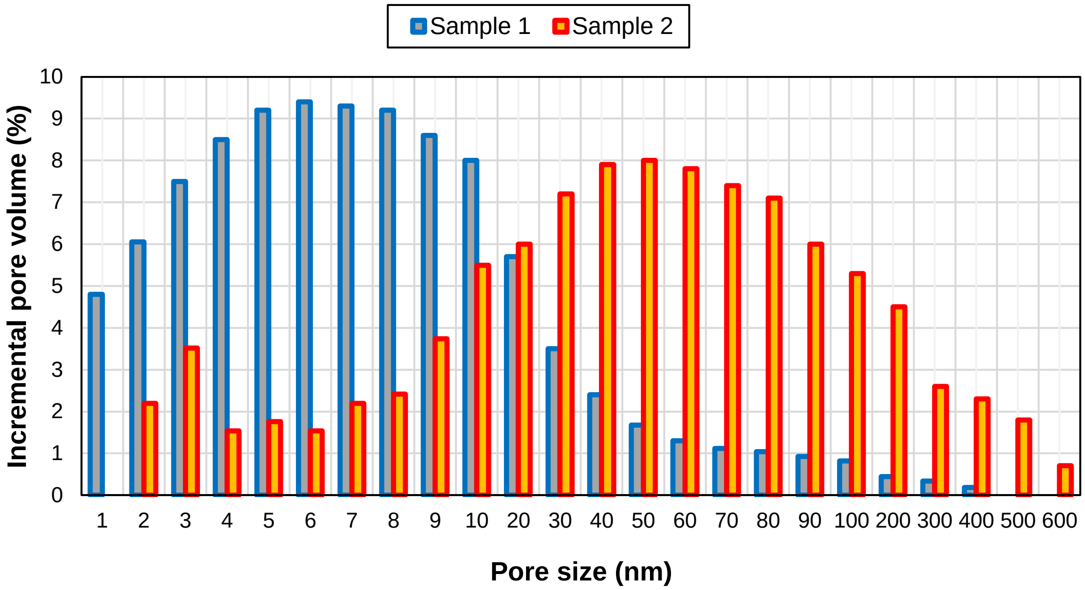

Figure 3.9 Pore size distribution of two organic-rich shale samples.

Table 3.3 Reservoir properties used in the calculations

Properties	**Values**	**Unit**
Bulk density, ρ_b	2.5	g/cm^3
Total porosity, ϕ	5	%
Immobile water saturation, S_w	35	%

In Eq. 3.4, $G(p)$ and $G^*(p)$ are the hydrocarbon in-place at pressure p. Note that we prefer using "hydrocarbon" in-place rather than gas in-place in our discussion even though the produced fluids are gas. This is because for fluids such as Mixture 3, a portion of the fluid in the organic nanopores is condensed. V_p is the effective hydrocarbon pore volume (cm^3/g) given as $\phi(1\text{-}S_w)/\rho_b$, where ρ_b, S_w, ϕ, and B_g are the bulk density of the rock in g/cm^3, water saturation, porosity and volume formation factor in ft^3/scf, respectively. n is the number of bulk hydrocarbon molecules stored in unit large pore volume under the reservoir pressure and temperature conditions (number/Å^3), and ε is the fraction of large pores which have the size larger than $d_{p,L}$. In addition, $V_{\%,dp}$ and n_{dp} are the pore volume percent contribution of the nanopore with size d_p in the source rock, as obtained from the measured incremental pore volume distribution vs. pore size data (Figure 3.5), and the number of hydrocarbon molecules in the nanopore per unit nanopore volume (number/Å^3), respectively. In Eq. 3.4b, the values for n_{dp} are computed using GCMC simulation. We use 40 nm as $d_{p,L}$. For the conventional approach, the number of molecules n is always the same regardless of the pore size. Appendix A gives the further details on Eq 3.4. Appendix B includes the predicted n_{dp} values for Mixtures 1, 2, and 3 using molecular simulation.

Table 3.4 shows the initial hydrocarbon in-place calculation results for the redistributed hydrocarbon mixtures. The change in hydrocarbon in-place amount in the absence of nano-confinement effects obtained using the conventional method is given as an error in the table: $(G\text{-}G^*)/G\times100$. The estimated values due to neglecting the nano-confinement effects show the error -14 % in Sample 2 and up to -37 % in Sample 1. The negative error indicates that the conventional approach leads to underestimation of the hydrocarbon in-place. Due to its larger pores, the nano-confinement effects are less pronounced in Sample 2. The nano-confinement effects vary with the pore size distribution and the fluid composition.

Table 3.4 Initial hydrocarbon in-place estimated at 4,000 psi 176 °F using in-situ hydrocarbon composition.

		Sample 1			Sample 2		
Model Fluid	***G*** scf/ton	*ε*	***G****** scf/ton	**Error** %	*ε*	***G****** scf/ton	**Error** %
Mixture 1	110.7	0.078	151.1	-36.5	0.545	119.2	-7.7
Mixture 2	107.9	0.078	128.7	-19.3	0.545	122.6	-13.7
Mixture 3	114.0	0.078	127.7	-12.1	0.545	117.6	-3.1

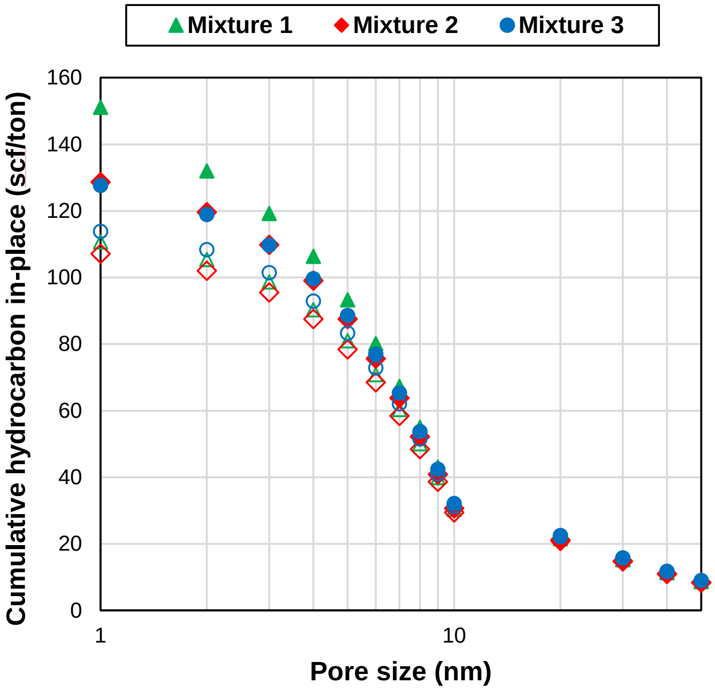

Figure 3.10 Cumulative initial hydrocarbon in place estimates for Sample 1 at 4,000 psi.

The result of the cumulative initial hydrocarbon in-place calculation is shown for Sample 1 in Figure 3.10. The filled data points include nano-confinement effects. In Eq. 3.4b, the incremental hydrocarbon in place at a particular pore can be calculated by discretizing the second term in parenthesis for the pore. Note that the most influential nanopores on the storage of hydrocarbons are those with sizes less than 10 nm.

In terms of the quantities used in the conventional reservoir engineering, the hydrocarbons in-place can be predicted per ton of source rock using the following equations (Ambrose *et al*. 2012):

Gas in place: $$G^*(p) = 32.0368\frac{\emptyset(1-S_w)}{\rho_b B_g^*} \quad \text{(scf/ton)} \qquad (3.8)$$

where, B_g^* is the modified formation volume factor of the fluid in the presence of nanopore confinement effects. Since Eq. 3.4b should be equal to Eq. 3.8, B_g^* is as follows:

$$B_g^* = \frac{4.22092 \times 10^{-5}}{\varepsilon \times \rho_{bulk,mol} + \sum_{d_{p1}}^{dp,L} \frac{V_{\%,d_p}}{100} \times \rho_{dp,mol}} \quad (\text{ft}^3/\text{scf}) \qquad (3.9)$$

In the denominator in Eq. 3.9, the first term is the contribution of the large pores with the volume fraction ε, and the second term is the contribution of the nanopores with the volume fraction, 1- $\varepsilon = \sum_{\boldsymbol{d_p}}^{\boldsymbol{d_{p,L}}} \boldsymbol{V}_{\%,\boldsymbol{d_p}}/\mathbf{100}$. Note that we have used the molar density, rather than the number of molecules, in Eq 3.10. $\rho_{dp,mol}$ is the molar density of the fluid in nanopore d_p in units of mol/cm^3. It can be calculated using the equation of state (Eq. 3.4a) but the latter needs to be written in terms of moles, instead of mass:

$$\rho_{dp,mol} = \left[c \cdot \ln(d_p) + d\right] \cdot \left(\frac{\rho_{dp,mol,CH4}}{\rho_{bulk,mol,CH4}}\right) \cdot \rho_{bulk,mol} \qquad (\text{mol/cm}^3) \qquad (3.10a)$$

where c and d are the new coefficients that are dependent on the molar density of the produced bulk fluid,

$$c = -26159.41\rho_{bulk,mol}^2 + 599.0111\rho_{bulk,mol} - 3.3265 \qquad (3.10b)$$

$$d = 92405.03\rho_{bulk,mol}^2 - 2121.03\rho_{bulk,mol} + 12.8323 \qquad (3.10c)$$

An example calculation using Eqs. 3.8-10 is included in Appendix C. The example shows how to avoid molecular simulations and, instead, use the empirical correlation given by Eq. 3.10 during the calculations.

3.3.5. Thermodynamic Recovery from Organic Nanopores

The rest of the discussion is on the molecular simulation results on the recovery. The approach involves the composition redistribution computations performed at various fluid pressure in micro-crack. Hydrocarbon recovery is estimated as per cent by comparing the hydrocarbon in-place at varying pressure, p to that at initial pressure p_i using the following equation:

$$\text{Recovery}(p) = \frac{G^*(p_i) - G^*(p)}{G^*(p_i)} \times 100 \qquad (3.11)$$

Here, p_i =4,000 psi and p takes the values of 1,000 psi, 2,000 psi and 3,000 psi. $G^*(p)$ is the hydrocarbon in-place including the nano-confinement effects, as given by Eq. 3.4b. This calculation points to a thermodynamic recovery of the redistributed hydrocarbon fluids due to pressure depletion. Note that we avoid using the equation of state (Eq. 3.10), because molecular simulation is more accurate in predicting the G^* values during the depletion. Figure 3.11 shows the hydrocarbons recovered from the individual pores for Mixture 1 (Left) and Mixture 3 (Right). The recovery curves of Mixture 1 show constant recovery for pores larger than 40 nm. In this region, the recovery of the bulk fluid is due to gas expansion. When the fluid pressure in the micro-crack is reduced to 3,000 psi, 30 % of the bulk fluid molecules in the large pores are recovered. Voidage created in the large pores due to the recovery of the hydrocarbon molecules is immediately filled up by the expansion of the 70 % fluid molecules left behind in the large pores. Fluid expansion is an effective recovery mechanism and yields to up to 75 % recovery in the large pores when the pressure is reduced to 1,000 psi. However, the recovery curve for Mixture 1 shows relatively less recovery from the smaller pores. The decrease in recovery with the pore size is a monotonous decline, which indicates that the fluid expansion becomes less effective as a recovery mechanism, as the pore size is reduced. The release of molecules from the small pores to the micro-crack is increasingly controlled by the molecular forces imposed by the pore walls. Hence, in these pores the dominant recovery mechanism is desorption. 32-71 % recovery is observed, mainly due to desorption, from the pores with sizes less than 10 nm, when pressure is reduced to 1,000 psi.

The recovery behavior of Mixture 3 in Figure 3.11 is significantly different, however. Firstly, two separate regions are observed in the pore size distribution: a high recovery region which is associated with the pores that have size 40 nm or higher; and a distinctly low recovery region with pores that have sizes equal to 10 nm or less. (A

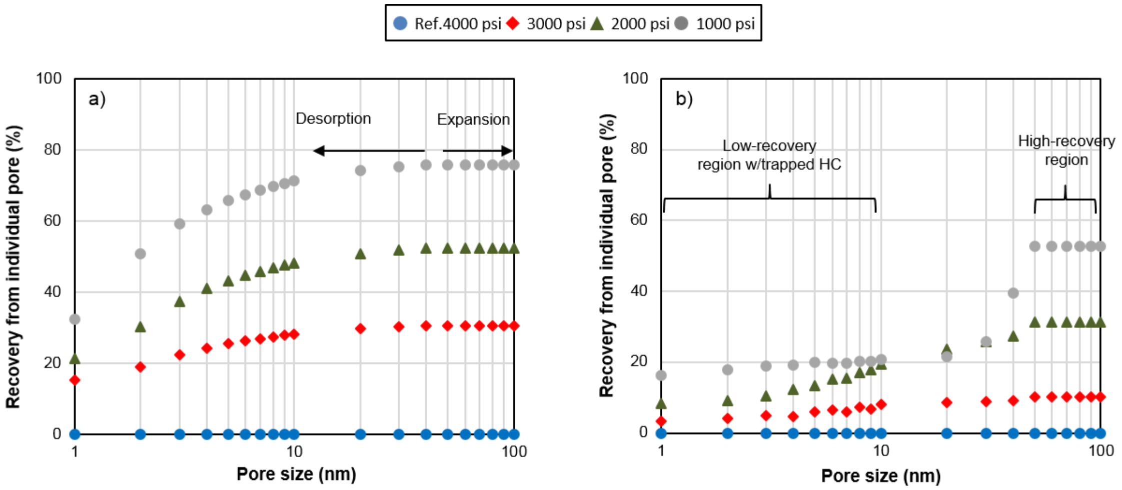

Figure 3.11 Hydrocarbons recovery from individual pores at various pressure and 176 °F.

transition region of rapid change in recovery exists in between the two regions, which will be ignored) In the high recovery region, the hydrocarbons recovery is independent of the pore size, indicating that the recovery of bulk fluids is experienced in these large pores. Compared to Mixture 1, in this region the recovery is much less for Mixture 3 and this is due to the composition effect on the bulk fluid expansion.

The behavior of the fluid in the low recovery region requires a careful discussion. The fluid molecules under confinement cannot expand effectively because the fluids are capillary-condensed. The liquid is not a compressible fluid such as gas; the liquid in nanopores is expected to be even less compressible under the influence of the nanopore walls. In this region the recovery mechanism is desorption of the fluid molecules. Desorption is not an effective recovery mechanism for the capillary-condensed fluids since only a small fraction of the fluid consisting of the lighter components can be released. Consequently, the recovery values observed are low and typically less than 20

% in this region. In Figure 3.11b, clearly all the pores with sizes 10 nm and less have 80 % trapped hydrocarbons when the pressure is reduced to 1,000 psi. Note that in these pores the trapped hydrocarbon amount is not 100 %. This is due to desorption. Although hydrocarbon molecules may not be transported as a bulk fluid, the lighter molecules could be released from the pores.

According to Figure 3.11 the trapped hydrocarbon cut-off is identified as 10 nm. It is worth mentioning that the observed trapping of the hydrocarbons in the low recovery region is different than the physical isolation of the hydrocarbons due to lack of pathways. During the generation of hydrocarbons in the source rock, the fluid in kerogen may not find a crack or channel or some interconnected pore network and, hence, it is physically trapped. Here, in our case the fluid residing in kerogen is in hydraulic communication with the outside through the micro-crack. Hence, it is important to differentiate that the trapping we observe is not due to physical isolation but due to amplified fluid-wall interactions when the multi-component fluid becomes heavier and capillary-condensed.

In summary, depending on the type of the produced fluid mixture and the pore size distribution, significant differences may exist in thermodynamic recovery. For Mixture 1, the cumulative recovery values from Sample 1 including the contribution of all the pores are 24 %, 41 % and 62 %, when the pressure is depleted to 3,000 psi, 2,000 psi and 1,000 psi, respectively. In the case of Mixture 3, the cumulative recovery is much lower due to the nanopore effects. Only 23 % of hydrocarbons can be produced from Sample 1 as the pressure is reduced to 1,000 psi. In order to see the impact of nano-confinement effects on the recovery clearly, the recoveries with and without the nanopore effects are compared

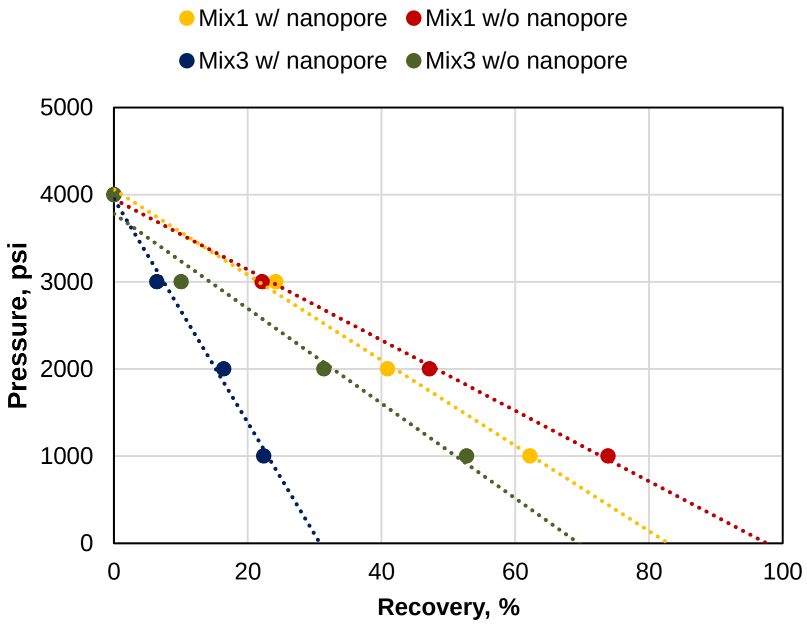

Figure 3.12 Nanopore confinement effects on hydrocarbon mixture recovery from Sample 1.

Table 3.5 Initial hydrocarbon in-place estimated at 4,000 psi 176 °F considering trapped hydrocarbons in nanopores for Mixture 3.

Sample	$d_{p,T}$ nm	ε_T %	G^* scf/ton	***Error*** %
1	10	80.6	22.5	80.3
2	10	24.4	86.4	24.2

in Figure 3.12. Firstly, regardless of nanopore effects, Mixture 3 (wet gas) shows less recovery than Mixture 1 (dry gas), which are shown in red and green lines, respectively.

The difference in recovery of the two mixtures becomes more pronounced as pressure drops further. When the nanopore effects are considered, the recovery is reduced for both mixtures (shown in yellow and navy). The nanopore effects become more pronounced at lower pressure.

The volumetric calculations for hydrocarbon in-place shown in Table 3.4 do not include the trapped hydrocarbons so that the confinement effects can be identified on the producible fluids. In Table 3.5 the impact of trapped hydrocarbons on the hydrocarbon in-place estimation is shown. Clearly, more than 80 % of the Sample 1 effective pore volume are filled with capillary-condensed trapped hydrocarbons that belong to Mixture 3. Note that the presented hydrocarbon in-place and recovery calculations are based on thermodynamic equilibrium molecular simulations which includes isothermal expansion and desorption of the hydrocarbon molecules. The recovery of the fluids at the reservoir scale will be further influenced by the resistances of the geological flow paths, including pore geometry, pore network connectivity and tortuosity (Akkutlu and Fathi 2012; Feng and Akkutlu 2015). Depending on the recombined produced fluid composition, trapped and mobile hydrocarbon volumes in the formation could vary significantly.

3.4. Conclusions

Any production consideration from source rocks should include a discussion on the compositional nature of in-situ hydrocarbon fluids and its connection to the rock matrix. This connection becomes crucial in the presence of organic nanopores in high organic content rocks. Using model organic nanopores in equilibrium with a micro-crack holding bulk hydrocarbon fluid under typical reservoir conditions as the system under investigation, this article demonstrates that the fluid composition varies in organic nanopores as a function of the pore size, when the produced fluid composition is re-distributed into the nanopores. We proposed a new compositional equation of state for the in-situ fluids including the nanopore confinement effects and showed that the hydrocarbon mixture density can be predicted in terms of the density of methane, the main constituent of the reservoir fluids such as dry gas, wet gas, and condensate. The composition effect of hydrocarbon mixtures then appears as a non-linear (logarithmic) deviation from the pure methane behavior under confinement. The error in using the proposed compositional equation of state is less than 5 % at high initial reservoir pressure but grows significantly during the pressure depletion and production. The latter indicates that the pore size dependence of composition and the impact of the nano-confinement change during production. We studied the nature of the fluid and its distribution in the matrix under the initial reservoir conditions but the evolution of the nano-confinement during production is not understood. Further research is needed to develop correlations to predict the effect of nano-confinement on the fluid composition during the depletion. Forecasting of production including the nano-confinement effects can be done computationally only by measuring the produced fluid composition periodically and repeating the re-distribution calculations using the methodology presented in this work. The production related field studies can also shed light into this fundamental issue.

Fluid mixtures in nanopores are heavier, i.e., they maintain larger apparent molecular weight. This is a consequence of the confinement effects occurring in small nanopores with sizes less than 10 nm. (The effects persist up to 40 nm but they are not significant.)

The most significant impact of this observation is that the fluid under confinement experiences modified physical properties. The fluid density and viscosity increase, the estimated mean free path length and transport coefficient decrease. The fluid sustains high density during pressure depletion indicating that vaporization of the capillary condensed fluids is not likely to occur in nanopores, when we consider typical pressure profile observed in the reservoir near the hydraulic fractures.

The recovery of fluids in large pores are due to fluid expansion. But the thermodynamic recovery calculations in this article show that nano-confinement does not allow efficient expansion of the fluids and recovery becomes a slave of the hydrocarbon molecules desorption, i.e., the release of the lighter portion of the mixture from the walls during pressure depletion. Unfortunately, fluid desorption in nanopores is not as efficient a mechanism as expansion in large pores. Consequently, the fluids under significant nano-confinement effects can be practically considered trapped. Furthermore, because desorption is controlled by the molecular interaction forces between the wall and fluid, the chemistry of the wall surfaces as well as the fluid composition are the primary controls on the recovery, not the mobility of fluid. Dilution of the mixture in the pores using a solvent such as ethane, liquefied petroleum gas, or CO_2 could potentially improve the recovery from these pores.

4. CO_2-STRIPPING OF KEROGEN CONDENSATES IN SOURCE ROCKS[2]

Much work has been done targeting hydrocarbon fluids in organic materials of source rocks such as kerogen and bitumen. These studies were, however, limited in scope to simple fluids confined in nanopores and ignored multi-component effects. Recent studies using hydrocarbon mixtures revealed that compositional variation caused by selective adsorption and nano-confinement significantly alters phase equilibrium properties of the fluids. One important consequence of this behavior is capillary condensation and trapping of hydrocarbons in organic nanopores. Pressure depletion produces lighter components, which make up a small fraction of the in-situ fluid. An equilibrium molecular simulation of hydrocarbon mixtures is carried out to show the impact of CO_2 injection on the hydrocarbon recovery from organic nanopores. CO_2 molecules introduced into the nanopore lead to exchange of molecules and a shift in the phase equilibrium properties of the confined fluid. This exchange has a stripping effect and in turn enhances the hydrocarbon recovery. The CO_2 injection, however, is not effective for heavy hydrocarbons as much as for light components in the mixture. Those large molecules left behind after CO_2 injection mainly make up the residual (trapped) hydrocarbon amount. High injection pressure leads to significant increase in recovery from the organic nanopores but not critical for the recovery of the bulk fluid in large pores.

---

[2] This chapter is from SPE-190821-PA "CO_2-Stripping of Kerogen Condensates in Source Rocks" written by Seunghwan Baek and I. Yucel Akkutlu. It is reprinted here with permission of SPE J., whose permission is required for further use.

Diffusion of CO_2 into nanopores and the exchange of the molecules are the primary drives that promote the recovery, whereas pressure depletion is not effective on the recovery. The results for N_2 are also presented for comparison.

4.1. Preliminaries

Resource shale and other source rock formations such as mudstone, siltstone and carbonates have significant amounts of organic material which makes up a complex multi-scale pore structure that not only consists of fractures and micro-cracks but also nanometer-size organic pores (Loucks et al. 2012). In particular, as a solid insoluble organic material, kerogen has received much interest in the literature due to its contribution to the storage of hydrocarbons (Javadpour et al. 2007; Kang et al. 2011; Ambrose et al. 2012; Bousige et al. 2016). The amount of organic matter is directly correlated to the amount of hydrocarbons stored in-place. However, large uncertainties exist during the assessment of resource shales due to added complexities associated with chemical and physical properties of the organic matter such as solid chemistry, maturity, pore size distribution, porosity, tortuousity, and moisture content (Weniger et al. 2010; Loucks et al. 2012; Gasparik et al. 2012; Zhang et al. 2012).

One important feature of kerogen in source rocks is that the pore scale within kerogen spans from a few angstroms to hundreds of nanometer range (Ambrose et al. 2012; Clarkson et al. 2013). The low end of the pore size distribution is regarded as responsible for the ultra-low permeability of source rocks. At this scale, conventional Darcy’s law breaks down and molecular diffusion plays a critical role in mass transfer, which is influenced by the adsorption of the fluid hydrocarbons (Javadpour et al. 2007;

Bousige et al. 2016; Olorode et al. 2017a). Strong fluid-solid interactions inside the kerogen pore network makes the understanding of the fluid storage and transport quite challenging. This is especially the case when multi-component fluids are involved.

The hydrocarbon fluids in organic nanopores can have significantly varying composition. (Stevenson et al. 1991; Arri et al. 1992; Clarkson and Bustin 2000; Hartman et al. 2011). Recently, Bui and Akkutlu (2017) used thermodynamic equilibrium computations and predicted in-situ fluid composition and properties in kerogen nanopores using the composition of the produced fluids. Their composition re-distribution approach showed that nano-scale pore confinement effects lead to significant variations in the composition of the fluid inside the nanopores compared to that of the produced bulk fluid.

Baek and Akkutlu (2019a) recently expanded the re-distribution computations to different produced fluids, and their observation was in agreement with literature (Jiang et al. 2005; Pitakbunkate et al. 2017; Wu et al. 2017). They argued that the composition effect becomes more pronounced during the production and pressure depletion. Baek and Akkutlu (2019a) showed the impacts of the compositional variation in kerogen on initial gas in-place estimation and pressure depletion production in shale gas reservoirs. Clearly, the nanopore does not hold the initial composition during depletion. Note significant increase observed in relative concentration of n-butane and n-pentane during the depletion. There is an increase in the absolute number of the heavy components under the influence of pressure drop while the light components are released from the pore. This release is mainly controlled by the molecular forces acting on the fluid in nanopore, and by the

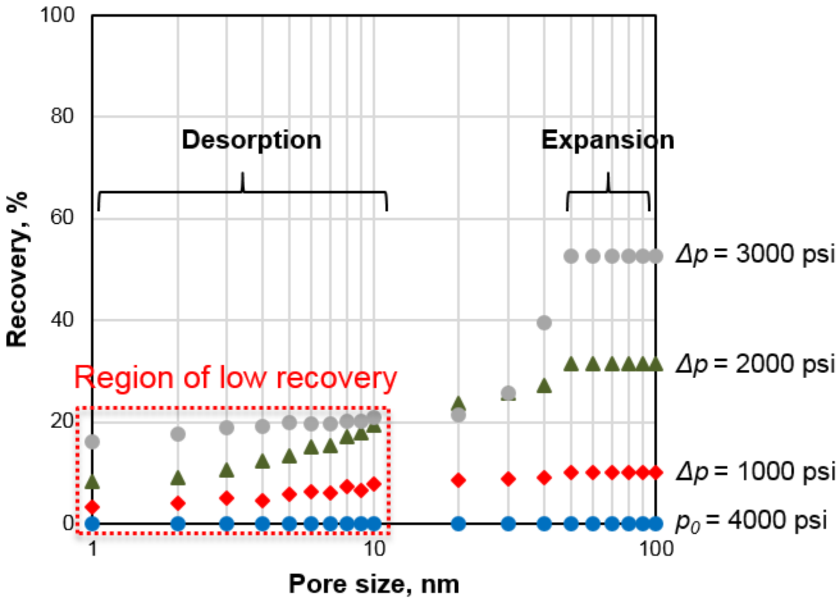

Figure 4.1 Hydrocarbon recovery from model kerogen nanopores during pressure depletion from 4,000 psi at 176 °F.

energy difference between the nanopore and the nearby micro-crack holding the bulk phase fluid.

Figure 4.1 shows the computed percent recovery from the individual nanopores during the depletion. The recovery experiences a 40 nm cut-off pore size above which the release of hydrocarbons is mainly due to gas expansion. For those pores above 40 nm, the expansion of the gas leads to recovery up to 50 % during the depletion. This is similar behavior in recovery of the natural gases from conventional resources. Below 40 nm, however, the recovery is controlled by desorption of the fluid molecules from the nanopores. In these pores, fluid desorption is not as effective a recovery mechanism as the

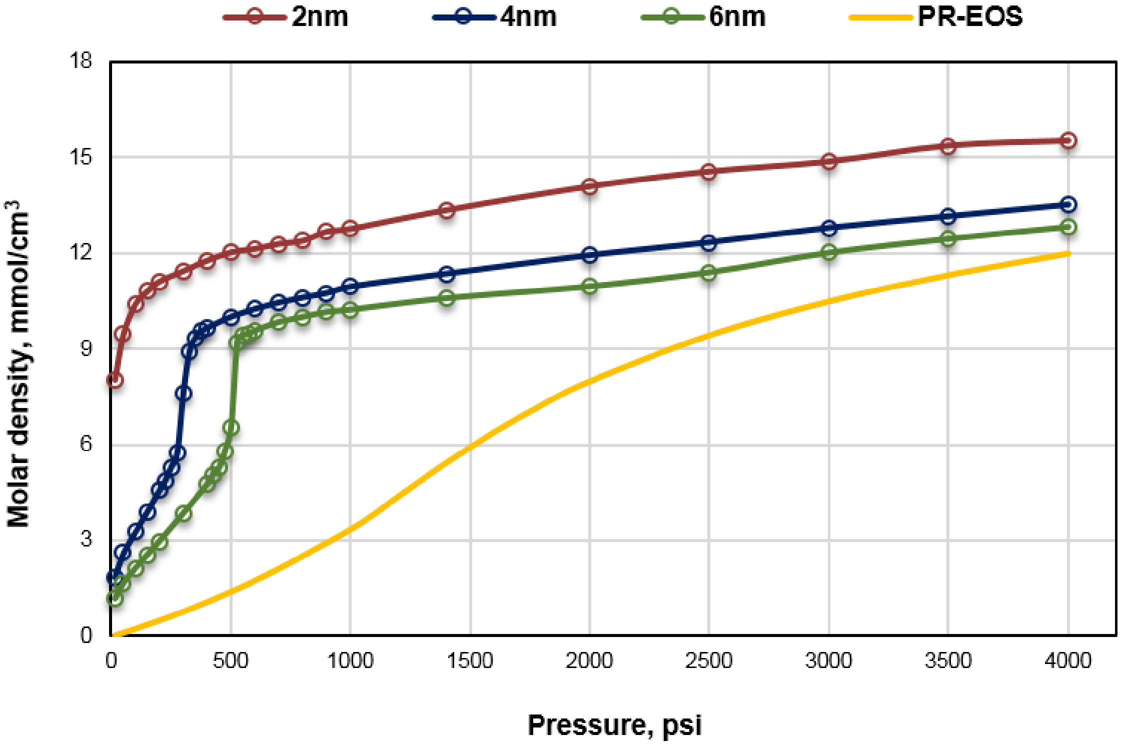

Figure 4.2 Molar density isotherm of the hydrocarbon fluid mixture in nanopores at 176 °F.

fluid expansion, however. Consequently, with the decrease in pore size from 40 nm to 20 nm, a sharp drop is observed in recovery. The recovery further decreases as the pore size is reduced below 10 nm. For this hydrocarbon mixture and several other produced fluid compositions, the recovery of the redistributed hydrocarbons from kerogen nanopores is typically below 20 %.

In order to gain physical insight into this peculiar behavior in recovery from kerogen nanopores, Figure 4.2 shows the density-pressure diagram of the in-situ hydrocarbon mixture in nanopores at a constant temperature. Each isotherm shows the average (molar) density change of a confined fluid in a particular nanopore. The results are compared to the bulk fluid behavior in the micro-crack, which was predicted using Peng-Robinson equation of state (Peng and Robinson 1976). In the isotherm, we look for pressure regions where a sharp change in density is recorded, indicating a phase change such as capillary condensation or vaporization of the hydrocarbon mixture (Gelb et al. 1999). Clearly, the bulk fluid does not go through any phase change over the pressure domain investigated, and shows the expansion behavior of the conventional dry gas reservoirs. The nano-confined fluids, on the other hand, show vaporization of the capillary-condensed fluid at 100 psi, 350 psi and 525 psi in 2 nm, 4 nm and 6 nm pore, respectively, during the pressure depletion. In essence, the isotherms show that the low recoveries estimated in Figure 4.1 were low because the fluid mixture was capillary-condensed in the pore, and that the pressure reduction needed to vaporize the in-situ hydrocarbons was much less than the applied pressure. This indicates a limited ability of pressure depletion to recover the confined fluids from organic nanopores.

The computational results on the occurrences of hydrocarbon fluids in kerogen under typical reservoir conditions and during the depletion raise serious questions on the ultimate recoveries from organic-rich source rocks. How can one improve desorption of hydrocarbons from kerogen? The reduction of flowing bottomhole pressure to values less than 500 psi could be impractical in some of the highly over-pressured source rocks. Besides, the depletion of the source rock reservoirs to such low pressure values could take long production times. One approach to the problem could be to inject inexpensive lean gases such as carbon dioxide (CO_2), nitrogen (N_2) or their mixtures (flue gas) into the formation once sufficient depletion near the hydraulic fractures is achieved for injection.

The injected gas molecules will penetrate into the formation and reach into the natural fractures and micro-cracks, where molecular-level interactions with the residual hydrocarbons will take place. If the injected fluid is not miscible with the residual hydrocarbons, then the injected fluid only plays the role of a displacing fluid under the influence of local capillarity. If, however, the injected fluid is miscible, then it dissolves and diffuses into the residual oil phase.

A large body of literature exists on the impact of miscible gas injection operations on the enhanced oil recovery. It is widely accepted that microscopic displacement efficiency of lean gases is high. Super-critical CO_2, in particular, shows gas-like mass transfer and liquid-like solvating characteristics (Hawthorne 1990) and maintains a dynamic miscibility with the residual oil (Monin et al. 1987; Jarrell et al. 2002). When miscible, CO_2 molecules dissolve and diffuse into the residual hydrocarbon mixture relatively easily. The latter experiences a drastic change in its density (i.e., swelling), and its viscosity decreases when it is diluted with the injected fluid molecules (Monin et al. 1987; Monger et al. 1991). Changes in the thermos-physical properties of the residual hydrocarbon mixture and swelling cause mobilization of the residual oil. So, injection of CO_2 molecules is expected to increase the recovery from these relatively easily accessible fractures and micro-cracks in the source rock. However, the effectiveness of the injected gas molecules is still questionable when they target the confined hydrocarbons within strongly hydrophobic nanoporous organic matter such as kerogen and bitumen.

Based on recent work by Baek and Akkutlu et al. (2019a), using Figures 4.1 and 4.2, so far we have found out that the recovery from kerogen nanopores is mainly due to desorption of the hydrocarbon molecules. Hence, the mobilization of the diluted hydrocarbon-CO_2 mixture in these small pores should be considered in the presence of strong fluid-wall interactions. This is, however, a complex question that has not been addressed yet. At best, one would anticipate that the CO_2 molecules could act as the light components in the mixture. This could help dilute and vaporize the hydrocarbon mixtures in nanopores at an injection pressure much higher than the pressure of vaporization. Let us remind ourselves that CO_2 has unique properties resulting from its intra-molecular quadruple charges, which are not only effective in replacing the hydrocarbon molecules but also impose enhanced storability in nanopores (Nuttall et al. 2005; Kang et al. 2011; Heller and Zoback 2014; Olorode et al. 2017b). Selective adsorption of CO_2 in kerogen pores is weaker than some of those of heavy molecules in the mixture such as butane and pentane while stronger than those of light components. So, understanding the relation between competitive adsorption of hydrocarbons and CO_2 in the organic nanopores could be critical to recovery. To date, the confined multi-component fluids have rarely been explored at the microscopic scale, especially for the application of CO_2 injection into source rocks.

In this work, the stripping effects of CO_2 gas are quantified under typical source rock conditions, and remaining hydrocarbons in the nanostructure are measured. Further, the hydrocarbon fluids produced from the nanoporous kerogen in the presence of injected gas molecules are analyzed and compared with the fluids recovered by the pressure depletion only. This investigation provides a fundamental understanding of the microscopic behavior of the multi-component fluids confined in nano-structures and gives

Table 4.1 Mole fraction and molecular weight of the components used in the bulk phase hydrocarbon fluid.

Mixture	Mole fraction in bulk phase, %						MW, g/mol
	CO_2	CH_4	C_2H_6	C_3H_8	n-C_4H_{10}	n-C_5H_{12}	
1	0.0	53.8	16.4	12.7	10.5	6.6	30.0
2	10.0	48.4	14.8	11.4	9.4	5.9	31.4
3	30.0	37.6	11.4	8.9	7.4	4.7	34.3
4	50.0	26.9	8.1	6.3	5.3	3.4	37.1
5	70.0	16.1	4.9	3.8	3.2	2.0	39.8
6	90.0	5.3	1.6	1.3	1.0	0.7	42.6

new insights into lean gas-assisted recovery of subsurface condensates and oil in source rocks.

4.2. Fluid Model

The initial fluid mixture has the produced fluid composition from the Middle Bakken formation in Williston basin, USA (Mixture 1 in Table 4.1) (Zhang et al. 2013). It has a specific gravity, 1.28. The fluid mixture consists of five hydrocarbon components: methane (CH_4), ethane (C_2H_6), propane (C_3H_8), n-butane (n-C_4H_{10}), and n-pentane (n-C_5H_{12}). The liquid saturation at given temperature is negligible and, hence, this fluid represents a wet gas. Injected CO_2 molecules are added into the bulk phase while the total number of molecules of hydrocarbons in the bulk phase is kept constant. Thus, the mole fraction of each component changes as the injected gas takes up 10 %, 30 %, 50 %, 70 % and 90 % of the total number of molecules in the bulk phase. This study simulates a particular situation when the injected gas molecules diffuse into the bulk phase outside of the nanopores in places such as fractures and micro-cracks. Hence, we consider that the

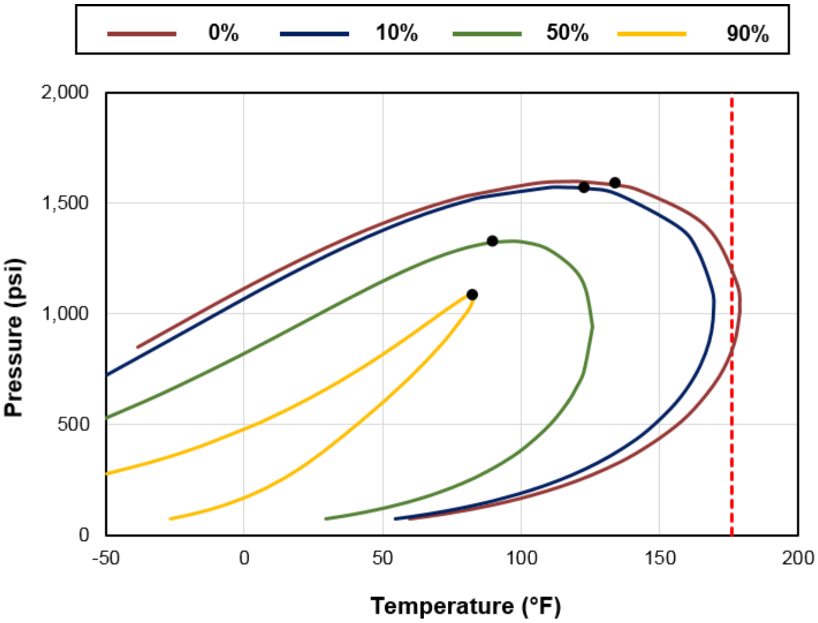

Figure 4.3 Phase diagram of hydrocarbon-CO_2 mixtures.

injected molecules are first-contact miscible with the bulk hydrocarbons for all the conditions considered. For hydrocarbons in nanopores, measurement of minimum miscibility pressure is a challenging task, and the current fluid models cannot capture it accurately because of the compositional variations inside the pores. We, therefore, give a variety of simulation data at a wide range of pressure conditions. The detailed compositions of the fluid mixtures are given in Table 4.1, and their pressure-temperature phase diagrams are shown in Figure 4.3. The specific mole fraction of the injected molecules would be used during the discussion. Note that in the absence of the injection fluid, with pressure depletion, these hydrocarbon mixtures are produced from the nanopores only in limited amounts due to nanopore confinement effects (Baek and Akkutlu 2019a).

4.3. Results and Discussion

Recovery of hydrocarbons from the model kerogen nanopores is measured as a function of the injected CO_2 concentration in the bulk phase in Figure 4.4. The x-axis in Figure 4.4 indicates the mole fraction x of injected CO_2 in the bulk fluid phase. The y-intercept at x =0 % represents the recovery in the absence of CO_2 with pressure depletion only, i.e., the primary recovery factor. The other data points on the plots with CO_2 concentration greater than 0 % indicate the recovery factor predicted in the presence of both the pressure depletion and the injected fluid concentration effects. For example, at 2,500 psi, firstly the pressure is depleted from 4,000 psi to 2,500 psi as an indication of the primary recovery, and then CO_2 at various concentration values is introduced into the bulk phase in the micro-crack at 2,500 psi. Interpolation could be used for a pressure different than the values shown. Figure 4.4 includes extrapolated values to predict the ultimate recovery and measure the non-recoverable hydrocarbon amount when the bulk fluid is fully filled up with the injection gas (i.e., x =100 %), which is the case corresponding to an infinite number of pore volumes of the injected fluid. The increment beyond 90 % of CO_2 mole fraction increases the molecular simulation cost significantly. We use both linear and a quadratic extrapolation. Both types of fitting give fairly reasonable accuracy. For clarity, only the fitting lines of a quadratic equation are included in Figure 4.4. Note that the model kerogen nanopores still hold hydrocarbon molecules when the injected CO_2 concentration in the bulk phase is extrapolated to 100 %. In this study, the residual hydrocarbon (R_{HC}) is defined as the ratio of the amount of hydrocarbons

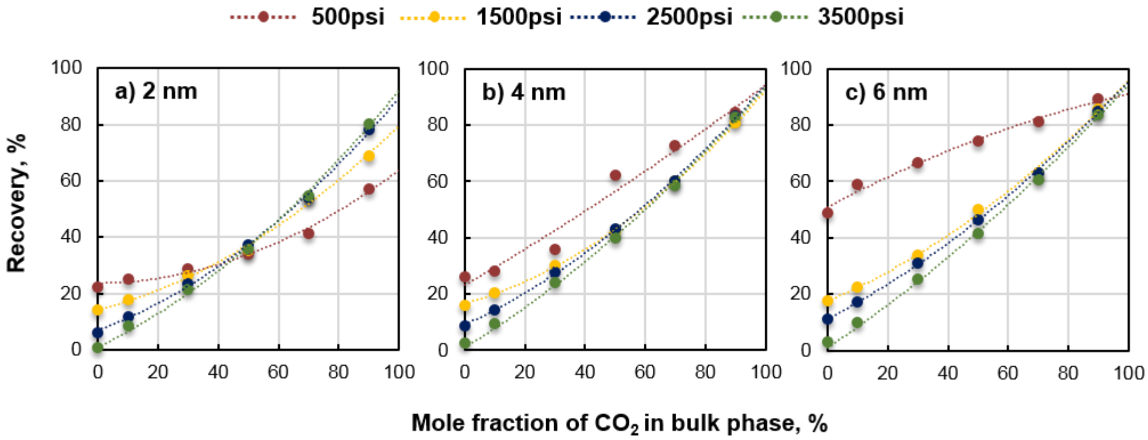

Figure 4.4 Enhanced recovery with CO_2 injection.

remained in the nanopore following the enhanced recovery using 100 % CO_2 to the amount of hydrocarbons stored in the pore at the initial reservoir conditions.

The primary recovery in the absence of injection gas, i.e., the data points on the y-axis, is less than 20 % for a reservoir pressure value as low as 1,500 psi for all the pores analyzed. It indicates an optimistic thermodynamic recovery value, because infinite time is considered to reach equilibrium state, hence the resistances associated with the fluid transport do not influence the recovery. When the pressure drops to 500 psi, a jump to 50 % recovery is observed in 6 nm pore due to the vaporization of the hydrocarbons in the pore. Indeed, the impact of vaporization on the recovery is large because desorption of gas molecules are easier than the liquid molecules. In 2 nm and 4 nm pores, however, the recovery does not exceed 25 % at the same pressure because the depletion is not large enough to vaporize the fluids in these smaller pores. This indicates that the primary production stage is not effective in recovering hydrocarbons from pores with sizes less than 4 nm where fluids are capillary condensed and fluid molecules release are controlled by the nanopore walls.

The injection of CO_2 into the system improves the recovery from all the pores investigated. The improvement in recovery is closely correlated to the amount of CO_2 molecules. As more CO_2 is introduced into the bulk fluid, it is more likely for the CO_2 molecules to diffuse into the nanopores and extract more of the hydrocarbon molecules in nanopores. This indicates the importance of molecular diffusion as the mechanism that allows penetration of the injected gases from the fractures and micro-cracks into the small kerogen pores. In the case of CO_2 at 500 psi, the changes in pore size result in significant differences in recovery. In particular, for 6 nm pore, the low recovery efficiency indicated by a smaller slope is caused by the high primary recovery with pressure depletion (large value on the y-intercept). The fluid in 6 nm pore goes through vaporization at 525 psi (Figure 4.3), and the phase change leads to a sudden increase in recovery. Consequently, this high primary recovery leaves only a small margin for further enhancement by CO_2 injection.

Furthermore, lower injection pressure (or larger pressure depletion) normally brings out higher recovery in 4 nm and 6 nm, and the difference in recovery becomes smaller as the mole fraction of CO_2 in the bulk phase is increased. Finally, the different injection pressure values reach almost the same recovery at 100 % CO_2. Thus, in the case when there is no phase change due to pressure depletion, the impact of injection pressure on the hydrocarbon recovery becomes negligible for 4 nm and 6 nm pores, as the bulk phase is filled up with the injection fluid. The average recovery (standard deviation) at

Table 4.2 Recovery enhancement comparison for CO_2 injection.

Pressure psi	2 nm pore			4 nm pore			6 nm pore		
	RF^1, %	RF^2, %	η	RF^1, %	RF^2, %	η	RF^1, %	RF^2, %	η
500	22.5	63.3	2.8	26.0	95.3	3.7	48.9	90.1	1.8
1,500	14.0	79.3	5.7	16.0	92.4	5.8	17.5	95.9	5.5
2,500	6.2	88.6	14.3	8.7	94.6	10.9	11.1	95.3	8.6
3,500	1.0	91.8	91.8	2.7	94.2	34.9	2.9	95.5	32.9

100 % is 94.1 % (1.24) for 4 nm and 94.3 % (2.52) for 6 nm, respectively. (The details are included in Table 4.2) This observation, however, is not valid when the pore size is reduced to 2 nm. For 2 nm pore, significantly different recovery is observed when the pressure is varied. When the mole fraction of CO_2 in the bulk phase fluid is low, the pressure depletion gives relatively high recovery. However, as the CO_2 occupies more than half of the bulk phase (x > 50 %), the higher injection pressure produces more hydrocarbons from the 2 nm pore. This indicates that the CO_2 injection at high pressure (small pressure depletion) can retrieve more hydrocarbons from 2 nm pore than that produced with large pressure depletion. The reason for this unique trend to those of the mesopores at 4 nm and 6 nm comes from both the compositional variance in nanopores and varying stripping ability of CO_2 over individual components. Previous studies revealed that as the pressure is reduced, 2 nm pore is preferentially filled up with more of heavy components such as n-butane and n-pentane, which are relatively more difficult to be extracted by CO_2. The recovery is limited even when large pressure drop is applied. At

higher pressure, mostly light components such as methane and ethane reside in 2 nm pore of the organic matter due to size entropic effect (Lu et al. 2003; Jiang et al. 2005; Bui and Akkutlu 2017; Wu et al. 2017), and they are producible by the introduced CO_2. That leads to higher recovery than that with the pressure depletion. Therefore, CO_2 injection can achieve higher recovery at high pressure (with small pressure depletion) when there are relatively more of the light components. Note that the enhanced recovery at high pressure is not caused by the solvating characteristics of supercritical CO_2 but by difference in a level of adsorption/desorption among components originating from the results of the energy balance in nanopores.

The predicted enhanced recovery of the condensate resulting purely from the gas injection process is given in Table 3.3. Here, RF^1 corresponds to the recovery factor driven by pressure depletion only at x = 0 % in Figure 4.4. RF^2 includes the recovery from both pressure depletion and gas injection at x = 100 % in Figure 4.4 and is obtained from extrapolation to 100 % injected gas using the quadratic line. The recovery enhancement (η) is calculated as RF^2/RF^1 ratio and indicates the improvement in recovery purely due to gas injection. The table shows that high-pressure injection significantly enhances recovery, and this observation is regardless of the pore size.

R_{HC} indicates remaining (or trapped) hydrocarbons at x =100 %, when the injection gas entirely fills up the bulk phase fluid as mentioned above. This case is difficult to replicate in the field because of the ultra-low permeability of the source rocks. Molar density in a particular pore at 4,000 psi is used as the reference to calculate R_{HC}. The value is calculated from the ultimate recovery in Figure 4.4 using the following expression:

$$R_{HC} = 1 - \frac{\text{Ultimate Recovery}(P, D_p)}{100}. \tag{4.2}$$

The ultimate recovery using 100 % gas injection is estimated using the extrapolated value of the quadratic equation in Figure 4.4. The calculated R_{HC} values are shown in Figure 4.5. Firstly, distinct difference exists on the estimated residual amounts. R_{HC} in 2 nm pore is strongly pressure-dependent, and higher CO_2 injecting pressure leaves less hydrocarbon molecules behind. According to the results, injecting supercritical CO_2 at high pressure can be preferred in order to maximize the ultimate recovery from the 2 nm pore. For 4 nm and 6 nm pores, CO_2 injection is somewhat insensitive to the injecting pressure and R_{HC} remains below 10 % over the range of pressure. Especially, when CO_2 is injected at 3,500 psi, similar R_{HC} is obtained from all investigated pores.

The stripping effect of the injected CO_2 molecules is studied using the molar density profile inside the nanopores. The density distribution at 1,500 psi is plotted for 4 nm pore at various bulk mole fractions of CO_2 (0, 10, 50 and 90 %) in Figure 4.6. The pore size is defined by taking the center of mass (COM) of the carbon atoms on the pore walls as reference. Also, the density profile calculation counts the location of COM of hydrocarbon molecules. Hydrocarbon molecules cannot access right next to COM of the carbon wall due to repulsive forces. Then, the effective pore size can be smaller than the defined pore size. We used 0.1 Å wide bins to construct the continuous density profiles across the half-length of the pore. The density at the center of the pores is omitted. The results for hydrocarbons are provided only for methane and n-pentane. Ethane and propane show similar behavior to that of CH_4 while n-butane shows behavior similar to n-pentane.

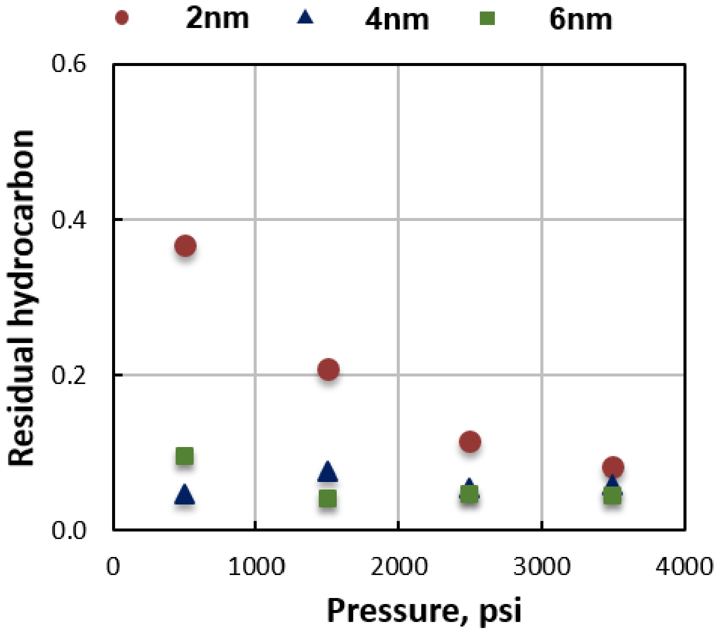

Figure 4.5 Residual hydrocarbon (R_{HC}) in nanopores.

Firstly, 10 % CO_2 is not sufficient to strip off the hydrocarbon molecules from nanopore, but once the concentration of the introduced CO_2 has reached 50 %, CO_2 molecules form the adsorption layer and replace the hydrocarbons in the pores. Although methane has relatively weaker affinity to the wall compared to CO_2, as part of their effort to reach equilibrium, they fill in small gaps among large hydrocarbons and CO_2 molecules. Since the COM is used for molar density profile calculation, the molar density profile of the n-pentane starts further away from the wall compared to that of methane. This also leads to a formation of the wide adsorption layer compared to those of the pure component system. An investigation on angular orientation in the adsorption layer (not shown) shows that molecules are oriented having angles between 25°- 40° against the pore surface (x-y plane) irrespective of the species. This supports the existence of a wider adsorption layer. At 90

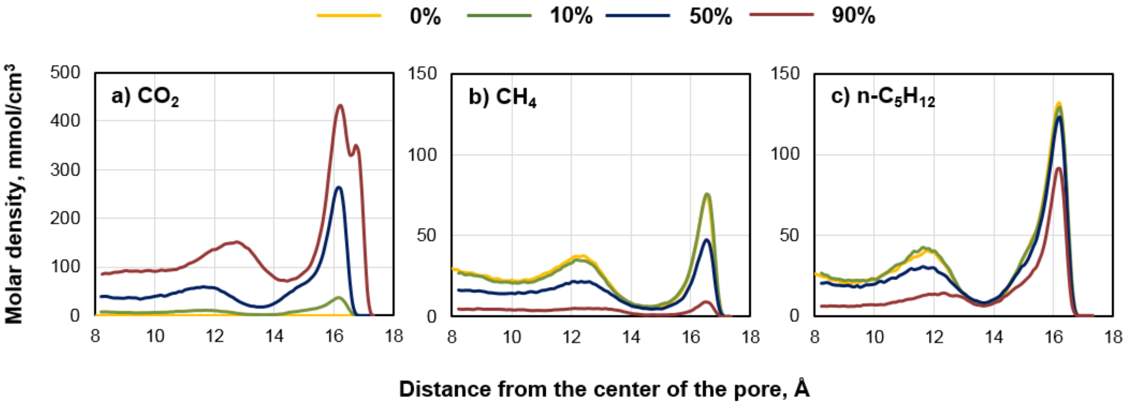

Figure 4.6 Molar density profiles in 4 nm pore at 1,500 psi with various bulk phase mole fraction of CO_2.

% CO_2, when many of the hydrocarbons are exchanged with CO_2 molecules, CO_2 fills up the space right next to the wall where the hydrocarbons used to occupy. The remaining heavy hydrocarbon molecules, however, prevent the smooth first adsorption layer of CO_2 from being formed. This leads to the formation of an unusual tip-splitting in the first adsorption layer for CO_2. This tip-splitting is not observed in the system having light hydrocarbons only. This will be discussed further below. In Figures 4.6b and 8c, hydrocarbon molecules are exchanged by the CO_2 molecules over the entire pore space. When 90 % of the bulk phase is filled with CO_2, only a miniscule amount of methane is left while many n-C_5H_{12} molecules still remain in the pore, especially in the adsorption layer. The stronger affinity of the heavy component to the pore surface does not enable CO_2 to strip these molecules. These trapped hydrocarbon molecules in the adsorption layer are responsible for the aforementioned residual hydrocarbons (R_{HC}).

Next, the pressure effects on R_{HC} are analyzed in Figure 4.7. The figure contains the molar density profile of each component in 2 nm and 6 nm pores when the bulk mole

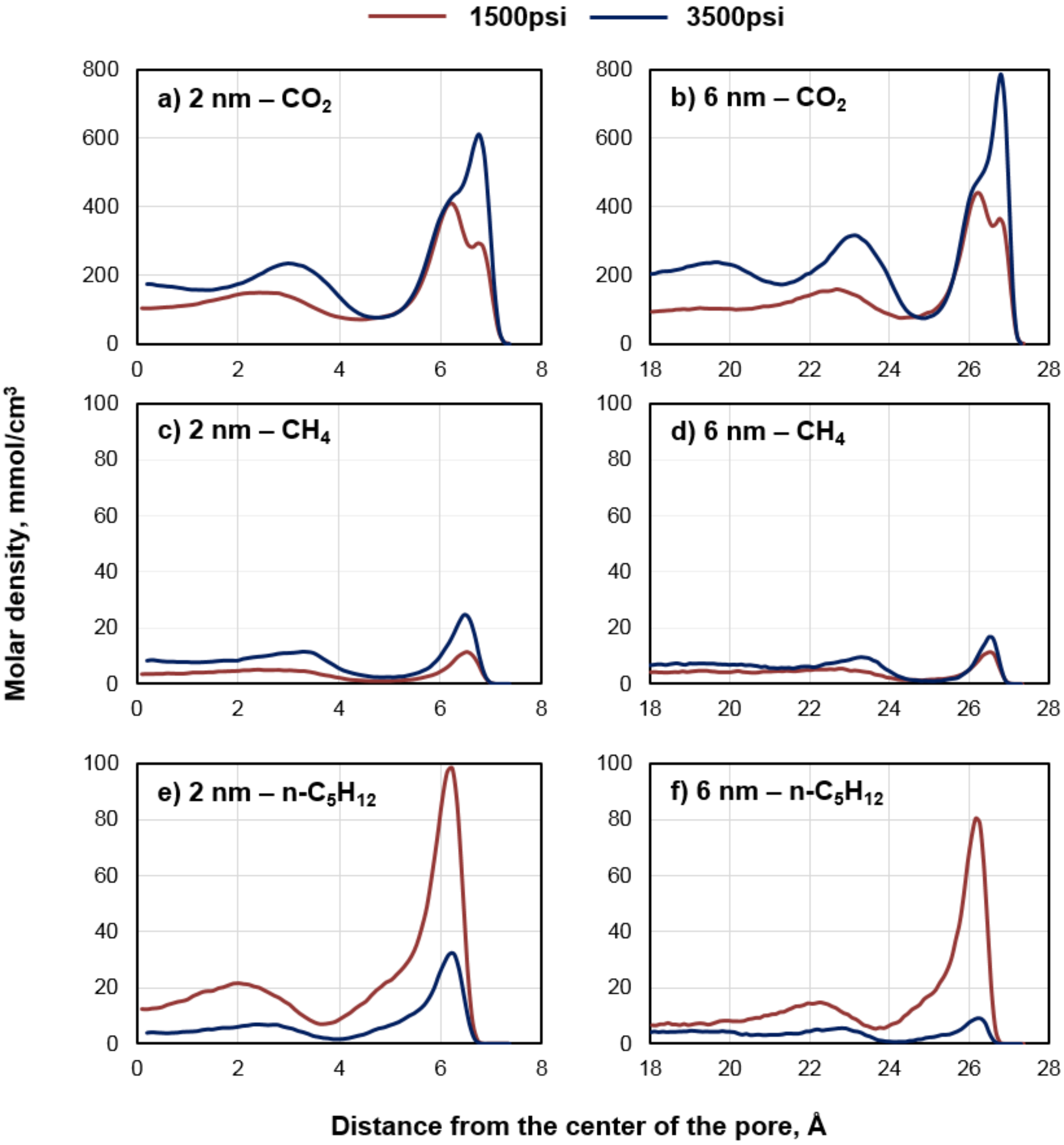

Figure 4.7 Molar density profile in nanopores with 90 % bulk mole fraction of CO_2 at 1,500 psi and 3,500 psi.

fraction of CO_2 is 90 % at 1,500 and 3,500 psi. In Figure 4.7a, we note that as the pressure is increased, CO_2 fills up the entire pore space and displaces more of hydrocarbons, especially the region right next to the wall. Clearly, the tip-splitting in the density stems from the presence of the large hydrocarbon components in the mixture considering the density change of methane is negligible with the pressure change. For methane, the pore size and pressure have no significant impact on R_{HC} because recoverable methane is already displaced with the injected CO_2. For n-pentane, in contrast, R_{HC} is reduced as the pore size or pressure increases. In general, the molar density in the adsorption layer increases with decreasing pore size due to nano-confinement. This was observed previously by Liu and Wilcox (2012). However, in Figures 4.7a and 9b, the CO_2 density at 6 nm is higher than that at 2 nm. This is attributed to the remaining n-pentane. Due to the steric effect of the heavy and large components, relatively small change in the density of pentane causes a large increase in the density of CO_2.

In this study, CO_2 injection is introduced because hydrocarbon fluids go through condensation within the nanopores of interest, and the nanopore allows only a small recovery of the condensed fluid. Now, we investigate how the injected CO_2 affects the density-pressure phase diagrams. Molar density isotherms with different levels of CO_2 injection at 176 °F are provided for 4 nm pore in Figure 4.8. These isotherms are often used to determine the stored gas capacity and the phase change. Figure 4.8a indicates the total molar density isotherm taking into account all the molecules in nanopores, including the in-situ hydrocarbons and the penetrating CO_2 molecules. Figure 4.8b considers only the hydrocarbon molecules.

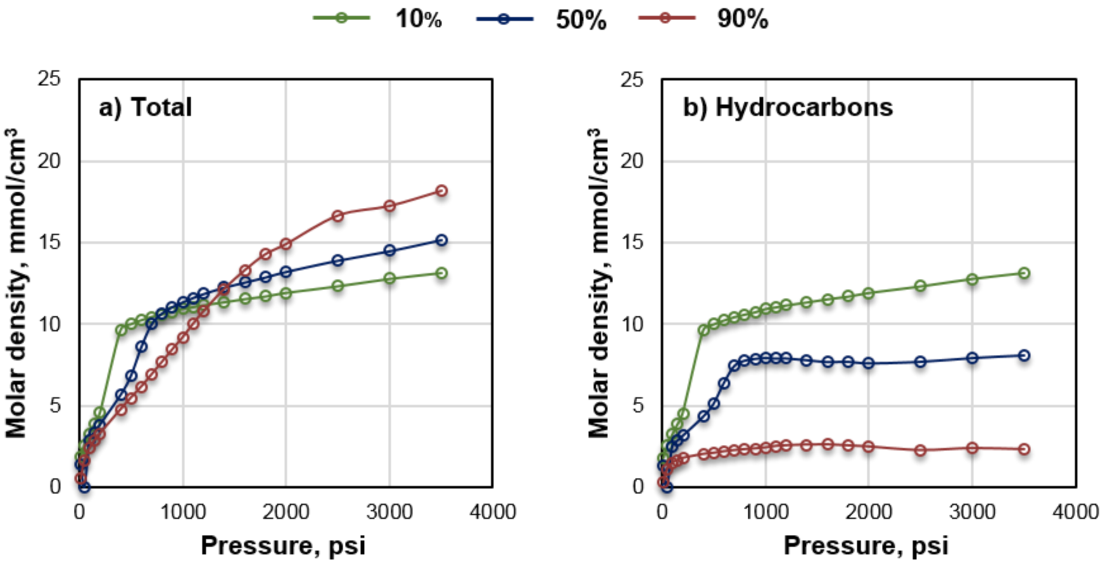

Figure 4.8 Molar density isotherm in 4 nm pore at 176 °F.

In Figure 4.8a, the pressure where the slope of the isotherms drastically changes as an indication of vaporization is shifted to a higher pressure with increasing CO_2 fraction. Specifically, the drastic slope change is observed at 400 psi and 800 psi at 10 % and 50 % CO_2, respectively. And finally, the discontinuity in slope disappears when the bulk mole fraction of CO_2 reaches 90%, and the total molar density isotherms become smoother for all the pore sizes. These trends indicate shifts in vaporization pressure due to the presence of CO_2 molecules in the pore. The smooth isotherms indicate the exchange of molecules between the bulk phase and the nanopore more sensitive to pressure changes. In addition, as 90% CO_2 is introduced, the nanopore holds more of molecules inside the pore at higher pressure. For instance, at 3,500 psi and 90 % CO_2, 4 nm pore shows 38.1 % increase in total molar density with respect to that of no CO_2 case. This is because the relatively middle size CO_2 displaces larger molecules such as n-butane and n-pentane and thus, denser packing of molecules is possible. The quadruple charges of CO_2 also contribute to this, and 15 % less molar density is observed without considering the intra-molecular electrostatic forces.

Next, the molar density of hydrocarbons in Figure 4.8b is obtained by subtracting the CO_2 portion from the total molar density. This isotherm shows the sensitivity of the hydrocarbon release on the pressure change. Injected CO_2 leads to development of a broad range of pressure for the stabilized density after the shifted pressure conditions where the sharp changes in slope occur. This stabilized value in the isotherms indicates that the pressure depletion has no thermodynamic impact on the hydrocarbon recovery during CO_2 injection at normal reservoir pressure above 1,000 psi. For instance, as CO_2 is introduced at 3,500 psi, the molar density of hydrocarbons in Figure 4.8b decreases, and the difference in density between Figure 4.8a and 4.8b increases indicating that injected CO_2 displaces hydrocarbons in the nanopore. Then, as pressure is decreased at 90 % CO_2 (Figure 4.8b), the consistent molar density is observed and continues until it meets the drastic change at low pressure. Note that during cyclic CO_2 injection, pressure depletion and production are processed after CO_2 injection. The results imply that CO_2 molecules introduced into the nanopores during soaking periods significantly increase the hydrocarbon production from the nanopore. Also, it can be inferred that only the injected CO_2 molecules, not the hydrocarbons, are released from the pore during the pressure depletion process following the soaking. This is observed in other sizes of pores as well.

The specific gravity of the fluids produced from the 4 nm pore is analyzed in Figure 4.9. The producible hydrocarbon amounts in the source rocks were quantified using the

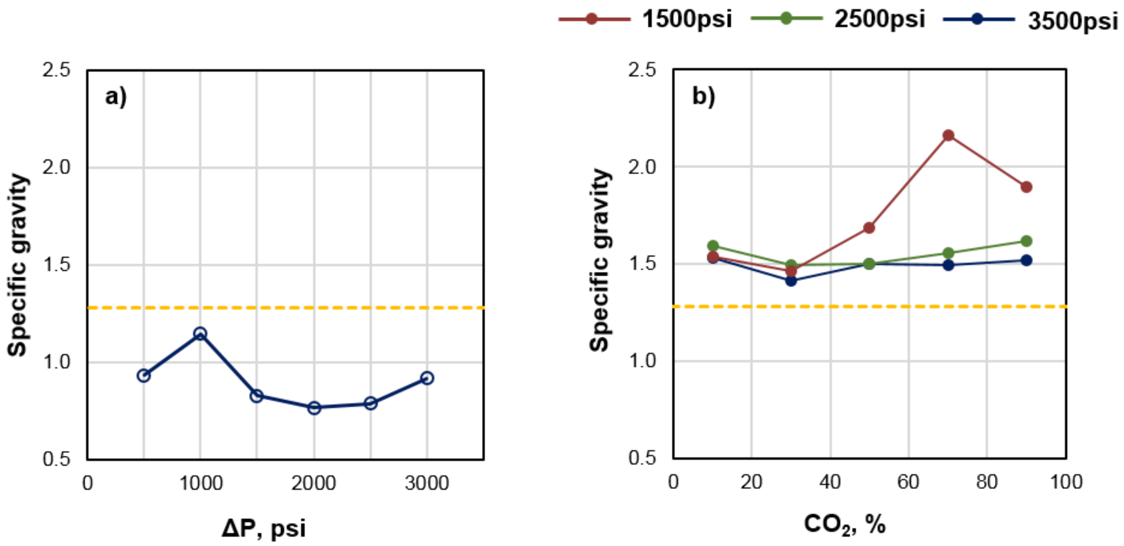

Figure 4.9 Specific gravity of the produced fluids from 4 nm pore.

specific shale sample data in our previous work (Akkutlu et al. 2017). Here, we only concentrate on the qualitative aspect of the produced fluids. Figure 4.9a shows the specific gravity of the fluids produced by pressure depletion only. X-axis indicates the pressure depletion from 4,000 psi. The dash guideline indicates the specific gravity (1.27) of the mixture with no CO_2. The result shows that the pressure depletion produces the lighter fluids from the nanopore. Once the pressure is reduced by 1,500 psi, the specific gravity of the produced fluid does not show any significant changes, and on average the specific gravity of 0.82 is observed for 4 nm pore. The kerogen nanopores obviously contribute to the lighter gas production as the primary recovery process proceeds. This simply cannot be attributed to relatively higher diffusivity of light hydrocarbons but to the energy balance among the molecules within nanopores.

Next, the impact of CO_2 injection on the produced fluid specific gravity is investigated under constant pressure drop. The results are shown in Figure 4.9b. X-axis of the plot is the mole fraction of the injected CO_2 in the bulk phase, and each data line is at fixed pressure conditions varying from 1,500 psi to 3,500 psi. Interestingly, in contrary to the case of the pressure depletion, CO_2 injection recovers relatively heavier fluids than that of the bulk fluid. The specific gravity of the produced fluid increases with the amount of CO_2 injected. Especially, at 1,500 psi, a sharp increase is observed over all pore sizes when the composition reaches 70 %. As discussed earlier, low amounts of CO_2 are not sufficient to strip off the heavy components in nanopores. When the injected CO_2 amount is sufficient to fill up more than a half of the bulk phase (> 50 %), the recovery of heavy components takes place, and this leads to increase in the specific gravity.

4.4. Conclusions

In this work, we addressed the stripping effects of CO_2 to the capillary-condensed hydrocarbons in kerogen. The results show that CO_2 injection clearly extracts more hydrocarbons than that produced due to pressure depletion only. Also, higher injection pressure leads to higher recovery. This suggests that high-pressure CO_2 injection could be effective in the field for recovering fluids from the organic material. The high pressure injection could be also preferable, because depletion increases the effective stress, which leads to significant change in fluid pathway and decrease in the permeability the source rocks. Then, one critical decision in optimization of enhanced production is how early the injection process should start in order for the wells to maintain a significant injectivity. In addition, supercritical CO_2 as a fracturing fluid has been highlighted (Middleton et al.

2015). However, it is possible that CO_2-induced swelling of rocks reduces the permeability (de Jong et al. 2014; Espinoza et al. 2014).

CO_2 injection can shift the vaporization pressure of the capillary condensed fluids and increase the hydrocarbon production from the nanopores significantly. For the condensed fluids, however, increasing the pressure drawdown has no impact on the thermodynamic recovery. In addition, CO_2 injection recovers heavier fluids from nanopores compared to the pressure depletion production.

In this study, we focused on understanding the statistical behavior of complex hydrocarbon fluid mixtures stored in the organic nanopores rather than the time-dependence of the system. The latter task is challenging and important for multi-component fluids. Nonetheless, the present work provides new insights and a fruitful discussion into the lean gas injection and recovery of the capillary-condensed hydrocarbons based on extensive molecular simulation data. It is hoped that the work provides an impetus for further experimentation in the laboratory or in the field.

5. MOLECULAR SIMULATION INVESTIGATION OF KEROGEN OIL RECOVERY USING ETHANE INJECTION[3]

Organic matter in source rocks stores oil in significantly larger volume than that based on its pore volume due to so-called nanopore confinement effects. However, during production and depletion, recovery of that oil is low. In our previous studies, we introduced the nano-confinement effects and explain their impact on the release of heavy hydrocarbon molecules. Here, we propose to control these effects and increase the oil recovery using lean gas injection, such as ethane. Molecular Monte Carlo simulation method is used for the investigation. The lean gas molecules are introduced to the nanopores by adjusting the bulk fluid composition and pressure to the desired values. Simulations are used to predict fate of in-situ and the injected molecules when the system is reached to equilibrium. Results show that oil in smaller nanopores is richer in heavy components compared to the bulk oil outside in the micro-crack. Compared to gas reservoirs, the impacts of the nano-confinement on in-place fluid volume is not significant. Recovery of the confined oil is typically below 15 % indicating that pressure depletion and fluid expansion is no longer an effective recovery mechanism. Ethane injection shows higher recovery performance than CO_2 injection; it improves recovery up to 90 %, depending on its composition in the fracture. Ethane recovers 5-20 % higher than carbon dioxide in both large pores and nanopores, because ethane molecules are more effective

---

[3] This chapter is from SPE-195272-MS "Recovery Mechanisms for Nano-confined Oil in Source Rocks using Lean Gas Injection" written by Seunghwan Baek and I. Yucel Akkutlu. It is reprinted here with permission of SPE J., whose permission is required for further use.

in vaporizing the heavier molecules in the pore. In addition, ethane reduces viscosity of the confined oil, and its diffusion is faster than CO_2. In summary, lean gas injection is effective in recovering the oil but its delivery to the matrix using fractures and micro-cracks under closure stress makes injection operations challenging in the field.

5.1. Preliminaries

One important reservoir engineering aspect of oil and gas production from source rocks (such as mudstones, siltstones and carbonates) is that the formation may contain significant volume of organic materials. The organic materials found in source rock reservoirs are metamorphosed solid or semi-solid form of what originally used to be biomass deposited in marine environment. Biomass has gone through a series of physical and chemical processes of thermal maturation and petroleum fluids generation. These processes create a complex multi-scale pore structure contributing to the storage of hydrocarbons, including fractures, micro-fractures and cracks, and organic pores down to a few nanometers (Loucks et al. 2012). Organic pores form when fluids are generated, whereas the cracks and fractures form when the generated fluids could not migrate in the primary pore network fast enough and built up sufficient local pressure (in times significant over-pressure) for rock failure.

Literature exists on the storage and transport of fluids in naturally occurring fractures. The challenge here is the characterization of the source rock reservoir in terms of its fracture frequency of occurrence, fractures' geometry, orientation and azimuth, and finally the fractures' stress-dependence under the influence of production and injection. New monitoring and flow simulation technologies are developed considering these fractures as discrete reservoir features embedded into the matrix. The matrix, on the other hand, as commonly known, is too tight with low porosity and ultra-low permeability (Javadpour 2009; Kang et al. 2011). Laboratory measurements of source rock samples have stress-sensitive matrix permeability (Akkutlu and Fathi 2012; Kim et al. 2018). X-ray CT images show the presence of fine-scale micro-fractures as the evidence of this sensitivity, although it is argued that some of these small-scale features are artificial, and they are a product of coring, cutting and desiccation (Ambrose et al. 2012).

Beyond the complexity of the multi-scale fractures, another challenge facing the unconventional reservoir engineer is the presence of the organic pore volume. Ambrose et al. (2012) discussed pore-scale considerations on the volumetric gas in-place calculation for highly-mature source rocks with significant kerogen pore volume, e.g., Barnett, Fayettville, Marcellus. They argued that kerogen pore network has a large specific surface area associated with the organic nanopores, and this creates not only an additional gas storage in the form of sorption but, if the total pore volume of the matrix is too low, also creates a sorbed phase, which reduces the total pore volume available for the free gas phase. They argued it is especially the case for high TOC source rocks. In other words, although the operators may not target the sorbed (adsorbed and absorbed) gas in the formation for economical production rates, the sorption of methane-rich natural gas molecules in high TOC source rock reservoir systems needs to be carefully evaluated for the estimation of the free gas amount that will be produced.

The technical challenges associated with the liquid-rich (condensate, light oil) source rocks appeared in the literature later due to the history of development of these unconventional resources in North America. The source rock could be a massive formation not only with gas but also with condensate and liquid windows that change with depth and location, such as Eagle Ford. Or it could be a liquid-rich source rock interspersed with non-source rock reservoirs, as in the case of the resources in the Permian Basin. The presence of organics brings added complexity for these liquid-rich reservoir systems. Firstly, the organic material is exposed to lower temperature maturation and, hence, the organic pore network is not as highly-developed as the network of the mature and over-mature natural gas window. Hence, the production of liquids from kerogen will be impacted by an under-developed network of organic pores.

Both migration and production processes require transport in the organic porous medium, but transport for production is significantly accelerated. Secondly, the organic nano-pores hold diverse multi-component hydrocarbon mixtures consisting of not only the natural gas components such as methane and ethane but also the heavier ones. In some of the source rocks bitumen appears as the “transitional” organic material, which could be part of the solid or part of the fluid, depending on its composition, reservoir temperature and pressure. In the former case, bitumen adds to the organic porosity of the formation, whereas in the second case it takes up the organic pore space. We will first consider the complexities of oil storage in the organic pores under nano-confinement effects, and we delve into the characteristic behavior of oil during primary production and pressure depletion. Following the depletion, we will discuss the nature of the residual oil in the

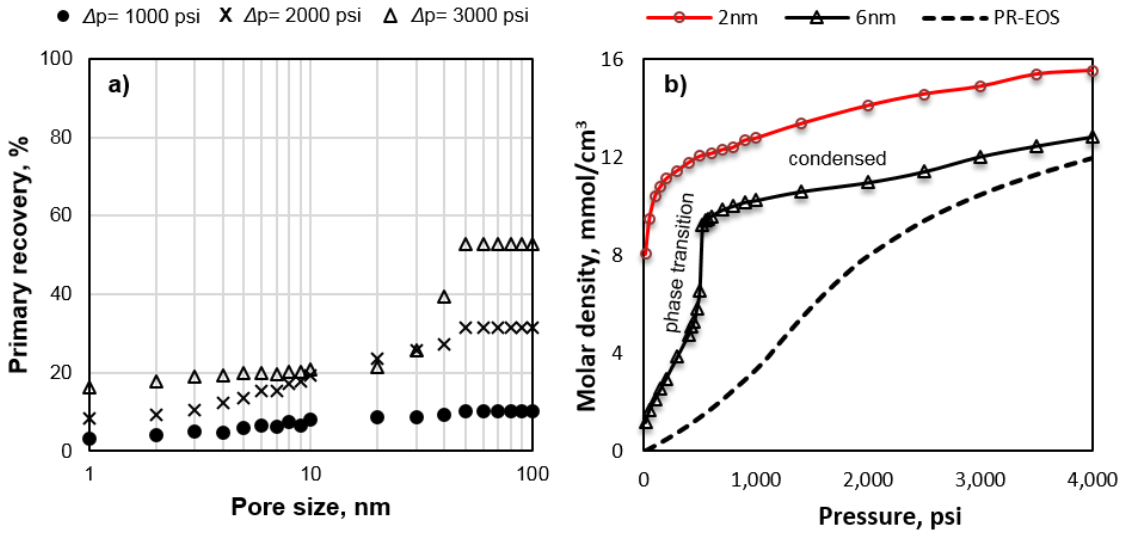

Figure 5.1 Hydrocrabon recovery from model kerogen nanopores and fluid density isotherm.

organic material and discuss how to enhance the recovery using ethane (C_2H_6) and comparing that recovery to using CO_2.

The pressure depletion effect on the recovery of hydrocarbon mixtures stored in model organic pores is shown in Figure 5.1a. These results have previously been obtained and validated using Monte Carlo molecular simulations by Baek and Akkutlu (2019a and 2019b). Further details of the simulation method will be given in the next page, since we use a similar method of computation in the presence of injected gas molecules. This is when we will compare the changes in results as enhancement in recovery due to the presence of the injectant.

Based on the previous works by Baek and Akkutlu (2019a), during production and pressure depletion, the lighter end of the fluid is produced and, hence, the composition of the residual hydrocarbons left inside the nanopores becomes even heavier. The primary recovery is due to two separate mechanisms. One of the mechanisms is heavily discussed in the conventional reservoir engineering as the fluid expansion mechanism (Craft and Hawkins 2015). The hydrocarbon molecules are removed from the pores, and the voidage created by the removal of the molecules is immediately filled up by the expansion of the fluid molecules left behind. This is a highly effective recovery mechanism for the conventional natural gas reservoirs and, in the case of source rocks, it is the dominant recovery mechanism in the large organic pores with sizes 40 nm or greater. With the gas expansion, Baek and Akkutlu (2019a) showed that 53 % of the hydrocarbons in-place can be produced for this multi-component fluid system in the large pores. In the smaller pores, however, the fluid expansion becomes less efficient with the decrease in the pore size. When the pore size is reduced below 10 nm, the recovery is controlled by the walls and, hence, the fluid cannot easily expand. At this scale the recovery is dominated by desorption of the fluid molecules from the pore. Desorption mechanism, however, is not as effective as the fluid expansion, and therefore the recovery drops significantly. The recovery from pores less than 10 nm does not exceed 20 % with 3,000 psi of pressure drop (Figure 5.1a).

Baek and Akkutlu (2019a) also discussed the compositional variability due to nano-confinement effects leading to phase change in an unpredictable way. Their discussion is summarized in Figure 5.1b, which shows the molar density of the fluid as a function of pressure. The figure clearly shows that the fluid in nanopores experience capillary condensation, although its bulk fluid composition does not show any phase change. It is difficult for the residual hydrocarbons to leave the pores, because it is the lighter hydrocarbons that have been produced. So, the residual hydrocarbon in nanopores becomes progressively more difficult to recover during the depletion, because desorption of heavier hydrocarbons is less effective than the light hydrocarbons. Note that the phase transition is driven by the compositional variation of the fluid inside pores, and it is very unusual because the reservoir conditions are extreme enough to have fluids in a supercritical state (Gelb et al. 1999). This shows well that nano-confinment effects substantially influence the fluid behavior in nanopores (Li et al. 2014; Rahmani and Akkutlu 2015; Pitakbunkate et al. 2017).

The nano-confined fluids in Figure 5.1b show vaporization of the capillary-condensed fluid at 100 psi, and 525 psi in 2 nm and 6 nm pore, respectively, during the pressure depletion. In essence, the isotherms show that the estimated recoveries were low because the fluid mixture was capillary-condensed in the pore, and that the pressure reduction needed to vaporize the in-situ hydrocarbons was much less than the applied pressure. This indicates a limited ability of pressure depletion to recover the confined fluids from organic nanopores. These computational results raise serious questions on the ultimate recoveries from organic-rich source rocks. Reducing the flowing bottomhole pressure to values less than 500 psi could be impractical in some of the highly over-pressured source rocks.

One approach to the problem could be to inject relatively inexpensive lean gases such as ethane (C_2H_6) and carbon dioxide (CO_2), into the formation once sufficient depletion near the hydraulic fractures is achieved for injection (McGuire et al. 2016). Baek and Akkutlu (2019b) recently extended the molecular simulation of hydrocarbon mixtures and showed the impact of CO_2 injection on the hydrocarbon recovery from kerogen organic nanopores. CO_2 molescules introduced into the nanopore lead to exchange of molecules and a shift in the phase equilibrium properties of the confined fluid. This exchange has a stripping effect and in turn enhances the hydrocarbon recovery. The CO_2 injection, however, is not effective for the recovery of heavy hydrocarbons as much as for the light components in the mixture. Those large molecules left behind in nanopores mainly make up the residual (or trapped) hydrocarbon amount. They argued that high injection pressure leads to significant increase in recovery from the organic nanopores but not too critical for the recovery of the bulk fluid in large pores. Large pressure drop and the associated fluid expansion leads to recovery from the large pores. Diffusion of CO_2 into nanopores and the exchange of the molecules are the primary drives that promote the recovery from organic pores, whereas pressure depletion is not effective on the recovery.

The discussion indicates that the compositional variability due to pore size and pressure change does not help recovery of oil from the organic nanopores. In this paper, we discuss if we can improve the recovery using ethane to a level beyond that experience with CO_2.

5.2. Fluid and Reservoir Models

The model oil that will be used in our computations has the following composition: 33 % CH_4, 33 % C_3H_8 and 34 % n-C_5H_{12}. The average molecular weight of the oil is 44.1 g/mol. When we add ethane or CO_2 into the bulk phase, the in-situ fluids composition becomes quaternary. The injectant is introduced to the bulk phase such that we maintain 10 %, 50 % and 90 % composition of the bulk mole fraction, and the molecular simulation predicts the fluid composition inside nanopore based on energy minimization. Figure 5.2 shows the pressure-temperature phase diagram of the ternary model oil. We shall perform the computations under fixed reservoir temperature of 176 °F.

In order to show the impact of nanopores on the hydrocarbon in-place, one organic rich shale sample with known pore-size distribution is considered as in Figure 5.3 (Shultz 2015). During the calculations, we assume 5 % total porosity (ϕ), 2.5 g/cm3 bulk density (ρ_b) and 35 % immobile water saturation (S_W).

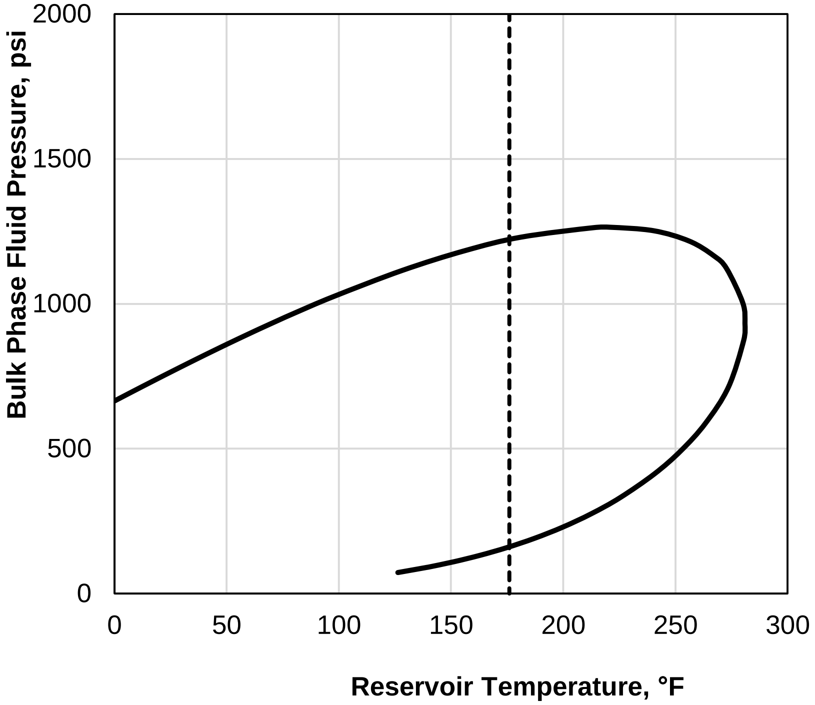

Figure 5.2 Pressure-temperature phase diagram of the shale oil considered.

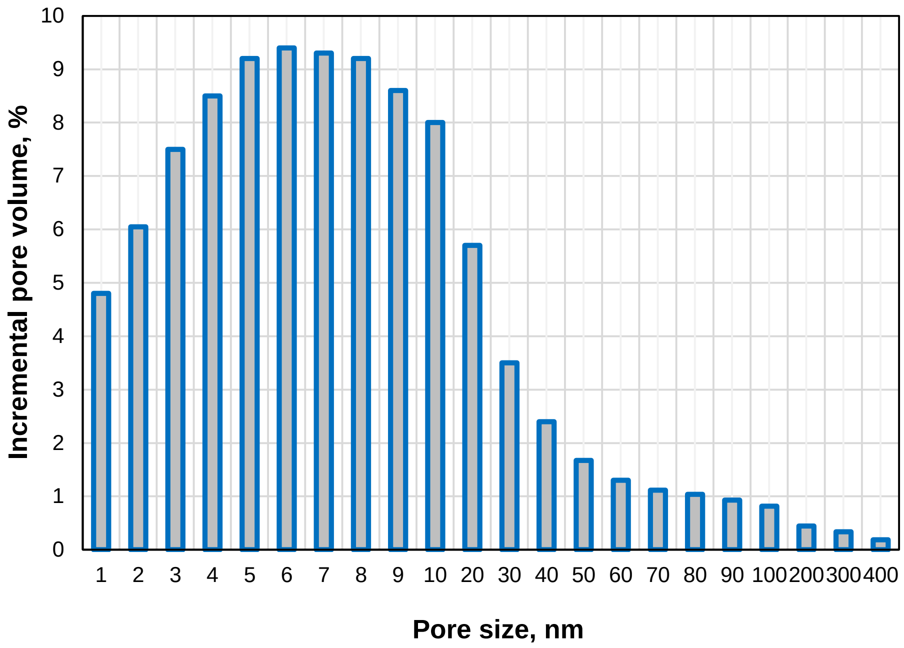

Figure 5.3 Pore size distribution of the organic-rich shale sample used.

5.3. Results and Discussion

Figure 5.4 includes molecular simulation results showing the initial distribution of the oil in a model reservoir. On the left, we clearly observe the impact of nanopores to the storage. The cumulative hydrocarbon in-place curve has an increase in the volume of stored fluids in pores with sizes less than 10 nm. Figure 5.4a shows that nano-confinement effects contribute to the storage an additional 10 %. This is significantly less than that observed for natural gases. In a recent study, a gas reservoir showed 50 % of the increase in estimated original gas in place (Baek and Akkutlu 2019a). Although the difference depends on the fluid composition and pore size distribution, our comparison indicates that nanopore consideration does not have significant impact on the initial hydrocarbon volume in the oil reservoirs. In Figure 5.4b, we observe that the nanopores store pentane

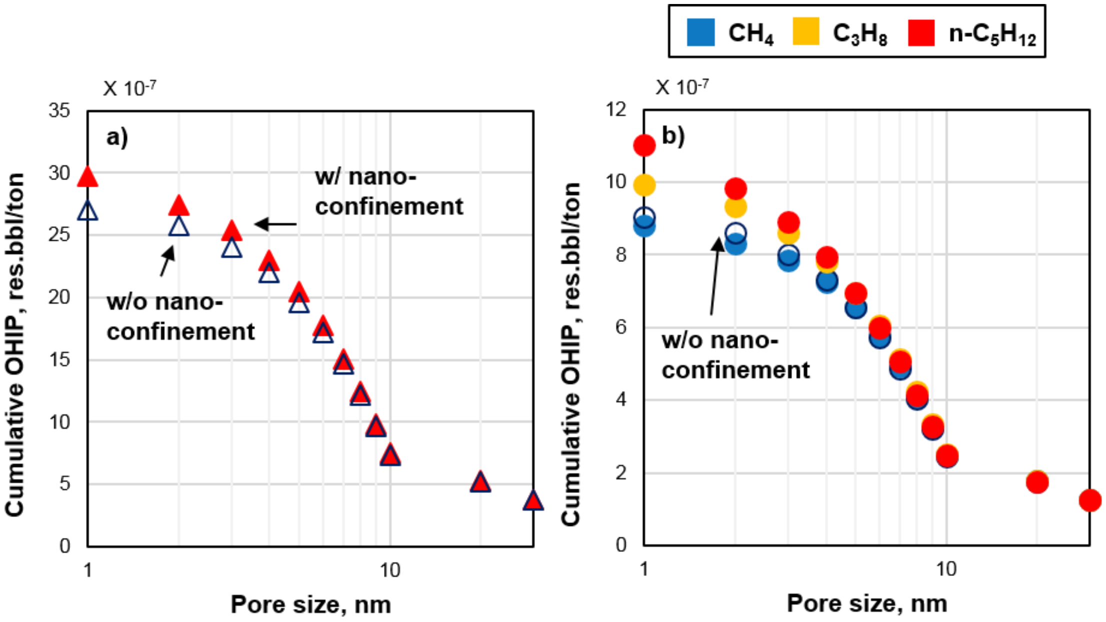

Figure 5.4 Initial oil distribution at a model reservoir at 4,000 psi.

more than the others. The pores are richer in the amount of pentane as the pore sizes become smaller, which is in agreement with our previous discussion on the nano-confined fluid behavior: the smaller the pore is, the heavier its hydrocarbon mixture becomes. The estimated in-situ fluid composition under nano-confiment is 30 % CH_4, 33 % C_3H_8 and 37 % n-C_5H_{12}. However, without nano-confinement, the mole fraction of each component was set equal. This compositional variation is difficult to be captured with a conventional approach, and the qualitative deviation will have huge impacts on PVT analysis, eventually reserve evaluation and production forecasting.

Now let us discuss what happens to these nano-confined fluids, if the model organic pores are exposed to pressure depletion. Figure 5.5a shows the pressure depletion effect on the oil recovery from nanopores. We considered depletion from 4,000 psi down to 3,500 psi, 2,500 psi, and 1,500 psi. The confined fluids and the bulk fluid in large pores maintain liquid state during the pressure drop. Because the volume expansion of liquid hydrocarbons is limited, we expect low recovery from these pores. As pressure drops the nano-confinement becomes more pronounced and, consequently, less hydrocarbons are released from the pores. The computed maximum recovery at Δp = 2,500 psi is less than 15 % of the original oil in place for the large pores whereas it is less than 10 % for the nanopores with sizes less than 10 nm. In a gas reservoir, the recovery was less than 20 % in nanopores (Baek and Akkutlu 2019a). Clearly, in nanopores the liquid (or condensed) phase molecules experience amplified attractive forces from the pore surface. However, the recovery from nanopores and large pores is consistent until Δp = 1,500 psi. This implies that nano-confined fluids and bulk fluids can share the same recovery mechanism above 2,500 psi reservoir pressure. Our results show that, even in the presence of strong nano-confinement, oil recovery from organic nanopore is possible, and it is just as difficult as that from the large pores.

Our previous study (Baek and Akkutlu 2019b) discussed that the organic matter near the fractures should yield more gases because near the fracture the fluids in the matrix are exposed to higher concentrations of the injectant. Away from the fractures, on the other hand, the recovery becomes slave of the network quality of the multi-scale fractures, and molecular diffusion of the injected fluid into the matrix. Here, in the same manner, the enhanced oil recovery with ethane injection is demonstrated and compared with CO_2 injection in Figure 5.5b. The production is simulated first due to pressure depletion from

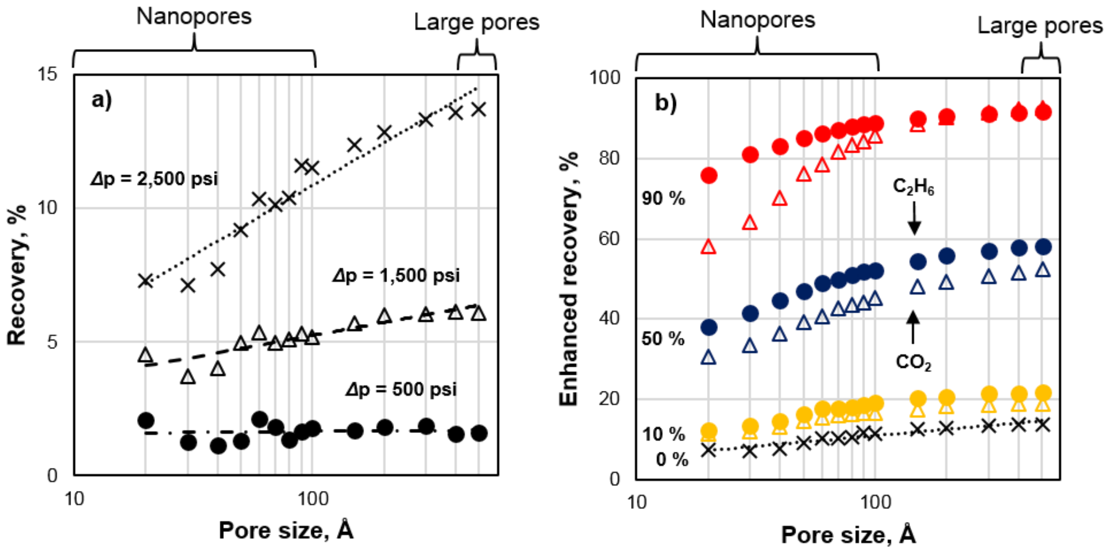

Figure 5.5 Recovery of oil from individual organic pores.

an initial pressure of 4,000 psi down to 1,500 psi and, next the injectant is introduced at 1,500 psi. The primary recovery is also shown for comparison using mark x. The y-axis indicates the enhanced recovery considering both the pressure depletion and the gas injection. As expected, more injection leads to more production from organic pores. Further, oil recovery performance due to ethane injection outweighs that with CO_2 injection. This is the case for all the pores. Especially, at the level of 90 % injection shown in red, the ethane injection recovers significantly more nano-confined hydrocarbons. Note that up to 50 %, ethane injection produces more hydrocarbons than CO_2 injection from large pores. For large pores, since the adsorption effect is negligible, the chemistry of the pore surface is not important, this result can be extended to inorganic large pores.

Figure 5.6 shows the compositional changes in the produced oil due to ethane and CO_2 injection. Here, our attention is on the recovery of the heaviest component, i.e., pentane, because it indicates the effectiveness of the injected fluid in stripping the adsorbed heavy components by the walls. Clearly, the portion of pentane in the produced fluid is sensitive to the injected fluid type. Regardless of the pore size, introduced ethane yields higher portion of pentane from the organic nanopore than CO_2, and this is probably the reason for the higher recovery in Figure 5.5b. The composition of pentane in the fluid produced from 2 nm pore is always higher than that from 20 nm (not shown). This is because the in-place fluid composition varies over different pore size due to nano-confinement, and more heavy components exist in smaller pores as discussed above. Ethane injection leads to the recovery of hydrocarbons with higher specific gravity than the fluids from either CO_2 injection or pressure depletion production.

The viscosity is measured for the confined oil and the injectant-included mixtures using Green-Kubo relations and molecular dynamics simulation. The results are shown in Figure 5.7a. As expected, as the injectant is introduced into the fluid mixtures in nanopores, the viscosity of the mixture is reduced. Overall, while ethane injection causes higher enhancement in mobility, the difference is negligible in 2 nm pores. At CO_2 = 10 % in 20 nm, a peculiar increase in viscosity is observed. This is because there are many of methane molecules over the entire pore space (especially in the center of the pore) and CO_2 molecules displace them from the pores. CO_2 has higher viscosity than methane, thus, adding CO_2 increases the viscosity of the confined fluid. On the other hand, in a small pore such as the 2 nm pore, due to nano-confinement effects, a large number of propane

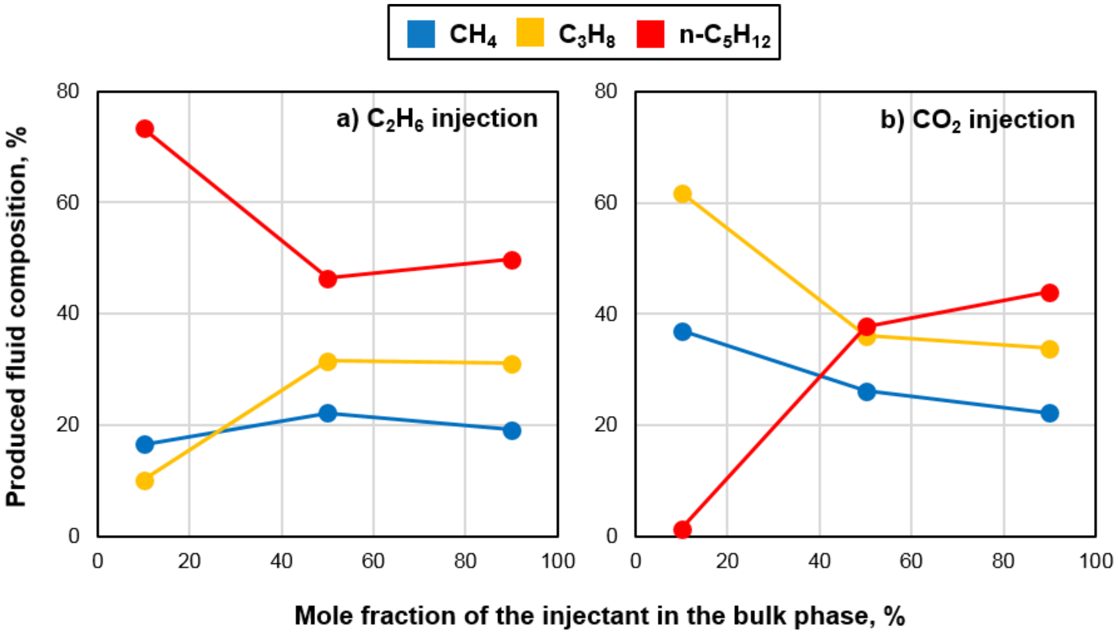

Figure 5.6 The composition of the fluids produced from 2 nm at 2,500 psi.

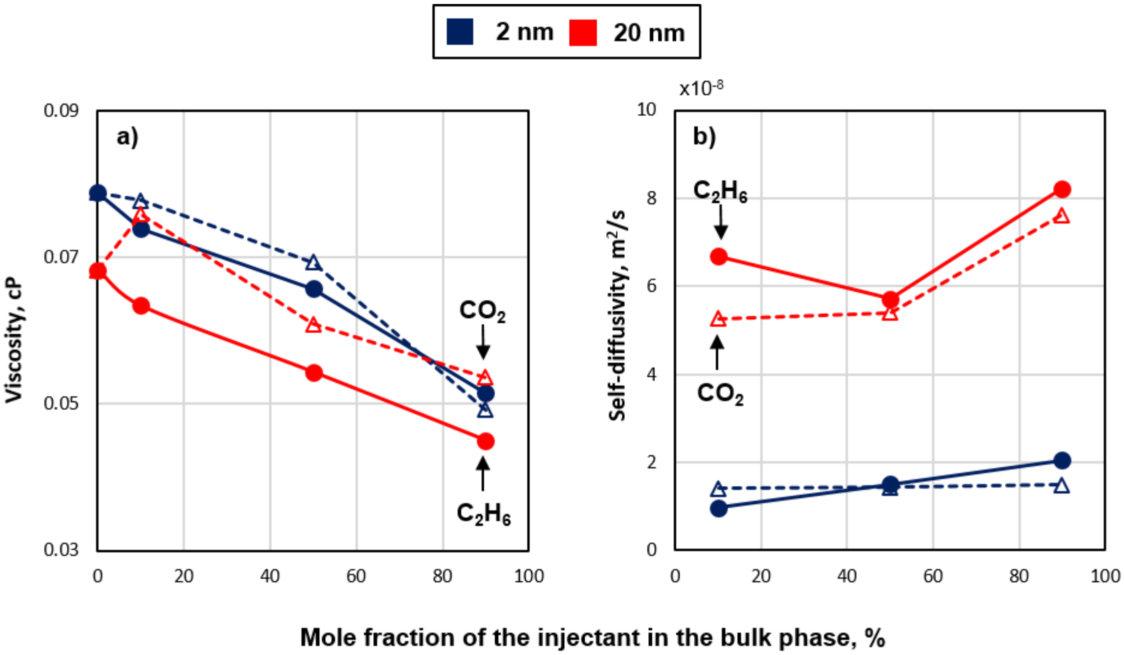

Figure 5.7 Transport properties of nano-confined fluids in 2 nm and 20 nm pores at 2,500 psi.

molecules exist in the mixture compared to methane, and more of propane is stripped off by CO_2. Since pure CO_2 has less viscosity than pure propane, the viscosity of the diluted mixture is decreased. Also, shown in Figure 5.7b, ethane diffuses into hydrocarbon mixtures faster than CO_2 in most cases. In general, however, the type of the injectant is not critical in fluid transport properties in small nanopores.

5.4. Conclusions

In this paper we consider lean gas injection to enhance confined oil recovery from source rocks. Using molecular simulations we show that low-cost injection gases such as ethane and carbon dioxide is effective in confined oil recovery. Near the fractures, where high concentrations of lean gases are delivered, the recovery is highly effective. Ethane, in particular, has clear advantages over carbon dioxide because ethane controls desorption of heavier hydrocarbons from the pores more effectively and, hence, can improve the recovery efficiency.

6. SHALE GAS WELL PRODUCTION OPTIMIZATION USING MODIFIED RTA METHOD – PREDICTION OF THE LIFE OF A WELL[4]

Routine history-matching and reservoir calibration methods for horizontal wells with multiple hydraulic fractures are complex. Calibration of important fracture and matrix quantities is, however, essential to understand the reservoir and estimate the future recoveries. In this paper, we propose a robust method of simulation-based history-matching and reserve prediction by incorporating an analytical solution of production Rate Transient Analysis (RTA) as an added constraint. The analytical solution gives the fracture surface area contributing to the drainage of the fluids from the matrix into the fractures. The surface area obtained from the RTA is the effective area associated with the production—not total area. It is the most fundamental and the most significant quantity in the optimization problem. Differential evolution (DE) algorithm and a multi-scale shale gas reservoir flow simulator are used during the optimization. We show that the RTA-based optimization predicts the quantities related to completion design significantly better. Further, we show how the estimated total fracture surface area can be used to measure the hydraulic fracturing quality index, as an indication of the quality of the well completion operation. The most importantly, we predict that the fractures under closure stress begin to close much sooner (100 days) than the prediction without the RTA-based fracture

---

[4] This chapter is from URTeC-185 “Shale Gas Well Production Optimization using Modified RTA Method – Prediction of the Life of a Well” written by Seunghwan Baek, I. Yucel Akkutlu, Baoping Lu, Shidong Ding, and Wenwu Xia. It is reprinted here with permission of SPE J., whose permission is required for further use.

surface area constraint. The deformation continues under constant closure stress for about 20 years, when the fractures are closed nearly completely. This work attempts to use the traditional reservoir optimization technologies to predict not only the reserve but also the life of the unconventional well.

6.1. Preliminaries

Resource shale and other source-rock formations are important oil and gas resources. Technical advances in horizontal drilling and hydraulic-fracturing have been the major factors in achieving economical production from these unconventional resources. However, the economics can be further improved by increasing the productivity of the existing wells. Well completion design and production optimization play an important role in increasing the productivity of the unconventional wells.

In order to improve the productivity of the existing wells using production optimization, we can use the existing optimization technologies that have already been developed for the conventional wells during the last decades. The classical problem of interest to the reservoir engineers is the estimation of the formation properties (such as the porosity and permeability fields) by history-matching the production data (Oliver, Reynolds, and Liu 2008). Currently we have various methods available in both deterministic and probabilistic frameworks. These methods overwhelmingly use a reservoir flow simulation model to history-match the production of a well or a group of wells in the field and to forecast the reserve. However, history-matching and production forecasting of the unconventional wells, such as the horizontal shale gas wells with multiple fractures, has fundamentally different focus. Primary optimization parameters that show significant sensitivities are, in this case, the fracture geometry (i.e., its length, width, and height), the fracture conductivity, the fracture spacing (or number of fractures) and the fracture complexity. Although a horizontal well's lateral length and the number of hydraulic fracturing stages are known accurately, the nature of fractures contributing to the production is poorly understood. This lack of knowledge brings in added complexity and uncertainties to the optimization process when the reservoir engineer is not only required to consider the key matrix parameters (such as porosity and permeability) and the geological impact on these parameters, but also the completion qualities such as the hydraulic fracturing design. This is a challenging task because various aspects related to the reservoir and the completion should be considered simultaneously. Several attempts have previously been made to optimize the transverse fractures for unconventional gas wells (Britt and Smith 2009; Marongiu-Porcu, Wang, and Economides 2009; Zhang et al. 2009; Bagherian et al. 2010; Gorucu and Ertekin 2010; Sarmadivaleh et al. 2010; Bhattacharya and Nicolaou 2011; Wilson and Durlofsky 2012; Bazan et al. 2013; Kim, Olalotiti-Lawal, and Gupta 2019). Plaksina and Gildin (2015) recently applied the multi-objective optimization algorithm for the hydraulic fracture placement. The objective function included economic constraints and production-related factors, which can be differently weighted depending on the users' target. The suggested framework does not require weighting assignment to individual objective and provides an optimal set of the solutions for fracture placement balancing between profit and cost.

The production history-matching and optimization methods allow us to characterize the reservoir and forecast the reserve. However, substantial computational cost occurs as a trade-off against better characterization and forecasting, and consequently, various strategies were suggested to reduce the cost. Yang et al. (2017) investigated the optimal multi-stage hydraulic fracture configurations for heterogeneous reservoir models. Fracture geometry and fracture placement were coupled and optimized simultaneously using a genetic algorithm. The use of a fast-marching method allowed them to conduct the optimization efficiently. Rahmanifard and Plaksina (2018) integrated an analytical solution representing flow to the fracture into stochastic gradient-free optimization algorithm to design transverse fractures of horizontal wells. The incorporation of the solution enabled the framework to be efficient compared to the simulation-based optimization. The fracture attributes, such as the number of stages, the fractures length, distance between the wells, were calibrated for the optimal design. Chai et al. (2018) recently developed a probabilistic approach, the so-called improved compartmental embedded discrete fracture model (cEDFM), combining the level-set approach and the ensemble Kalman filter (EnKF) for the production history matching. The proposed approach allowed the discrete fractures characterized explicitly for multiphase-flow problems and low-permeability flow barriers.

The existing methods use the well’s production rate-transient as the observation data that must be honored during the optimization. However, the rate transient has additional information that could be used for improved accuracy: the fracture surface area. The production begins with the linear and bilinear flow of fluids in the fracture when the fracture volume and conductivity are the key quantities. But this time period is ephemeral, and it is followed by long-term formation linear flow, when most of the produced fluids are those flowed from the matrix to the fracture. During the formation linear flow the area of the fractures contributing to the production becomes the key quantity. The fracture surface area can be estimated if the number and geometry of the fractures are known. However, uncertainties exist on these completion-related quantities. The industry uses micro-seismic data, production logs, wellbore image logs and tracer test to characterize the fractures (Hetz et al. 2017). These methods have limited application, however, because the data is costly, or the formation holds a relatively complex network of fractures where identifying individual wing-like planar fractures could be difficult. A common approach is to measure the fracture surface area directly using the well production data along with an RTA method. The most widely used approach is the method also known as $A\sqrt{k}$ method, originally proposed by Wattenbarger et al. (1998). The method is used to estimate the fracture surface area from the production decline as a straight line. Pelaez-Soni, Akkutlu and Maggard (2017) recently suggested a modified version of the $A\sqrt{k}$ method considering stress-dependent matrix permeability during the straight line analysis. Permeability of the shale gas formation could vary for several reasons (Wasaki and Akkutlu 2015) but it is mainly the stress-dependence of the permeability that leads to dramatic changes in its value. They showed elimination of the dynamic permeability due to stress change could give 80% error in the estimated fracture surface area.

In this study, a new simulation-based optimization approach is presented for the shale gas production wells. The method is based on a robust shale gas flow simulator and uses DE algorithm for optimization. It considers the field transient data (pressure and production rate) and the RTA-based fracture surface area as the basis during the calibration

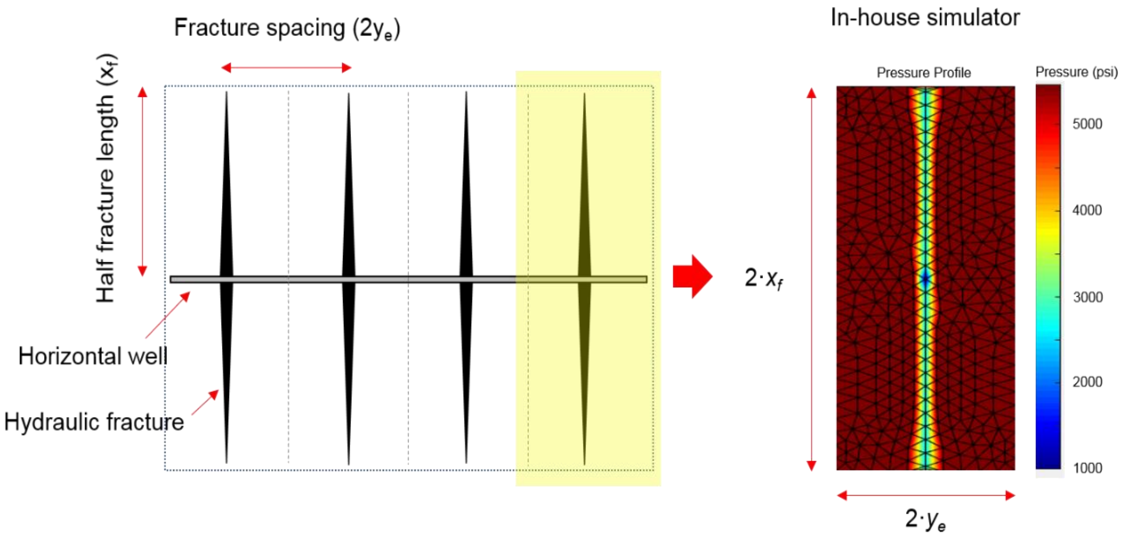

Figure 6.1 Schematic of hydraulically fractured formation model.

of the matrix and fracture properties. The modified version of the RTA method is adopted during the optimization, which considers dynamic matrix permeability. The paper is developed as follows. First we will discuss the features of the reservoir flow simulation and the reservoir model we have developed for this work. Briefly, we shall describe DE algorithm. Next we will delve into the details of the workflow for the optimization, in particular, emphasizing how the modified RTA method is introduced to the optimization process as a new mathematical constraint. Finally we will show the optimization results for a shale gas well and discuss the results. One important aspect of this optimization process is that the simulation model considers the production geo-mechanically fully coupled. Hence, not only the changes in fluid pressure but also stress and displacement are computed during the history matching and optimization. Consequently, the results can also shed light onto the long-term geo-mechanical behavior near the hydraulic fractures. We will discuss that closure stress effects are in long-term related to the life of the well.

6.2. Fluid and Reservoir Models

The model fluid is a mixture of methane, ethane and propane but the fluid is nearly pure methane. For gas properties, Peng-Robinson EOS and Lee's viscosity correlation are used (Lee, Gonzalez, and Eakin 1966; Peng and Robinson 1976). Fixed parameters are displayed in Tables 6.1 and 6.2, respectively.

The stencil fracture model will be used as shown in Figure 6.1. The fracture length and fracture spacing define the boundary of the computational domain. The fracture spacing is determined with total lateral length of the well (L_h) and the number of fractures (n_{frac}).

The modified RTA method coupling this dynamic permeability model is adopted for the total fracture surface area estimation of the well (Pelaez-Soni et al. 2017). The modified model is compared to the Wattenbarger's RTA Method (1998) in Appendix E. The flow chart of the approach is also described.

Table 6.1 Fixed parameters for reservoir simulation.

Parameters	Symbol	Value	Field Unit
Reservoir thickness	h	115	ft
Fracture permeability	k_f	50	Darcy
Fracture porosity	ϕ_f	0.33	
Temperature	T	181.13	°F
Well radius	r_w	0.054	in
Total horizontal well length	L_h	4,495	ft
Initial reservoir pressure	p_i	5,466	psi
Large pore cut-off	e_{ps}	0.9	
Tortuosity	τ	3	
Young's Modulus	E_f	5,801,510	psi
Poisson ratio	v	0.25	
Biot Coefficient	α	0.2	
Confining pressure	p_c	10,000	psi
Initial mole fractions	z_i	99.1:0.88:0.02	%

Table 6.2 Variables calibrated during for history-matching and optimization.

	Parameters	Symbol	Range	Unit
Fractures	Fracture half length	x_f	98 — 984	ft
	Initial fracture width	w_0	0.039 — 0.197	in
	Viscoelastic coefficient	η	7.3E10 — 7.3E12	psi-sec
Matrix	Porosity	ϕ	0.03 — 0.09	
	Initial matrix permeability	k_0	0.001 — 0.050	mD
	Exponent in Gangi's model	m	0.10 — 0.99	
	Max confining pressure	P_{max}	9,100 — 16,000	psi

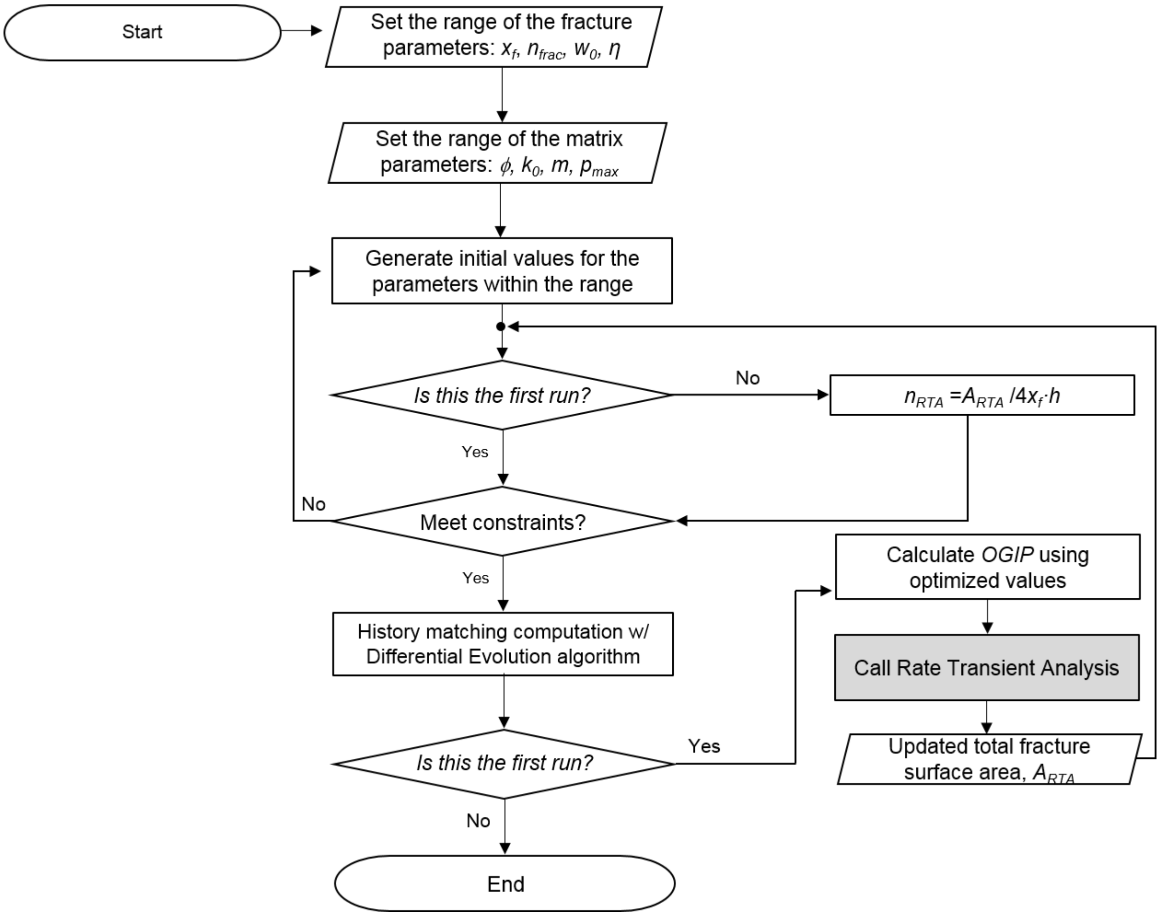

Figure 6.2 Work flow for the optimization.

6.3. Work Flow for the Optimization

The purpose of this study is to show the benefit of using the effective fracture surface area estimated using the modified RTA method during the history-matching and optimization. The detail of the workflow is shown in Figure 6.2. Initial optimization is conducted to approximate the fracture-associated parameters such as fracture half-length (x_f), the number of fractures (n_{frac}), the initial fracture width (w_0), and viscoelastic coefficient (η), and matrix-associated parameters such as matrix porosity (ϕ), Gangi's permeability model parameters (k_0, m and p_{max}).

DE algorithm generates various combinations of parameters within their ranges, and additional constraints are helpful to save the computational time and predict physically meaningful solutions. Three conditions are provided at this stage:

$$y_e = \frac{L_h}{2 \cdot n_{frac}} \tag{6.3}$$

$$Max.\ Cum.Production < \ 0.5 \times OGIP \tag{6.4}$$

$$P_{max} > P_{eff} \tag{6.5}$$

The fracture spacing (y_e) is dependent on total horizontal well length (L_h) and the number of fractures, n. L_h is given as 4,495 ft. Original gas in-place (OGIP) is calculated based on volumetric method with porosity (ϕ), saturation (S_w), fracture half-length (x_f), fracture spacing (y_e), number of fractures (n_{frac}), reservoir thickness (h), initial formation volume factor ($B_{g,ini}$).

$$OGIP = \frac{\emptyset \cdot 2x_f \cdot 2y_e \cdot n_{frac} \cdot h \cdot (1 - S_W)}{B_{g,ini}} \tag{6.6}$$

$$n_{RTA} = \frac{A_{Frac,RTA}}{4 \cdot x_f \cdot h} \tag{6.7}$$

The initially optimized parameters and new OGIP are then fed into the modified RTA, and the effective fracture surface area ($A_{Frac,RTA}$) is estimated based on transient gas flow rate data during the formation linear flow period. Next, the second optimization is carried out, and the obtained $A_{Frac,RTA}$ is used as a new constraint for the number of fractures (n_{RTA}) and fracture spacing (y_e) as shown Eqs. 6.7 and 6.3 ($n_{Frac} = n_{RTA}$), respectively. Consequently, the new optimized parameters honor production history and are constrained by analytical transient rate analysis method.

Figure 6.3 shows the proposed optimization method. Figure 6.3a has the shale gas production well with a total fracture surface area equal to A_{Frac}, with the production rate q_g. Figure 6.3b, the modified RTA method gives the fracture surface area $A_{Frac,RTA}$ for the production q_g. In general, RTA gives the effective surface contributing to the production. Hence, this area is somewhat less than the actual surface area, i.e., $A_{Frac,RTA} < A_{Frac}$, because, although some of the fractures exist, their contribution to production could be reduced or negligible. The optimization considers this effective surface area as a constraint such that not only the production rate but also the effective surface area is honored, i.e., $A_{Frac,OPT} = A_{Frac,RTA}$. As in Figure 6.3c, the optimization returns the number of planar fractures (n_{RTA}) assuming a uniform completion based on Eq. 6.7.

Comparison of n_{RTA} from Eq. 6.7 to the designed value, n_{design} (based on the product of the number of fractures in each stage x number of stages), indicates the quality of the hydraulic fracturing:

$$I_{HF} = \frac{n_{RTA}}{n_{design}} \tag{6.8}$$

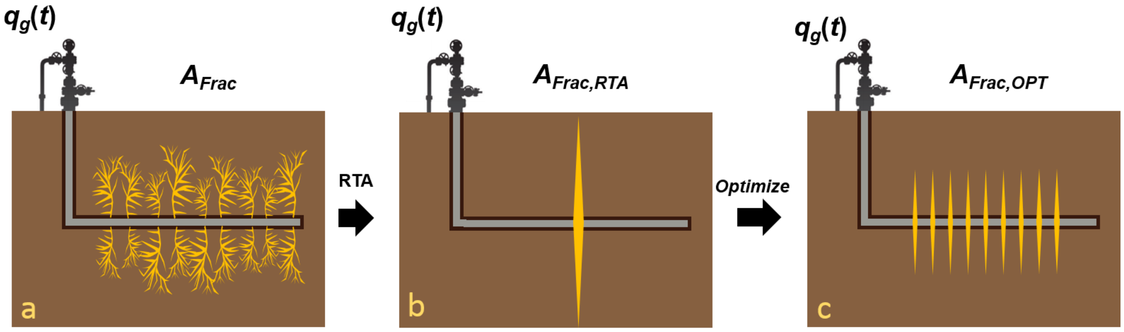

Figure 6.3 Proposed optimization method using modified RTA method as a constraint.

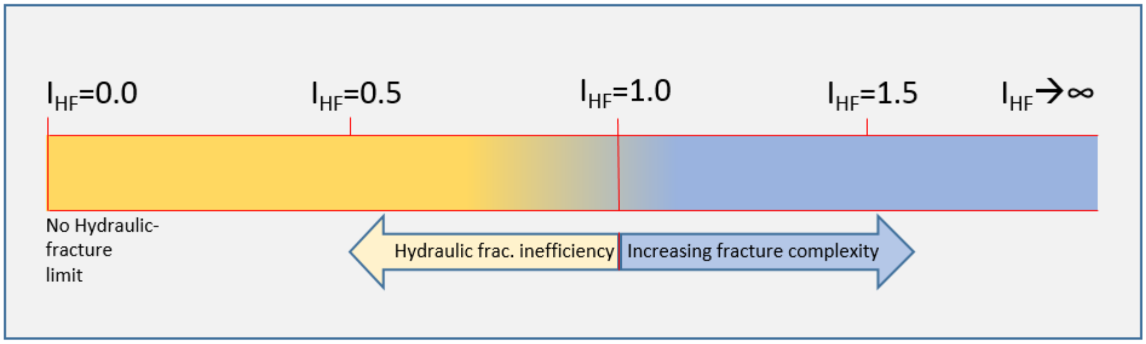

Figure 6.4 Hydraulic fracturing quality index, I_{HF}.

If I_{HF} is close to unity then the hydraulic fracturing is completed as designed. However, if $I_{HF} < 1.0$, for example $I_{HF} = 0.5$, then the completion has been completed with 50 % success. This could be due to unsuccessful stages of fracturing, when the number of fractures is less than the designed number of fractures, and/or it could be due to the presence of un-propped or partially-propped fractures that were formed but did not contribute to the production. If $I_{HF} > 1.0$, then the hydraulic fracturing has been done successfully, and it led to the development of a complex fracture network. These are shown in Figure 6.4. Hence, following the optimization one would proceed and identify the hydraulic fracturing quality and the nature of fracture complexity of the horizontal shale gas well using the hydraulic fracturing quality index.

6.4. Results and Discussion

The gas flow rate (red) and the flowing bottomhole pressure (blue) of a shale gas well from Sichuan basin in China are plotted as a function of the production time in Figure. 6.5. At the time of this analysis, we have data only up to 273 days. The initial reservoir pressure is 5,466 psi. The flow rate drops eventually to zero due to wellbore shut-in.

The gas flow rate and the cumulative gas production are plotted as a function of the production time on a log-log scale in Figure 6.6. Here, we can observe the dominant negative half slope trend in the gas flow rate between 100 and 130 days, indicating formation linear flow. The start of boundary-dominated flow regime is not clear on the plots because the production data only includes this early production history of the well. Pseudo-time (t_{ap}) as given in Eq. 6.9 is calculated using trapezoidal rule, and the plot of the reciprocal of the flow rate versus the square root of pseudo production time is plotted in Figure 6.7.

$$t_{ap} = \int_0^t \frac{k_g}{\mu \cdot c_t} dt \tag{6.9}$$

$$A_{Frac,RTA} = f_{cp} \cdot \frac{1261.2T}{slope\sqrt{(\emptyset)_i}} \cdot \frac{1}{\Delta m_k(p)} \cdot n_{RTA} \tag{6.10}$$

The straight line for the linear flow regime is used to calculate the slope and the effective fracture surface area ($A_{Frac,RTA}$) from Eq. 6.10.

The history-matching and optimization were conducted constraining to the field data, and the best fit result is shown in Figure 6.8. Clearly, the gas flow rate is honored (Figure 6.8b) and the matched pressure profile follows the observed bottom hole pressure well (Figure 6.8a). In Figure 6.8 the blue mark includes the trends without applying the RTA method, i.e., just the optimization was performed. The difference in matched pressure is negligible. For early production up to around 30 days, fractures primarily influence the production history, and afterwards flow in the matrix starts to affect the production. In Figure 6.8a, our matching overestimates the pressure, and more of pressure depletion is needed between 45 and 165 days. This indicates that there are additional obstacles associated with hydrocarbon flow in matrix, we did not catch. Other possibility is on our uniform reservoir and fracture model. Considering further heterogeneity can improve the history-matching while it also increases the computational cost. This will be addressed in a future publication.

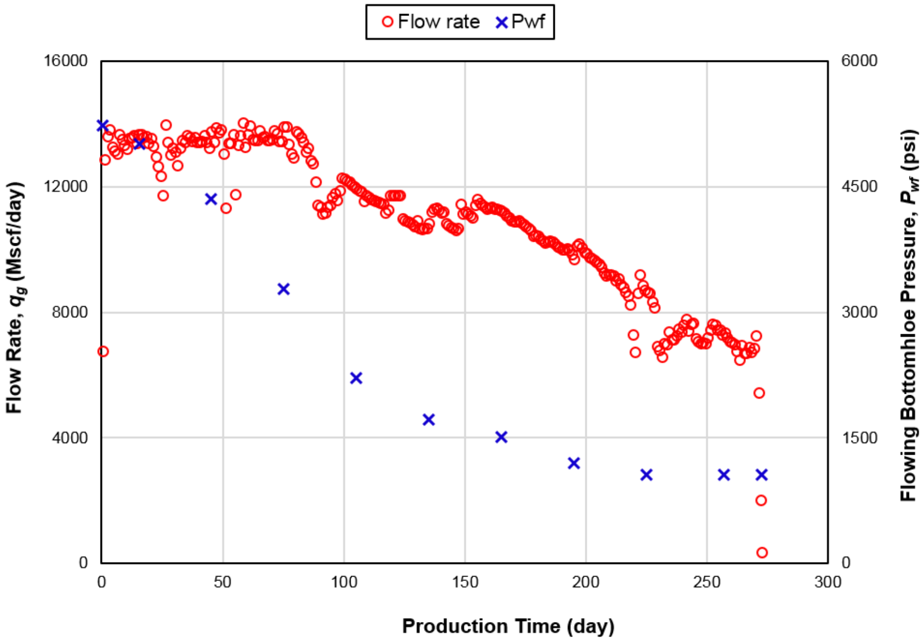

Figure 6.5 Production history plot of gas flowrate (q_g) and calculated bottomhole pressures (P_{wf}) versus production time.

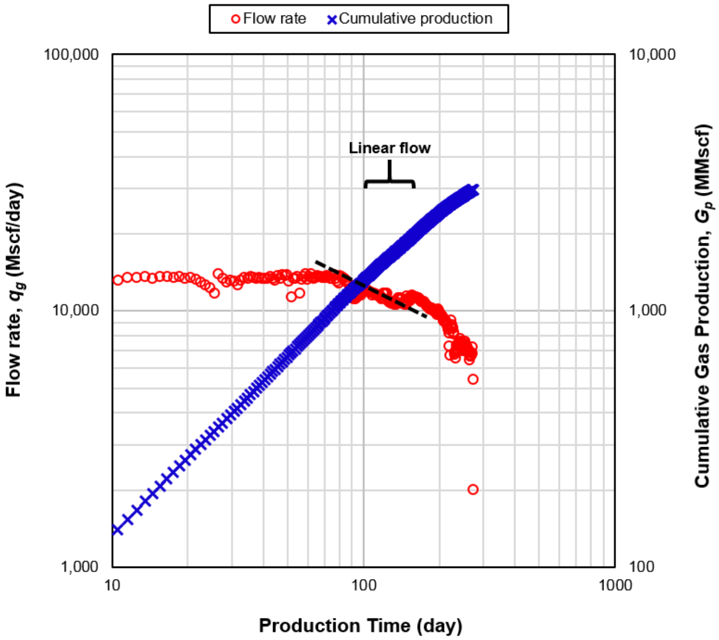

Figure 6.6 Gas flow rate (q_g) and cumulative gas production (G_p) versus production time (Log-Log scale).

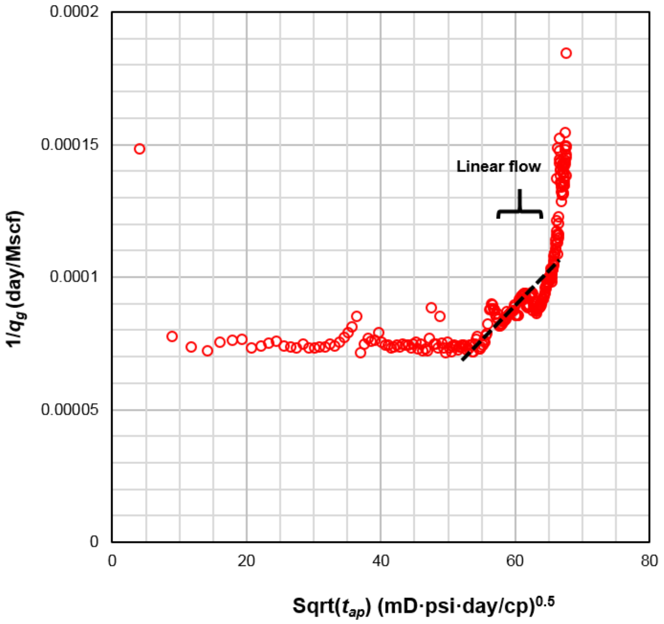

Figure 6.7 The reciprocal of the gas flowrate (1/q_g) versus square root of pseudo production time (sqrt (t_{ap})).

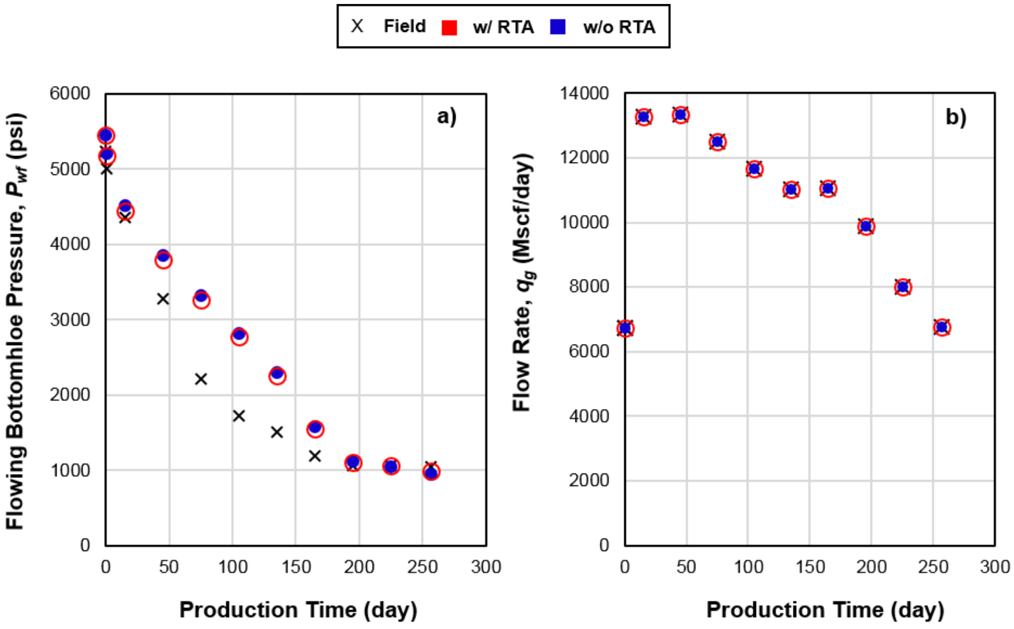

Figure 6.8 History-matching and optimization results with and without rate transient analysis.

Table 6.3 Comparison of optimization results.

	x_f	w_0	η	ϕ	k_0	m	P_{max}	n_{frac}	A_{Frac}
	ft	*in*	*psi-sec*		*mD*		*psi*		*acre*
without RTA	643	0.138	3.3E+12	0.044	0.0268	0.309	10,512	61	414
with RTA	427	0.278	1.9E+12	0.069	0.0419	0.480	10,334	33	149

The optimized variables are compared in Table 6.3. Although the difference in history-matched pressure data in Figure 6.8a is negligible, the optimized values vary significantly depending on the implementation of the RTA method. Total surface area (A_{Frac}) is estimated using Eqs. 6.7 and 6.11 for the cases of with and without RTA, respectively. The implementation of RTA results in a discrepancy in the surface area estimation. Optimization without RTA shows 177% over-estimation with respect to the case with RTA.

$$A_{Frac} = 4 \cdot n_{frac} \cdot x_f \cdot h \tag{6.11}$$

This is a typical issue of non-uniqueness when dealing with multidimensional problems. Shortage of information can lead to a set of solutions having good history-matching results with an ignorable difference. They, however, are merely combinations of individual variable and do not have any physical correlation. The RTA method provides the strong analytical constraint (Eq. 6.7) with the optimization honoring production data. The transient analysis is very efficient and has been successfully applied to many field cases.

Next, we discuss the hydraulic fracture quality of this well based on the optimization with RTA. Our optimization gave us equivalent 33 planar fractures for the predicted surface area. The lateral part of the well is 4,600 ft, and 15 stages of fracturing designed with each stage has 3 groups of perforations. Hence n_{design} is 45. Then the hydraulic fracturing quality index for this well is 73%:

$$I_{HF} = \frac{n_{RTA}}{n_{design}} = \frac{33}{45} = 0.73$$

Further, the designed fracture spacing was 4,600/45 = 102 ft; on the other hand the optimization results gives: 4,495/33 = 136 ft. Hence the uniform spacing between the fractures is predicted about 25 % larger than the designed value.

Another important feature of the modified RTA we adopted in this study is the calibrated dynamic matrix permeability. In general, consideration of the time-dependent permeability helps better history-matching (Appendix F). Figure 6.9 shows the profile of stress-sensitive matrix permeability over the production history. The optimized values in Table 6.3 were used for Figure 6.9a. The optimization with RTA predicts higher matrix permeability mainly stemming from higher initial matrix permeability (k_0) value, while the difference is reduced over the time due to different exponent m. For comparison, in addition, the model parameters suggested based on the core flooding experiments are shown in Table 6.4 for other shale plays. For the rest of the parameters, the same values of w/ RTA in Table 6.3 were used to build the data in Figure 6.9b.

Next, the stress-sensitive fracture width is predicted over the production history in Figure 6.10. The stress profile of the grid of the well, which experiences the fastest pressure drop was used and provided together in the secondary y-axis. RTA-assisted optimization shown in red predicts a larger fracture width up to 17 years. In Eq. 6.2, w_0 and the first term on the right hand side primarily decide the fracture width over early production period. After 100 days, the fractures start to close due to plastic deformation

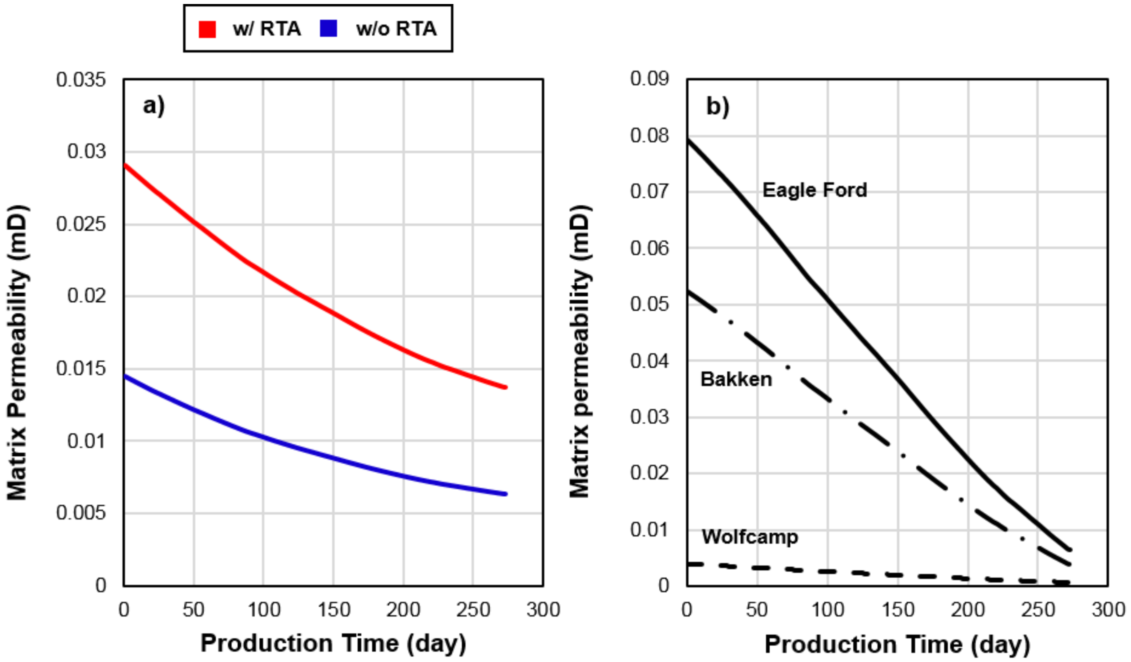

Figure 6.9 Matrix permeability based on Gangi's model versus production time.

Table 6.4 Gangi's parameters measured in the laboratory.

	k_0	m	P_{max}
	mD		*psi*
Eagle Ford	0.098	0.97	8,037
Bakken	0.065	0.95	8,027
Wolfcamp	0.005	0.86	8,336

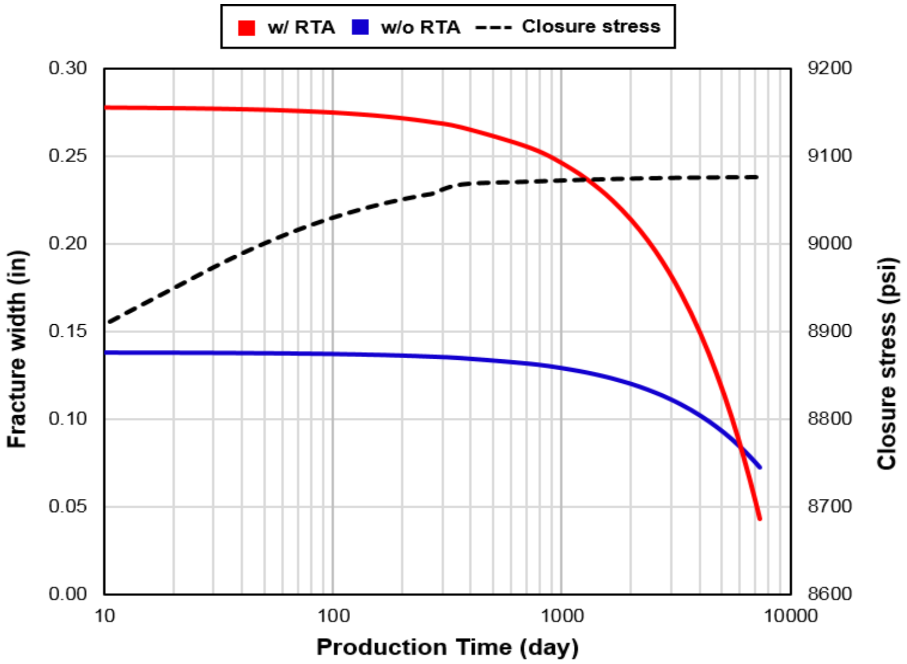

Figure 6.10 Dynamic fracture width and closure stress versus production time.

of the matrix with increasing compressional stress. The fracture closing started much later if the RTA method is not implemented in the optimization. The viscoelastic coefficient, η and the accumulation of the effective stress over time in the second term in parenthesis in Eq. 6.2 lead to reduction in fracture width in later production. As η is smaller, the fracture width is more sensitive to accumulated stress and the fractures tend to close faster.

The impact of the dynamic fracture width on the predicted bottomhole pressure and on the gas reserve is studied in and on the gas reserve is studied in Figure 6.11. In the history-matching and optimization, the viscoelastic coefficient is intentionally controlled to the huge number to maintain the constant fracture width. The calibrated parameters are shown in Table 6.5. Figure 6.11a clearly shows that consideration of dynamic fracture width results in better history-matching, and the constant width model causes 194 % error in A_{Frac}. In addition, as expected, the constant width model overestimates the cumulative production. The fractures close and production becomes difficult with dynamic model. After 20 years, the error reaches to around 23 %. Taking account that later production does not have significant impacts on cumulative production, this error is substantial.

6.5. Conclusions

History-matching on the basis of optimization has been a routine computational method to characterize the reservoirs and forecast the reserves. The multi-dimensional optimization often provides non-unique solutions, and deciding one representative solution is a challenging task. In this study we suggest incorporating analytical solution associated with an RTA method into the optimization to have physically meaningful results for the horizontal shale gas wells with multiple fractures. The analytical approach brings in new and plausible physics, hence, plays an important role as a constraint in the optimization process. This enables us to estimate more accurately the effective fracture surface area associated with the production. The implementation of the RTA-based fracture surface area to the optimization has led to significantly different reservoir and completion qualities. The proposed method can be easily applied to the existing workflows.

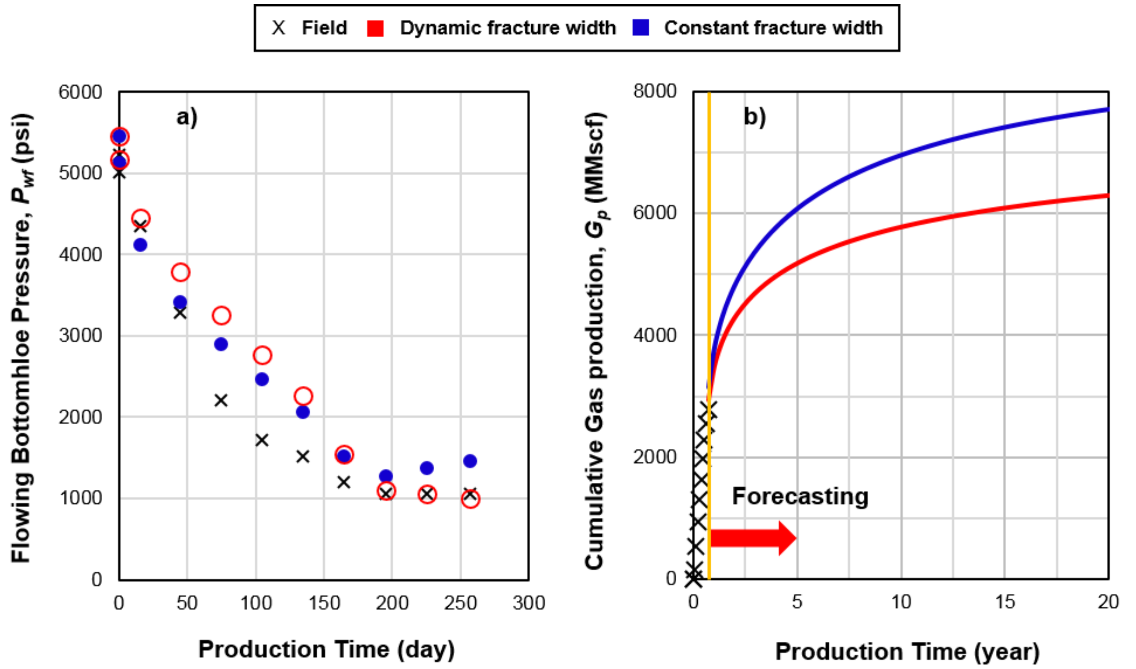

Figure 6.11 The impact of dynamic fracture width on history-matching and cumulative gas production.

Table 6.5 Comparison of optimization results with and without dynamic fracture width model.

	x_f	w_0	η	ϕ	k_0	m	P_{max}	n_{frac}	A_{Frac}
	ft	*in*	*psi-sec*		*mD*		*psi*		*acre*
Dynamic width	427	0.278	1.9E+12	0.069	0.0419	0480	10,334	33	149
Constant width	512	0.284	1.0E+15	0.068	0.0015	0.220	12,976	82	439

7. SUMMARY

Any production consideration from source rocks should include a discussion on the compositional nature of in-situ hydrocarbon fluids and its connection to the rock matrix. The present works demonstrate that the fluid composition varies in organic nanopores as a function of the pore size, when the produced fluid composition is re-distributed into the nanopores. Forecasting of production including the nano-confinement effects can be done computationally only by measuring the produced fluid composition periodically and repeating the re-distribution calculations using the methodology presented in this work. The production related field studies can also shed light into this fundamental issue.

The recovery of fluids in large pores are due to fluid expansion. But the thermodynamic recovery calculations in this article show that nano-confinement does not allow efficient expansion of the fluids and recovery becomes a slave of the hydrocarbon molecules desorption. However, fluid desorption in nanopores is not as efficient a mechanism as expansion in large pores. Thus, we addressed the stripping effects of CO_2 and C_2H_6 to the condensed hydrocarbons in kerogen. Ethane, in particular, has clear advantages over carbon dioxide because ethane controls desorption of heavier hydrocarbons from the pores more effectively and, hence, can improve the recovery efficiency.

Further, we suggest incorporating analytical solution associated with an RTA method into the optimization to have physically meaningful results for the horizontal shale gas wells with multiple fractures. The analytical approach brings in new and plausible physics, hence, plays an important role as a constraint in the optimization process. This enables us to estimate more accurately the effective fracture surface area associated with the production. The proposed method can be easily applied to the existing workflows.

REFERENCES

Arri, L. E., Yee, D., Morgan, W. D. et al. 1992. Modeling Coalbed Methane Production with Binary Gas Sorption. Presented at the SPE Rocky Mountain Regional Meeting, Casper, Wyoming, USA, 18-21 May. SPE-24363-MS. https://doi.org/10.2118/24363-MS.

Adesida, A. G., Akkutlu, I. Y., Resasco, D. E. et al. 2011. Characterization of Barnett Shale Kerogen Pore Size Distribution using DFT Analysis and Grand Canonical Monte Carlo Simulations. Presented at the SPE Annual Technical Conference and Exhibition, Denver, Colorado, USA. 30 October–2 November. SPE-147397-MS. https://doi.org/10.2118/147397-MS.

Akkutlu, I. Y. and Fathi E. 2012. Multiscale Gas Transport in Shales with Local Kerogen Heterogeneities. *SPE J.* **17** (4): 1002-1011, SPE-146422-PA. https://doi.org/10.2118/131772-PA.

Ambrose, R. J., Hartman, R. C., Diaz-Campos, M. et al. 2012. Shale Gas-in-place Calculations Part I: New Pore-scale Considerations. *SPE J.* **17** (01): 219-229, SPE-185162-PA. https://doi.org/10.2118/131772-PA.

Akkutlu, I. Y., Baek, S., Olorode, O. M. et al. 2017. Shale Resource Assessment in Presence of Nanopore Confiniement. Unconventional Resources Technology Conference, Austin, Texas, USA, July 24-26, URTeC-2670808-MS. https://doi.org/10.15530/URTEC-2017-2670808.

Aljamaan, H., Ismail, M. A. and Kovscek, A. R. 2017. Experimental Investigation and Grand Canonical Monte Carlo Simulation of Gas Shale Adsorption from the Macro to the Nano Scale. *J. Nat. Gas Sci. Eng.* **48**: 119-137. https://doi.org/10.1016/j.jngse.2016.12.024.

Britt, L. K. and Smith, M. B. 2009. Horizontal Well Completion, Stimulation Optimization, and Risk Mitigation. Presented at the SPE Eastern Regional Meeting, Charleston, West Virginia, USA, 23-25 September. SPE-125526-MS. https://doi.org/10.2118/125526-MS.

Bagherian, B., Ghalambor, A., Sarmadivaleh, M., et al. 2010. Optimization of Multiple-Fractured Horizontal Tight Gas Well. Presented at the SPE International Symposium and Exhibition on Formation Damage Control, Lafayette, Louisiana, USA. 10-12 February. SPE-127899-MS. https://doi.org/10.2118/127899-MS.

Bhattacharya, S. and Nicolaou, M. 2011. Optimal Fracture Spacing and Stimulation Design for Horizontal Wells in Unconventional Gas Reservoirs. Presented at the SPE Annual Technical Conference and Exhibition, Denver, Colorado, USA. 30 October-2 November. SPE-147622-MS. https://doi.org/10.2118/147622-MS.

Bazan, L. W., Brinzer, B. C., Meyer, B. R. et al. 2013. Key Parameters Affecting Successful Hydraulic Fracture Design and Optimized Production in Unconventional Wells. Presented at the SPE Eastern Regional Meeting, Pittsburgh, Pennsylvania, USA. 20-22 August. SPE-165702-MS. https://doi.org/10.2118/165702-MS.

Bousige, C., Ghimbeu, C. M., Vix-Guterl, C. et al. 2016. Realistic Molecular Model of Kerogen's Nanostructure. *Nat. Mater.* 15: 576-582. https://doi.org/10.1038/nmat4541.

Bui, K. and Akkutlu, I. Y. 2017. Hydrocarbons Recovery from Model Kerogen Nanopores. *SPE J.* **22** (3): 854-862. https://doi.org/10.2118/185162-PA.

Baek, S. and Akkutlu, I. Y. 2019a. Produced Fluid Composition Re-Distribution in Source Rocks for Hydrocarbon in-Place and Thermodynamic Recovery Calculations. *SPE J.* SPE-195578-PA (in press). https://doi.org/10.2118/195578-PA.

Baek, S. and Akkutlu, I. Y. 2019b. CO_2-Stripping of Kerogen Condensates in Source Rocks. *SPE J*. SPE-190821-PA (in-press). https://doi.org/10.2118/190821-PA.

Baek, S. and Akkutlu, I. Y. 2019c. Recovery Mechanisms for Nano-Confined Oil in Source Rocks using Lean Gas Injection. Presented at the SPE Western Regional Meeting, San Jose, California, USA. 23-26 April. SPE-195272-MS. https://doi.org/10.2118/195272-MS.

Baek, S., Akkutlu, I. Y., Lu, B. et al. 2019d. Shale Gas Well Production Optimization using Modified RTA Method – Prediction of the Life of a Well. Presented at the Unconventional Resources Technology Conference, Denver, Colorado, USA. 22-24 July. URTEC-185.

Bui, K. and Akkutlu, I. Y. 2015. Nanopore Wall Effect on Surface Tension of Methane. *Mol. Phys.* **113** (22): 3506-3513. https://doi.org/10.1080/00268976.2015.1037369.

Bui, K. and Akkutlu, I. Y. 2017. Hydrocarbons Recovery from Model-Kerogen Nanopores. *SPE J.* **22** (03): 854-862, SPE-185162-PA. https://doi.org/10.2118/185162-PA.

Bui, K., Akkutlu, I.Y., and Zelenev, A. 2018. Kerogen Maturation Effects on Pore Morphology and Shale Oil Recovery. Presented at the SPE EUROPEC featured at 80th EAGE Conference and Exhibition, Copenhagen, Denmark. 11-14 June. SPE-190818-MS. https://doi.org/10.2118/190818-MS.

Clarkson, C.R. and Bustin, R.M. 2000. Binary gas adsorption/desorption isotherms: effect of moisture and coal composition upon carbon dioxide selectivity over methane. *Int. J. Coal Geol*. **42** (4): 241-271. https://doi.org/10.1016/S0166-5162(99)00032-4.

Chen, T., Smit, B. and Bell, A. T. 2009. Are Pressure Fluctuation-based Equilibrium Methods Really Worse than Nonequilibrium Methods for Calculating Viscosities? *J. Chem. Phys.* 131: 246101. https://doi.org/10.1063/1.3274802.

Clarkson, C. R., Solano, N., Bustin, R. M. et al. 2013. Pore Structure Characterization of North American Shale Gas Reservoirs using USANS/SANS, Gas Adsorption, and Mercury Intrusion. *Fuel* 103: 606–616. https://doi.org/10.1016/j.fuel.2012.06.119.

Curtis, M. E., Sondergeld, C. H. and Rai, C. S. 2013. Relationship between Organic Shale Microstructure and Hydrocarbon Generation. Presented at the Unconventional Resources Conference, Woodlands, Texas, USA. 10-12 April. SPE-164540-MS. https://doi.org/10.2118/164540-MS.

Collell, J., Galliero, G., Vermorel, R. at el. 2015. Transport of Multicomponent Hydrocarbon Mixtures in Shale Organic Matter by Molecular Simulations. *J. Phys. Chem. C.* **119** (39): 22587. https://doi.org/10.1021/acs.jpcc.5b07242.

Craft, B. C. and Hawkins, M. 2015. *Applied Petroleum Reservoir Engineering*. 3rd Edition. Prentice Hall. New Jersey.

Chen, Z. and Jiang, C. 2016. A revised method for organic porosity estimation using Rock-Eval pyrolysis data, example from Duvernay Shale in the Western Canada Sedimentary Basin. *AAPG Bulletin*. **100** (3): 405-422. https://doi.org/10.1306/08261514173.

Cristancho-Albarracin D., Akkutlu, I. Y., Wang, Y. et al. 2017. Shale Gas Storage in Kerogen Nanopores with Surface Heterogeneities. *Appl. Geochem*. 84: 1-10. https://doi.org/10.1016/j.apgeochem.2017.04.012.

Chai, Z., Tang, H., He, Y. et al. 2018. Uncertainty Quantification of the Fracture Network with a Novel Fractured Reservoir Forward Model. Presented at the SPE Annual Technical Conference and Exhibition, Dallas, Texas, USA. SPE-191395-MS.

https://doi.org/10.2118/191395-MS.

de Jong, S. M., Spiers, C. J. and Busch, A. 2014. Development of Swelling Strain in Smectitie Clays through Exposure to Carbon Dioxide. *Int. J. Greenh. Gas. Con.* **24**: 149-161. https://doi.org/10.1016/j.ijggc.2014.03.010.

Dubinin, M. M. 1960. The Potential Theory of Adsorption of Gases and Vapors for Adsorbents with Energetically Nonuniform Surfaces. *Chem. Rev*. **60** (2): 235-241. https://doi.org/10.1021/cr60204a006.

Espinoza, D. N., Vandamme, M., Pereira, J.-M. et al. 2014. Measurement and Modeling of Adsorptive-Poromechanical Properties of Bituminous Coal Cores Exposed to CO_2: Adsorption, Swelling Strains, Swelling Stresses and Impact on Fracture Permeability. *Int. J. Coal Geol.* 134-135: 80-95. https://doi.org/10.1016/j.coal.2014.09.010.

Feng, F. and Akkutlu, I.Y. 2015. Flow of Hydrocarbons in Nanocapillary: A Non-Equilibrium Molecular Dynamics Study. Presented at the SPE Asia Pacific Unconventional Resources Conference and Exhibition, Brisbane, Australia. 9-11 November. SPE-177005-MS. https://doi.org/10.2118/177005-MS.

Falk, K., Coasne, B., Pellenq, R. et al. 2015. Subcontinuum Mass Transport of Condensed Hydrocarbons in Nanoporous Media. *Nat. Commun*. 6: 6949. https://doi.org/10.1038/ncomms7949.

Gangi, A. F. 1978. Variation of Whole and Fractured Porous Rock Permeability with Confining Pressure. *Int. J. Rock Mech. Min*. **15** (5): 249-257. https://doi.org/10.1016/0148-9062(78)90957-9.

Goldberg, D. E. 1989. *Genetic Algorithms in Search, Optimization and Machine Learning*. Boston, Addison-Wesley Longman Publishing Company.

Gelb, Lev D., Gubbins, K. E., Radhakrishnan, R. et al. 1999. Phase separation in confined systems. *Rep. Prog. Phys.* 62: 1573-1659. https://doi.org/10.1088/0034-4885/62/12/201.

Gorucu, S. E. and Ertekin, T. 2011. Optimization of the Design of Transverse Hydraulic Fractures in Horizontal Wells Placed in Dual Porosity Tight Gas Reservoirs. Presented at the SPE Middle East Unconventional Gas Conference and Exhibition, Muscat, Oman. 31 January-2 February. SPE-142040-MS. https://doi.org/10.2118/142040-MS.

Guo, J. and Liu, Y. 2012. Modeling of Proppant Embedment: Elastic Deformation and Creep Deformation. Presented at the SPE International Production and Operations Conference & Exhibition, Doha, Qatar. 14-16 May. SPE-157449-MS. https://doi.org/10.2118/157449-MS.

Gasparik, M., Ghanizadeh, A., Bertier, P. et al. 2012. High-Pressure Methane Sorption Isotherms of Black Shales from the Netherlands. *Energy Fuels* **26** (8): 4995-5004. https://doi.org/10.1021/ef300405g.

Gottlieb, M. A. and Pfeiffer, R. 2013. The Feynman Lectures on Physics. http://www.feynmanlectures.caltech.edu

Greathouse, J. A., Cygan, R. T., Fredrich, J. T. et al. 2016. Molecular Dynamics Simulation of Diffusion and Electirical Conductivity in Montmorillonite Interlays. *J. Phys. Chem. C*. **120** (3): 1640-1649. https://doi.org/10.1021/acs.jpcc.5b10851.

Hawthorne, S. B. 1990. Analytical-Scale Supercritical Fluid Extraction. *Anal. Chem.*, **62** (11): 633A-642A. https://doi.org/10.1021/ac00210a722.

Hartman, R. C., Ambrose, R. J., Akkutlu, I. Y. et al. 2011. Shale Gas-in-Place Calculations Part – Multicomponent Gas Adsorption Effects. Presented at the North American

Unconventional Gas Conference and Exhibition, The Woodlands, Texas, USA. 14-16 June. SPE-144097-MS. https://doi.org/10.2118/144097-MS.

Heller, R. and Zoback, M. 2014. Adsorption of Methane and Carbon Dioxide on Gas Shale and Pure Mineral Samples. *J. Unconv. Oil. Gas. Resour*. **8**: 14-24. https://doi.org/10.1016/j.juogr.2014.06.001.

Hetz, G., Kim, H., Datta-Gupta, A. et al. 2017. History Matching of Frequent Seismic Surveys using Seismic Onset Times at the Peace River Field, Canada. Presented at the SPE Annual Technical Conference and Exhibition, San Antonio, Texas, USA. 9-11 October. SPE-187310-MS. https://doi.org/10.2118/187310-MS.

Jarrell, P. M., Fox, C., Stein, M. et al. 2002. Practical Aspects of CO_2 flooding. SPE Monograph Series, Vol. 22: Society of Petroleum Engineers.

Jiang, J., Sandler, S. I., Schenk, M. et al. 2005. Adsorption and Separation of Linear and Branched Alkanes on Carbon Nanotube Bundles from Configurational-Bias Monte Carlo Simulation. *Phys. Rev. B* 72: 045447. http://dx.doi.org/10.1103/PhysRevB.72.045447.

Javadpour, F., Fisher, D. and Unsworth, M. 2007. Nanoscale Gas Flow in Shale Gas Sediments, *J. Can. Pet. Technol*. **46** (10): 55-61, PETSOC-07-10-06. https://doi.org/10.2118/07-10-06.

Javadpour, F. 2009. Nanopores and Apparent Permeability of Gas Flow in Mudrocks (Shales and Slitstone). J. Can. Pet. Technol. **48** (8): 16-21. PETSOC-09-08-16-DA. https://doi.org/10.2118/09-08-16-DA.

Kang, S. M., Fathi, E., Ambrose, R. J. et al. 2011. Carbon Dioxide Storage Capacity of Organic-Rich Shales. *SPE J*. **16** (04): 1384-1396. SPE-134583-PA. https://doi.org/10.2118/134583-PA.

Kim, B. Y., Akkutlu, I. Y., Martysevich, V. et al. 2018. Laboratory Measurement of Microproppant Placement Qaulity using Split Core Plug Permeability under Stress. Presented at the SPE Hydraulic Fracturing Technology Conference and Exhibition, The Woodlands, Texas, USA. 23-25 January. SPE-189832-MS. https://doi.org/10.2118/189832-MS.

Kim, B. Y. Olorode, O. M. and Akkutlu, I. Y. 2019. Multi-scale Analysis of CO_2 Injection as Improved Shale Gas Recovery Method. Presented at the SPE EUROPEC featured at 81th EAGE Conference and Exhibition, London, UK. 3-6 June. SPE-195528-MS.

Kim, H., Olalotiti-Lawal, F., and Datta-Gupta, A. 2019. Multi-Resolution Grid Connectivity-Based Transform for Efficient History Matching of Unconventional Reservoirs. Presented at the Unconventional Resources Technology Conference, Denver, Colorado, USA. 22-24 July. URTEC-982.

Lee, A. L., Gonzalez, M. H., and Eakin, B. E. 1966. The Viscosity of Natural Gases. *J. Pet. Technol.* **18** (8): 997-1000, SPE-1340-PA. https://doi.org/10.2118/1340-PA.

Lu, L., Wang, Q. and Liu, Y. 2003. Adsorption and Separation of Ternary and Quaternary Mixtures of Short Linear Alkanes in Zeolites by Molecular Simulation. *Langmuir* **19** (25): 10617-10623. http://dx.doi.org/10.1021/la034766z.

Loucks, R. G., Reed, R. M., Ruppel, S. C. et al. 2012. Spectrum of Pore Types and Networks in Mudrocks and a Descriptive Classification for Matrix-Related Mudrock Pores. *AAPG Bull.* **96** (6): 1071-1098. https://doi.org/10.1306/08171111061.

Liu, Y. and Wilcox, J. 2012. Molecular Simulation of CO_2 Adsorption in Micro- and Mesoporous Carbons with Surface Heterogeneity. *Int. J. Coal. Geol.* 104: 83-95. https://doi.org/10.1016/j.coal.2012.04.007.

Li, Z., Jin, Z. and Firoozabadi, A. 2014. Phase Behavior and Adsorption of Pure Substances and Mixtures and Characterization in Nanopore Structures by Density Functional Theory. *SPE J*. **19** (6): 1096-1109. SPE-169819-PA. https://doi.org/10.2118/169819-PA.

Myers, A. L. 1968. Adsorption of Gas Mixtures – a Thermodynamic Approach. *Ind. Eng. Chem.* **60** (5): 45-49. https://doi.org/10.1021/ie50701a007.

Monin, J. C., Barth, D. Perrut, M. et al. 1987. Extraction of Hydrocarbons from Sedimentary Rocks by Supercritical Carbon Dioxide. *Org. Geochem*. **13** (4): 1079–1086. https://doi.org/10.1016/0146-6380(88)90292-6.

Monger, T. G., Ramos, J. C. and Thomas, J. 1991. Light Oil Recovery from Cyclic CO_2 Injection: Influence of Low Pressures Impure CO_2, and Reservoir Gas. *SPE Reservoir Eng.* **6** (01): 25-32. SPE-18084-PA. https://doi.org/10.2118/18084-PA.

McCain, W. D. Jr. 1990. *The Properties of Petroleum Fluids*. Chapter 13. PenWell Publishing Company, Tulsa, Oklahoma.

Martin, M. G. and Siepmann, J. I. 1998. Transferable Potentials for Phase Equilibria. 1. United-Atom Description of n-Alkanes. *J. Phys. Chem. B* **102** (14) 2569-2577. http://dx.doi.org/10.1021/jp972543+.

Martin, M. G. and Siepmann, J. I. 1999. Novel Configurational-Bias Monte Carlo Method for Branched Molecules. Transferable Potentials for Phase Equilibria. 2. United-Atom Description of Branched Alkanes. *J. Phys. Chem. B* **103** (21): 4508-4517. http://dx.doi.org/10.1021/jp984742e.

Mullins, O. C., Hashem, M. Elshahawi, H. et al. 2004. Hydrocarbon Compositional Analysis In-Situ Openhole Wireline Logging. Presented at the SPWLA 45th Annual Logging Symposium, Noordwijk, The Netherlands. 6-9 June. SPWLA-2004-FFF.

Marongiu-Porcu, M., Wang, X., and Economides, M. J. 2009. Delineation of Application and Physical and Economic Optimization of Fractured Gas Wells. Presented at the SPE Production and Operations Symposium, Oklahoma City, Oklahoma. 4-8 April. SPE-120114-MS. https://doi.org/10.2118/120114-MS.

Modica, C. J. and S. G. Lapierre, 2012. Estimation of Kerogen Porosity in Source Rocks as a Function of Thermal Transformation: Example from the Mowry Shale in the Powder River Basin of Wyoming. *AAPG Bulletin* 96: 87–108.

Martin, M. G. and Siepmann, J. I. 1998. Transferable Potentials for Phase Equilibria. 1. United-Atom Description of n-Alkanes. *J. Phys. Chem. B* **102** (14) 2569-2577. http://dx.doi.org/10.1021/jp972543+.

Martin, M. G. and Siepmann, J. I. 1999. Novel Configurational-Bias Monte Carlo Method for Branched Molecules. Transferable Potentials for Phase Equilibria. 2. United-Atom Description of Branched Alkanes. *J. Phys. Chem. B* **103** (21): 4508-4517. http://dx.doi.org/10.1021/jp984742e.

Martin, M. G. 2013. MCCCS Towhee: a Tool for Monte Carlo Molecular Simulation. *Mol. Simul.* 39: 14-45, 1212-1222. https://doi.org/10.1080/08927022.2013.828208.

Middleton, R. S., Carey, J. W., Currier, R. P. et al. 2015. Shale Gas and Non-Aqueous Fracturing Fluids: Opportunities and Challenges for Supercritical CO_2. *Appl. Energy*. 147: 500-509. https://doi.org/10.1016/j.apenergy.2015.03.023.

McGuire, P. L., Okuno, R., Gould, T. L., et al. 2017. Ethane-Based EOR: An Innovative and Profitable EOR Opportunity for a Low Price Environment. *SPE. Reservoir Eval. Eng.* SPE-179565-PA. **20** (01): 42-58. https://doi.org/10.2118/179565-PA.

Nuttall, B. C., Eble, C. F., Drahovzal, J. A. et al. 2005. Analysis of Devoninan Black Shales in Kentucky for Potential Carbon Dioxdie Sequestration and Enhanced

Natural Gas Production. Report Kentucky Geological Survey of University of Kentucky. DE-FC-26-02NT41442.

Ottiger, S., Pini, R., Storti, G. et al. 2008. Measuring and Modeling the Competitive Adsorption of CO_2, CH_4, and N_2 on a Dry Coal. *Langmuir* 24: 9531-9540. https://doi.org/10.1021/la801350h.

Oliver, D. S., Reynolds, A. C., and Liu, N. 2008. *Inverse Theory for Petroleum Reservoir Characterization and History Matching*. Cambridge University Press.

Obliger, A., Pellengq, R., Ulm, F. et al. 2016. Free Volume Theory of Hydrocarbon Mixture Transport in Nanoporous Materials. *J. Phys. Chem. Lett.* 7 (19): 3712-3717. https://doi.org/10.1021/acs.jpclett.6b01684.

Olorode, O. M., Akkutlu, I. Y. and Efendiev, Y. 2017a. Compositional Reservoir-Flow Simulation for Organic-Rich Gas Shale. *SPE J*. **22** (06): 1963-1983. SPE-182667. https://doi.org/10.2118/182667-PA.

Olorode, O. M., Akkutlu, I. Y. and Efendiev, Y. 2017b. A Compositional Model for CO_2 Storage in Deformable Organic-Rich Shales. Presented at the SPE Europec featured at 79th EAGE Conference and Exhibition, Paris, France. 12-15 June. SPE-185792-MS. https://doi.org/10.2118/185792-MS.

Peng, D. Y. and Robinson, D. B. 1976. Two and Three Phase Equilibrium Calculations for Systems Containing Water. *Can. J. Chem. Eng*. **54** (6): 595-599. http://dx.doi.org/10.1002/cjce.5450540620.

Plimpton, S. J. 1995. Fast Parallel Algorithms for Short-Range Molecular Dynamics. *Comput. Phys.* **117** (1): 1-19. https://doi.org/10.1006/jcph.1995.1039.

Plaksina, T. and Gildin, E. 2015. Practical Handling of Multiple Objectives using Evolutionary Strategy for Optimal Placement of Hydraulic Fracture Stages in Unconventional Gas Reservoirs. *J. Nat. Gas Sci. Eng*. 27: 443-451.

https://doi.org/10.1016/j.jngse.2015.06.049.

Pitakbunkate, T., Balbuena, P. B., Moridis, G. J. et al. 2016. Effect of Confinement on Pressure/Volume/Temperature Properties of Hydrocarbons in Shale Reservoirs. *SPE J*. **21** (2): 621-634. SPE-170685-PA. https://doi.org/10.2118/170685-PA.

Pitakbunkate, T., Blasingame, T. A., Moridis, G. J. et al. 2017. Phase Behavior of Methane-Ethane Mixtures in Nanopores. *Ind. Eng. Chem. Res*. **56** (40): 11634-11643. https://doi.org/10.1021/acs.iecr.7b01913.

Pelaez-Soni, L., Akkutlu, I. Y., and Maggard, J. B. 2017. Shale Gas Well Total Fracture Surface Area Calculation Re-Visited for a Dynamic Formation Permeability. Presented at the SPE EUROPEC featured at 79th EAGE Conference and Exhibition, Paris, France. 12-15 June. SPE-185809-MS. https://doi.org/10.2118/185809-MS.

Ruthven, D. M. 1984. *Principles of Adsorption and Adsorption Processes*, Wiley, New York.

Rahmani D. B. and Akkutlu, I. Y. 2015. Confinement Effects on Hydrocarbon Mixture Phase Behavior in Organic Nanopore. Presented at the Unconventional Resources Technology Conference, San Antonio, Texas, USA. 20-22 July. URTEC-2151854-MS. https://doi.org/10.15530/URTEC-2015-2151854.

Rahmanifard, H. and Plaksina, T. 2018. Application of Fast Analytical Approach and AI Optimization Techniques to Hydraulic Fracture Stage Placement in Shale Gas Reservoirs. *J. Nat. Gas Sci. Eng.* 52: 367-378. https://doi.org/10.1016/j.jngse.2018.01.047.

Steele, W. A. 1973. The Physical Interaction of Gases with Crystalline Solids. I. Gas-solid Energies and Properties of Isolated Adsorbed Atoms. *Surf. Sci.* **36** (1): 317-352. http://dx.doi.org/10.1016/0039-6028(73)90264-1.

Stevenson, M. D., Pinczewski, W. V., Somers, M. L. et al. 1991. Adsorption/Desorption of Multicomponent Gas Mixtures at In-Seam Conditions. Presented at the SPE Asia-Pacific Conference, Perth, Australia. 4-7 November. SPE-23026-MS. https://doi.org/10.2118/23026-MS.

Schoen, M. and Diestler, D. J. 1998. Analytical treatment of a simple fluid adsorbed in a slit-pore. *J. Chem. Phys.* 109: 5596-5606. https://doi.org/10.1063/1.477177.

Singh, S. K., Khan, S., Jana, S. et al. 2011. Vapour–liquid Phase Equilibria of Simple Fluids Confined in Patterned Slit Pores. *Mol. Sim*. **37** (5): 350-360. https://doi.org/10.1080/08927022.2010.514778**.**

Shultz, J. M. 2015. Pore Network Variation Identified Through NMR Analysis: Eagle Ford Group, South Texas, USA. MS thesis, The University of Texas at Austin.

Travalloni, L., Castier, M., Tavares, F. W. et al. 2010. Thermodynamic modeling of confined fluids using an extension of the generalized van der Waals theory. *Chem. Eng. Sci.* **65** (10): 3088-3099. https://doi.org/10.1016/j.ces.2010.01.032.

Tsai, M. C., Chen, W. N., Cen, P. L. et al. 1985. Adsorption of Gas Mixture on Activated Carbon. *Carbon*. **23** (2): 167-173. https://doi.org/10.1016/0008-6223(85)90008-9.

van Krevelen, D. W. 1961. Coal: Typology, Chemistry, Physics, Constitution, Elsevier.

Vishnyakov, A., Piotrovskaya, E. M., Brodskaya, E. V. et al. 2001. Critical Properties of Lennard-Jones Fluids in Narrow Slit-shaped Pores. *Langmuir*, **17** (14): 4451-4458. https://doi.org/10.1021/la001641a.

Wattenbarger, R. A., El-Banbi, A. H., Villegas, M. E. et al. 1998. Production Analysis of Linear Flow into Fractured Tight Gas Wells. Presented at the SPE Rocky Mountain Regional/Low Permeability Reservoirs Symposium and Exhibition, Denver, Colorado, USA. 5-8 April. SPE-39931-MS. https://doi.org/10.2118/39931-MS.

Weniger, P., Kalkreuth, W., Busch, A. et al. 2010. High-Pressure Methane and Carbon Dioxide Sorption on Coal and Shale Samples from the Parana Basin, Brazil. *Int. J. Coal. Geol*. **84** (3-4): 190-205. https://doi.org/10.1016/j.coal.2010.08.003.

Wilson, K. and Durlofsky, L. J. 2012. Computational Optimization of Shale Resource Development Using Reduced-Physics Surrogate Models. Presented at the SPE Western Regional Meeting, Bakersfield, California, USA. 21-23 March. SPE-152946-MS. https://doi.org/10.2118/152946-MS.

Wasaki, A. and Akkutlu, I. Y. 2015. Permeability of Organic-rich Shale. *SPE J*. **20** (6): 1384-1396. SPE-170830-PA. https://doi.org/10.2118/170830-PA.

Wu, H., He, Y. and Qiao, R. 2017. Recovery of Multi-component Shale Gas from Single Nanopores. *Energy Fuels* **31** (8): 7932–7940. https://doi.org/10.1021/acs.energyfuels.7b01013.

Yang, C., Vyas, A., Datta-Gupta, A. et al. 2017. Rapid Multi-stage Hydraulic Fracture Design and Optimization in Unconventional Reservoirs using Fast Marching Method. *J. Petrol. Sci. Eng*. 156: 91-101. https://doi.org/10.1016/j.petrol.2017.05.004.

Zarragoicoechea, G. J. and Kuz, V. A. 2004. Critical shift of a confined fluid in a nanopore. *Fluid Phase Equilibr.* **220** (1): 7-9. https://doi.org/10.1016/j.fluid.2004.02.014.

Zhang, X., Du, C., Deimbacher, F. et al. 2009. Sensitivity Studies of Horizontal Wells with Hydraulic Fractures in Shale Gas Reservoirs. Presented at the International Petroleum Technology Conference, Doha, Qatar. 7-9 December. IPTC-13338-MS. https://doi.org/10.2523/IPTC-13338-MS.

Zhang, T. Ellis, G. S., Ruppel, S. C. et al. 2012. Effect of Organic-Matter Type and Thermal Maturity on Methane Adsorption in Shale-Gas Systems. *Org. Geochem.* **47**: 120-131. https://doi.org/10.1016/j.orggeochem.2012.03.012.

Zhang, T., Sun, X. and Ruppel, S. C. 2013. Integrated Hydrocarbon Geochemical Characterization and Pore Size Distribution Analysis for Bakken Shales, Williston Basin, USA. Presented at the AAPG Annual Convention and Exhibition, Pittsburgh, Pennsylvania, USA. 19-22 May.

APPENDIX A. VOLUMETRIC METHOD OF HYDROCARBON IN-PLACE IN THE PRESENCE OF NANO-CONFINEMENT EFFECTS

A.1. Hydrocarbon Volume in Large-pores

Earlier we have described the effective hydrocarbon porosity in Eq. 3.2. Now dividing each term in the equation with the bulk density of the rock, ρ_b, we convert the equation to pore volume (ft^3) in one ton of rock as follows:

$$V_{p,HC} = \varepsilon V_p + (1-\varepsilon)V_p = V_{p,Large} + V_{p,Nano} \tag{A.1}$$

where ε is volume fraction of large pores. Hence, the effective hydrocarbon pore volume $V_{p,HC}$ involves the summation of the volume εV_p of the hydrocarbons in large pores, and of the volume $(1-\varepsilon)V_p$ in the organic nanopores in which V_p is the total pore volume (ft^3) in one ton of rock.

Now, let's define n as the number of bulk hydrocarbon molecules stored in unit large pore volume (molecule number/Å^3) under the reservoir pressure and temperature conditions. This number comes from NPT molecular simulation of the mixture with the produced fluid composition, and n is equal to the total number of molecules N divided by the computational box volume predicted from the simulation. The total number of moles of the hydrocarbon molecules stored in the large pores volume in one ton of source rock is equal to $\varepsilon \times V_p \times n/N_A$, where N_A is Avogadro's number (= 6.023x10^{23} molecule number/mol). Finally, using the gas law equation, the volume of the hydrocarbon molecules stored in the large pores volume in one ton of source rock in standard ft^3/ton is:

$$V_{p,Large} = \varepsilon V_p \times \left(\frac{n}{N_A}\right) \times \left(\frac{RT_{sc} z_{sc}}{P_{sc}}\right) \qquad \text{(scf/ton)} \qquad \text{(A.2)}$$

Here, z_{sc}=1.0 is taken. Since the hydrocarbons in large pores volume is in the bulk state, the same results could have been obtained using the traditional volumetric approach.

A.2. Hydrocarbon Volume in Nano-pores

Calculation for hydrocarbon volume stored in nanopores is more elaborate and involves further partitioning the nanopores volume into its constituents as follows. Consider pore volume for the specific nanopore size d_p in a ton of source rock:

$$V_{p,Nano,dp} = V_p \times V_{\%,dp} / 100 \qquad \text{(A.3)}$$

where $V_{\%dp}$ is the volume percent of the nanopore with size d_p in the source rock, as obtained from incremental pore volume distribution vs. pore size data.

If the simulated number density of hydrocarbon molecules in the nanopore i is equal to n_i (molecule number/Å^3), the hydrocarbon volume stored in the pore under the standard conditions is:

$$V_{HC,Nano,dp} = V_{p,Nano,dp} \times \left(\frac{n_{dp}}{N_A} \right) \times \left(\frac{RT_{sc} z_{sc}}{P_{sc}} \right)$$

$$= V_p \times \left(\frac{V_{\%,dp}}{100} \right) \times \left(\frac{n_{dp}}{N_A} \right) \times \left(\frac{RT_{sc} z_{sc}}{P_{sc}} \right) \qquad \text{(A.4)}$$

Hydrocarbons stored in all the nanopores are then the summation of the latter equation:

$$V_{HC,Nano} = \sum_{dp1}^{dp,L} V_{HC,Nano,dp} = V_p \left(\frac{RT_{sc} z_{sc}}{N_A P_{sc}} \right) \sum_{dp1}^{dp,L} \left(\frac{V_{\%,dp}}{100} \right) n_{dp} \qquad \text{(A.5)}$$

Here the summation is over the organic nanopores, d_p =1 nm ... $d_{p,L}$ with confined hydrocarbons.

A.3. Initial Hydrocarbon In-place including Nanopore Confinement Effects

Then, the total hydrocarbon in place is:

$$V_{p,HC} = V_{p,Large} + V_{p,Nano} \qquad \text{(A.1)}$$

$$= V_p \left(\frac{RT_{sc}}{N_A P_{sc}} \right) \times \left(\varepsilon \times n + \sum_{dp}^{dp,L} \frac{V_{\%,d_p}}{100} \times n_{dp} \right) \qquad \text{(A.6)}$$

$$= 1.2603 \times 10^6 \times V_p \times \left(\varepsilon \times n + \sum_{dp}^{dp,L} \frac{V_{\%,d_p}}{100} \times n_{dp} \right) \quad \text{(scf/ton)} \qquad \text{(3.4b)}$$

$$= 7.59 \cdot 10^5 \cdot V_p \cdot \left(\varepsilon \cdot \rho_{bulk,mol} + \sum_{d_{p1}}^{dp,L} \frac{V_{\%,d_p}}{100} \cdot \rho_{dp,mol} \right) \quad \text{(scf/ton)} \qquad \text{(A.7)}$$

in which ϕ and ρ_b are total porosity and rock density respectively. The units for ρ_b, n, n_{dp}, $V_{\%,dp}$, $\rho_{bulk,mol}$ and $\rho_{dp,mol}$ are g/cm^3, molecule numbers/A^3, molecule numbers/A^3, percentage, mol/cm^3 and mol/cm^3, respectively. ϕ and ε are dimensionless fraction.

A.4. Description of Total Amount of Hydrocarbons Stored Considering Trapped Hydrocarbons

$$G^* = \frac{\emptyset\,(1 - S_w)}{\rho_b B_g} - V_T = \frac{\emptyset\,(1 - S_w - S_{trappedHC})}{\rho_b B_g} \qquad \text{(A.8)}$$

$$S_{trappedHC} = \frac{V_T\,\rho_b B_g}{\emptyset} \qquad \text{(A.9)}$$

in which V_T is the volume of hydrocarbons trapped in pores with pore size less than $d_{p,T}$. ε_T is the fraction of the pore volume with respect to total hydrocarbon pore volume. V_w is the volume occupied by water, and S_w is the fraction of the effective porosity filled with water (S_w=V_w/V_{total}) in that, saturation.

APPENDIX B. RE-DISTRIBUTED COMPOSITION OF HYDROCARBONS IN NANOPORES

The molecular simulation data of number density, n_{dp} is shown for the mixtures. The unit is molecule number/Å^3.

Table B.1 Re-distribution data of Mixture 1.

Pore size nm	Pressure, psi			
	1,000	2,000	3,000	4,000
1	1.64470E-02	1.91210E-02	2.05476E-02	2.14873E-02
2	6.34491E-03	8.99244E-03	1.04546E-02	1.14225E-02
3	4.25710E-03	6.54835E-03	8.10483E-03	9.24243E-03
4	3.44131E-03	5.51966E-03	7.08200E-03	8.28042E-03
5	2.99967E-03	4.96896E-03	6.51975E-03	7.74248E-03
6	2.71755E-03	4.61611E-03	6.15761E-03	7.40395E-03
7	2.52469E-03	4.37908E-03	5.91590E-03	7.16439E-03
8	2.38728E-03	4.20261E-03	5.73210E-03	6.99766E-03
9	2.28148E-03	4.06515E-03	5.59246E-03	6.86644E-03
10	2.19708E-03	3.96061E-03	5.48584E-03	6.76284E-03
20	1.83658E-03	3.50119E-03	5.01895E-03	6.31499E-03
30	1.71969E-03	3.35534E-03	4.86371E-03	6.17070E-03
40	1.66313E-03	3.28391E-03	4.79195E-03	6.10363E-03

Table B.2 Re-distribution data of Mixture 2.

Pore size nm	Pressure, psi			
	1,000	2,000	3,000	4,000
1	9.09467E-03	9.64178E-03	1.08049E-02	1.14782E-02
2	7.83185E-03	8.67527E-03	9.40256E-03	9.89705E-03
3	6.50690E-03	7.34560E-03	8.01632E-03	8.72932E-03
4	5.37134E-03	6.87299E-03	7.65877E-03	8.29691E-03

5	4.20080E-03	6.08877E-03	7.03823E-03	7.91339E-03
6	3.75660E-03	5.77459E-03	6.89685E-03	7.73877E-03
7	3.36752E-03	5.35527E-03	6.58847E-03	7.56853E-03
8	3.18191E-03	5.20842E-03	6.51724E-03	7.41944E-03
9	2.94923E-03	4.97044E-03	6.31335E-03	7.30789E-03
10	2.83330E-03	4.87600E-03	6.29839E-03	7.23811E-03
20	2.21453E-03	4.23979E-03	5.81463E-03	6.85437E-03
30	2.02780E-03	4.04023E-03	5.70812E-03	6.78050E-03
40	1.92611E-03	3.93897E-03	5.70812E-03	6.75536E-03

Table B.3 Re-distribution data of Mixture 3.

Pore size nm	Pressure, psi			
	1,000	**2,000**	**3,000**	**4,000**
1	9.27741E-03	1.01492E-02	1.07224E-02	1.10809E-02
2	7.68607E-03	8.48476E-03	8.95253E-03	9.34449E-03
3	6.64071E-03	7.32058E-03	7.77733E-03	8.18333E-03
4	6.39283E-03	6.93540E-03	7.53386E-03	7.90476E-03
5	6.18440E-03	6.68116E-03	7.25953E-03	7.71296E-03
6	6.12751E-03	6.47927E-03	7.14970E-03	7.64122E-03
7	6.06551E-03	6.37878E-03	7.09036E-03	7.54682E-03
8	5.93642E-03	6.15606E-03	6.88658E-03	7.42778E-03
9	5.92348E-03	6.09331E-03	6.92817E-03	7.41872E-03
10	5.81912E-03	5.93203E-03	6.76639E-03	7.35176E-03
20	5.61356E-03	5.45715E-03	6.52959E-03	7.14957E-03
30	5.26936E-03	5.26242E-03	6.46539E-03	7.08516E-03
40	4.27687E-03	5.14203E-03	6.42272E-03	7.07104E-03

APPENDIX C. EXAMPLE CALCULATION OF INITIAL HYDROCARBON IN-PLACE WITH NANO-CONFINEMENT EFFECTS

Here, we include an example calculation showing how the nano-confinement effects can be introduced to the classical volumetric method calculations using empirical correlations proposed in this study. For the calculations, we consider 5 % total porosity and 35 % water saturation for the formation and the bulk density of the rock is taken 2.5 g/cm^3. We use Mixture 3 composition given in Table 3.1 as the bulk hydrocarbon fluid produced, which has 53.8 % Methane, 16.4 % Ethane, 12.7 % Propane, 10.5 % n-Butane and 6.6 % n-Pentane. For the calculation we consider that the formation holds 60 % of the pore volume as large pores, i.e., ε is 0.6. The rest of the pores are made of nanopores with 10 % 10 nm pores, 10 % 8 nm pores, 10 % 6 nm pores 5 % 4 nm pores and 5 % 2 nm pores.

1. Calculate z-factor for the bulk fluid mixture

z-factor is needed to calculate the bulk molar density of the produced fluid mixture. It is first necessary to determine the pseudo critical pressure and temperature of the mixture as,

$\boldsymbol{p_{pc} = \sum_i x_i p_{ci}} =$ 0.538·668 + 0.164·708 + 0.127·616 + 0.105·551 + 0.066·489 = 643.86 psi

$\boldsymbol{T_{pc} = \sum_i x_i T_{ci}} =$ 0.538·343 + 0.164·550 + 0.127·666 + 0.105·765 + 0.066·845 = 495.40 °R

where x_i are the mole fractions of each component in the bulk fluid. Next step is to calculate pseudo-reduced pressure and pseudo-reduced temperature.

$$\boldsymbol{p_{pr} = \frac{p}{p_{pc}} = \frac{4000\,psi}{643.9\,psi} = 6.2} \qquad \boldsymbol{T_{pr} = \frac{T}{T_{pc}} = \frac{635.67\,°\mathrm{R}}{495.4\,°\mathrm{R}} = 1.28}$$

where p and T are the initial reservoir conditions, which are 4,000 psi and 176 °F (= 635.67 °R). Then using the calculated p_{pr}, T_{pr} and the Standing-Katz correlation chart (Standing and Katz 1942), z-factor is obtained as 0.815. PC-SAFT equation of state gives 0.814, which confirms the z-factor value obtained.

2. Calculate molar density of the bulk fluid mixture

To calculate the bulk molar density at the initial reservoir conditions, the real gas isothermal compressibility equation is adopted.

$$\boldsymbol{\rho_{bulk,mol} = \frac{p}{zRT} = \frac{4000\,psi}{(0.815)\cdot\left(1205.913\,\frac{cm^3\cdot psi}{K\cdot mol}\right)\cdot(353.15\ \mathrm{K})}} = 0.01155\,\boldsymbol{\frac{mol}{cm^3}}$$

3. Calculate hydrocarbon in-place using volumetric method

Now, we are ready to calculate the formation volume factor and to predict the hydrocarbon in-place. We shall do this calculation twice. First, we ignore the nanopore confinement effects and use the classical volumetric method for the calculation.

We have formation volume factor without nano-confinement effects:

$B_g = 0.02829 \cdot z \cdot T/p = 0.02829 \cdot 0.815 \cdot 635.67/4000 = 3.6641 \cdot 10^{-3}$ ft^3/scf

Using Equation 3.4a:

$$\boldsymbol{G = 32.0368\,\frac{\emptyset(1-S_w)}{\rho_b B_g}} = \boldsymbol{32.0368\,\frac{0.05(\,1-0.35)}{2.5\cdot 3.6641\cdot 10^{-3}}} = 113.7\ \text{scf/ton}$$

With nano-confinement effects:

Taking $\boldsymbol{\rho_{bulk,mol}} = 0.01155$ mol/cm^3, the coefficients c and d are calculated using Equations 3.10b and 3.10c:

c = -26159.41 · 0.01155^2 + 599.0111 · 0.01155 – 3.32647 = 0.102354

d = 92405.03 · 0.01155^2 - 2121.03 · 0.01155 + 12.83228 = 0.661549

Next, using Eq. 3.10a and the calculated values of the coefficients c and d, we determine the molar density of the confined fluid for each nanopore:

$$\rho_{dp,mol} = \left[c \cdot \ln\left(d_p\right) + d\right] \cdot \left(\frac{\rho_{dp,mol,CH4}}{\rho_{bulk,mol,CH4}}\right) \cdot \rho_{bulk,mol} \qquad (\text{mol/cm}^3) \qquad (3.16a)$$

where $\rho_{dp,mol,CH4}/\rho_{bulk,mol,CH4}$ are obtained from Table 3.2 for each pore.

$\rho_{2nm,mol}$ = [0.102354 · ln(2) + 0.661549] · 1.93546 · 0.01155 = 0.016375 mol/cm^3

$\rho_{4nm,mol}$ = [0.102354 · ln(4) + 0.661549] · 1.40306 · 0.01155= 0.013020 mol/cm^3

$\rho_{6nm,mol}$ = [0.102354 · ln(6) + 0.661549] · 1.25455 · 0.01155= 0.012243 mol/cm^3

$\rho_{8nm,mol}$ = [0.102354 · ln(8) + 0.661549] · 1.1857 · 0.01155= 0.011975 mol/cm^3

$\rho_{10nm,mol}$ = [0.102354 · ln(10) + 0.661549] · 1.14591 · 0.01155= 0.011875 mol/cm^3

Next, we calculate the formation volume factor with nano-confinement effects using Eq. 3.9:

$$B_g^* = \frac{4.22092 \times 10^{-5}}{\varepsilon \times \rho_{bulk,mol} + \sum_{d_{p1}}^{dp,L} \frac{V_{\%,d_p}}{100} \times \rho_{dp,mol}} \qquad (\text{ft}^3/\text{scf}) \qquad (3.9)$$

$$\begin{aligned} B_g^* = {} & 4.22092 \cdot 10^{-5} \\ & /[0.65 \times 0.01155 + (0.05 \cdot 0.01638 + 0.05 \cdot 0.01302 + 0.1 \cdot 0.01224 \\ & + 0.1 \cdot 0.01198 + 0.1 \cdot 0.01188)] \\ = {} & \mathbf{3.3533} \cdot 10^{-3} \text{ ft}^3/\text{scf} \end{aligned}$$

Again, using Equation 3.8:

$$\boldsymbol{G = 32.0368 \frac{\emptyset(1-S_w)}{\rho_b B_g^*}} = \boldsymbol{32.0368 \frac{0.05(1-0.35)}{2.5 \cdot 3.3533 \cdot 10^{-3}}} = 124.2 \text{ scf/ton}$$

This gives (113.7-124.2)/113.7x100 = -9.2 % error in hydrocarbon in-place for neglecting the nano-confinement effects.

APPENDIX D. RE-DISTRIBUTED COMPOSITION OF HYDROCARBONS-CO2 MIXTURES IN NANOPORES

Table D.1 Mole fraction in nanopores with CO_2 injection into bulk phase.

Mole fraction of CO_2 in bulk	Pressure Psi	Pore size nm	CO_2	CH_4	C_2H_6	C_3H_8	n-C_4H_{10}	n-C_5H_{12}
0.0	500	2	0.000	6.545	7.646	13.445	27.407	44.957
		4	0.000	8.707	8.478	14.749	27.633	40.433
		6	0.000	15.145	10.361	15.335	26.431	32.728
	1,500	2	0.000	15.059	11.842	17.230	26.548	29.321
		4	0.000	21.589	13.900	17.479	23.463	23.569
		6	0.000	25.017	14.314	16.937	22.861	20.871
	2,500	2	0.000	25.668	15.121	16.608	21.314	21.289
		4	0.000	35.406	15.907	15.821	17.731	15.135
		6	0.000	40.304	16.091	15.012	15.729	12.864
	3,500	2	0.000	31.106	16.103	16.624	20.523	15.645
		4	0.000	40.030	16.415	15.012	16.005	12.538
		6	0.000	44.206	16.370	14.286	14.798	10.340
0.1	500	2	0.031	0.056	0.068	0.124	0.268	0.453
		4	0.034	0.082	0.078	0.138	0.273	0.394
		6	0.049	0.161	0.099	0.145	0.255	0.290
	1,500	2	0.061	0.137	0.110	0.154	0.239	0.299
		4	0.068	0.193	0.126	0.157	0.216	0.239
		6	0.072	0.224	0.133	0.160	0.205	0.206
	2,500	2	0.083	0.227	0.134	0.158	0.217	0.180
		4	0.086	0.321	0.146	0.145	0.164	0.138
		6	0.090	0.357	0.146	0.139	0.148	0.120
	3,500	2	0.089	0.271	0.141	0.143	0.188	0.169
		4	0.091	0.364	0.148	0.136	0.145	0.115
		6	0.095	0.402	0.148	0.131	0.124	0.099
0.3	500	2	0.100	0.046	0.054	0.112	0.249	0.439
		4	0.113	0.074	0.067	0.122	0.242	0.384
		6	0.154	0.135	0.082	0.121	0.210	0.297
	1,500	2	0.185	0.103	0.085	0.127	0.203	0.297
		4	0.204	0.149	0.097	0.130	0.190	0.230
		6	0.219	0.174	0.102	0.129	0.178	0.197
	2,500	2	0.249	0.178	0.104	0.124	0.169	0.176
		4	0.261	0.248	0.116	0.119	0.135	0.121
		6	0.274	0.282	0.117	0.110	0.121	0.096

	3,500	2	0.272	0.213	0.108	0.119	0.156	0.132
		4	0.274	0.282	0.113	0.112	0.118	0.102
		6	0.282	0.314	0.114	0.104	0.104	0.081
0.5	500	2	0.185	0.037	0.047	0.096	0.234	0.401
		4	0.249	0.086	0.062	0.101	0.188	0.314
		6	0.279	0.110	0.065	0.095	0.173	0.278
	1,500	2	0.326	0.077	0.066	0.107	0.181	0.243
		4	0.363	0.115	0.076	0.103	0.158	0.186
		6	0.391	0.141	0.079	0.100	0.136	0.152
	2,500	2	0.428	0.129	0.079	0.098	0.125	0.141
		4	0.446	0.180	0.082	0.087	0.100	0.105
		6	0.460	0.203	0.084	0.081	0.090	0.082
	3,500	2	0.445	0.160	0.083	0.090	0.108	0.115
		4	0.467	0.206	0.086	0.081	0.088	0.072
		6	0.473	0.226	0.085	0.076	0.073	0.067
0.7	500	2	0.297	0.025	0.034	0.078	0.188	0.378
		4	0.389	0.060	0.044	0.077	0.154	0.276
		6	0.433	0.072	0.044	0.074	0.142	0.235
	1,500	2	0.619	0.080	0.049	0.067	0.094	0.091
		4	0.639	0.110	0.052	0.058	0.072	0.068
		6	0.651	0.122	0.050	0.054	0.063	0.059
	2,500	2	0.619	0.080	0.049	0.067	0.094	0.091
		4	0.639	0.110	0.052	0.058	0.072	0.068
		6	0.651	0.122	0.050	0.054	0.063	0.059
	3,500	2	0.644	0.096	0.051	0.060	0.072	0.079
		4	0.655	0.127	0.053	0.053	0.063	0.049
		6	0.667	0.136	0.052	0.049	0.054	0.041
0.9	500	2	0.516	0.012	0.018	0.049	0.134	0.271
		4	0.614	0.025	0.020	0.043	0.098	0.200
		6	0.651	0.028	0.020	0.040	0.091	0.169
	1,500	2	0.735	0.019	0.020	0.039	0.075	0.112
		4	0.784	0.031	0.021	0.034	0.054	0.076
		6	0.809	0.035	0.020	0.029	0.044	0.064
	2,500	2	0.839	0.029	0.019	0.027	0.038	0.047
		4	0.863	0.039	0.020	0.024	0.028	0.026
		6	0.871	0.043	0.019	0.021	0.022	0.023
	3,500	2	0.864	0.033	0.019	0.024	0.029	0.030
		4	0.871	0.043	0.019	0.020	0.025	0.021
		6	0.876	0.047	0.019	0.019	0.021	0.018

APPENDIX E. RTA METHODS WITH ANALYTICAL SOLUTIONS FOR FRACTURE SURFACE AREA

Table E.1 Comparison of the original and modified RTA methods.

	$A\sqrt{k}$ method proposed by Wattenbarger et al. (1998)	**Modified RTA method proposed by Pelaez-Soni et al. (2017)**
$1/q_D$	$\frac{kh[m(p_i)-m(p_{wf})]}{1424q_gT}$	$\frac{x_fh[m(p)_{ki}-m(p)_k]}{2236q_gLT}$
t_D	$\frac{0.00633kt}{(\phi\mu c_t)_iy_e^2}$	$\frac{0.00633kt_{ap}}{\phi L^2}$
$m(p) \rightarrow m(p)_k$	$2\int_{p_0}^{p}\frac{p}{z\mu}dp$	$2\int_{p_b}^{p}\frac{k_gp}{z\mu}dp$
$t \rightarrow t_{ap}$	t	$t_{ap}=\int_0^t\frac{k_g}{\mu c_t}dt$
$m_{cp} \rightarrow m_{cpk}$	$\frac{315.4T}{x_fh\sqrt{(\phi\mu c_t)_i}}\cdot\frac{1}{\Delta m(p)\sqrt{k}}$	$\frac{315.4T}{x_fh\sqrt{(\phi)_i}}\cdot\frac{1}{\Delta m(p)_k}$
A_{Frac}	$f_{cp}\cdot\frac{1261.2T}{m_{cp}\sqrt{(\phi\mu c_t)_i}}\cdot\frac{1}{\Delta m(p)\sqrt{k}}\cdot n$	$f_{cp}\cdot\frac{1261.2T}{m_{cp}\sqrt{(\phi)_i}}\cdot\frac{1}{\Delta m(p)_k}\cdot n$

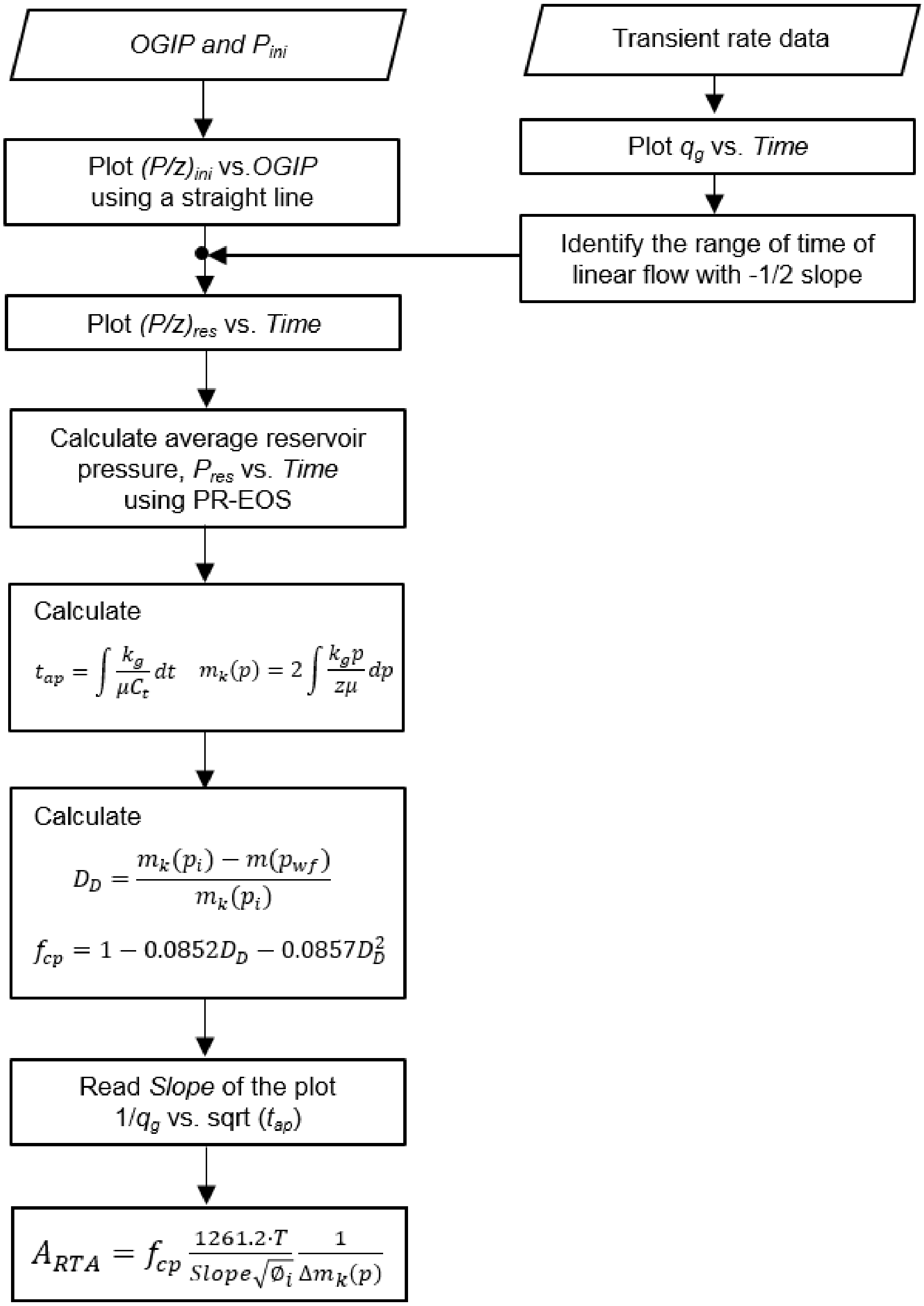

Figure E.1 Flow chart of modified RTA method proposed by Pelaez-Soni et al. (2017).

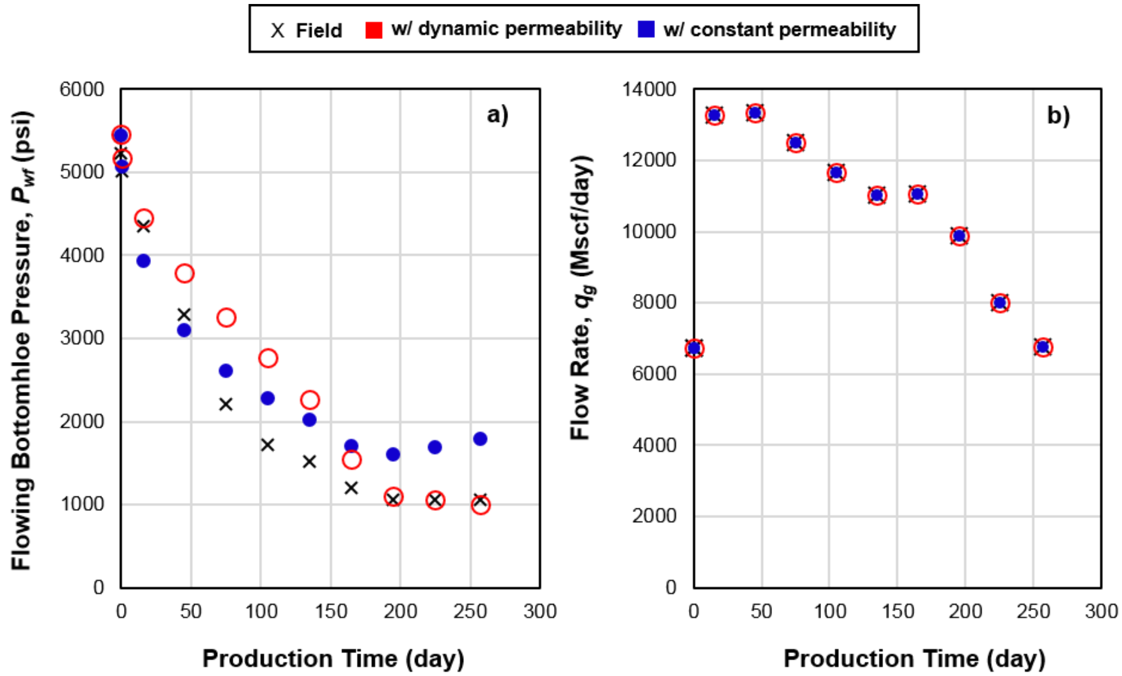

Figure F.1 History-matching and optimization results with and without dynamic matrix permeability model.

Table F.1 Comparison of optimization results with and without dynamic matrix permeability model.

	x_f	w_0	η	ϕ	k_0	m	P_{max}	n_{frac}
	ft	*in*	*psi-sec*		*mD*		*psi*	
Dynamic perm	427	0.278	1.86E+12	0.069	0.0419	0480	10,334	33
Constant perm	413	0.304	4.42E+12	0.075	0.0020	1.000	1.0E+10	13